Polymat

Contributions

Proceedings

Polymat Contributions

Structural and mechanical analysis of fabrication of poly(lactic acid)/poly(caprolactone)/murexide blends

Ariel Eduardo Alarcón Fuentes[1,2], Mayra Elizabeth Juárez Méndez[1], José Alberto Andraca Adame[1], Yunuén López Grijalba[1], Helen Willcock[2], Diana Palma-Ramírez[1*]

*[1]Instituto Politécnico Nacional, Unidad Profesional Interdisciplinaria de Ingeniería Campus Hidalgo (UPIIH), Department of Polymers and Nanomaterials, Pachuca, Hidalgo, 42162, México, *dpalmar@ipn.mx*

[2] Loughborough University, Materials Department, Loughborough LE11 3TT, UK

Abstract

The automotive sector is constantly evolving, including changes in the textures and shapes of interior components. However, users often cause minor damage that, due to its impact on appearance, leads to the disposal of these parts or even affects the vehicle's resale value. One way to reduce this waste is by incorporating self-healing capabilities into materials, as well as replacing conventional polymers with biodegradable alternatives to minimize environmental impact. To address this, a combination of poly (lactic acid) (PLA), poly(caprolactone) (PCL), and murexide particles into polymer blends is proposed to study the possibility of imparting self-healing properties and preventing components from being discarded or replaced solely due to visual damage. The blends are studied using Raman spectroscopy, confocal laser scanning microscopy (CLSM), and compression test to analyze their mechanical, morphological, and structural properties.

Introduction

Automotive interior components are typically manufactured from polymers derived from fossil sources [1], which contributes to their slow degradation. As a result, studies emphasize their degradability [2]. This highlights the importance of seeking eco-friendly alternatives to reduce the amount of waste generated by automotive parts that can no longer be used. Although recycling efforts have been made for such components [3], issues such as scratches, minor fractures, or aesthetic damage often lead to increased waste. Therefore, it becomes necessary to introduce materials with self-healing capabilities.

A polymeric material with self-healing properties requires a matrix, a catalyst, and microcapsules. When damage occurs, and self-repair is triggered, these microcapsules react to fill the crack and mitigate mechanical or aesthetic damage, depending on the aspect being analyzed [4]. In this study, the material was developed using a matrix composed of poly (lactic acid) (PLA), poly(caprolactone) (PCL), and murexide particles. The blends were prepared through the solvent casting method to analyze the structural, morphological, and mechanical behavior. Raman spectroscopy, confocal laser scanning microscopy (CLSM) analysis, and compression tests were conducted to establish a foundation for advancing the development of this material blend.

Methodology

To prepare the samples, a modification was carried out by grafting maleic anhydride onto PLA to obtain PLA_g using benzoyl peroxide as an initiator. The following procedure was performed: 50 g of PLA pellets (4032 Da, Ingeo) were mixed with 1 g of maleic anhydride (Alquimia Mexicana) and 0.01 g of benzoyl peroxide (Sigma-Aldrich) in 150 mL of methylene chloride

(Wohler, 98% purity). The mixture was heated at 60 °C and 350 rpm using a heating plate with magnetic stirring, employing a stirring bar in a 500 mL flask. A condensation system was required due to the boiling point of methyl chloride (39.7 °C).
Once the reaction was complete, the mixture was poured dropwise into a 1 L round-bottom flask containing 600 mL of acetone. After this stage, the product was filtered to separate the grafted PLA and dried at 60 °C for 24 h. The resulting material was then used to prepare the corresponding blends in methylene chloride at room temperature. PLA_x/PCL_{x-y}, $PLA_{g\ x}/PCL_{x-y}$, $PLA_x/PCL_{x-y}/Mu$, $PLA_{g\ x}/PCL_{x-y}/Mu$ blends in which x is the PLA, x-y the PLC, and Mu are murexide particles (0.1 wt%) contents. Ratios of 70/30, 80/20, and 90/10 under an argon atmosphere were prepared. After blending, the methyl chloride was evaporated in glass molds.

Results and discussion

The samples were subjected to compression tests to observe the differences among them. Results showed that samples modified through grafting and containing murexide particles exhibited greater deformation under increased stress across all three groups. Among these, the PLA_{80}/PCL_{20} blend appeared most promising, as the other mixtures demonstrated more favorable deformation behavior as the force increased. These findings are supported by the data presented in Figure 1.

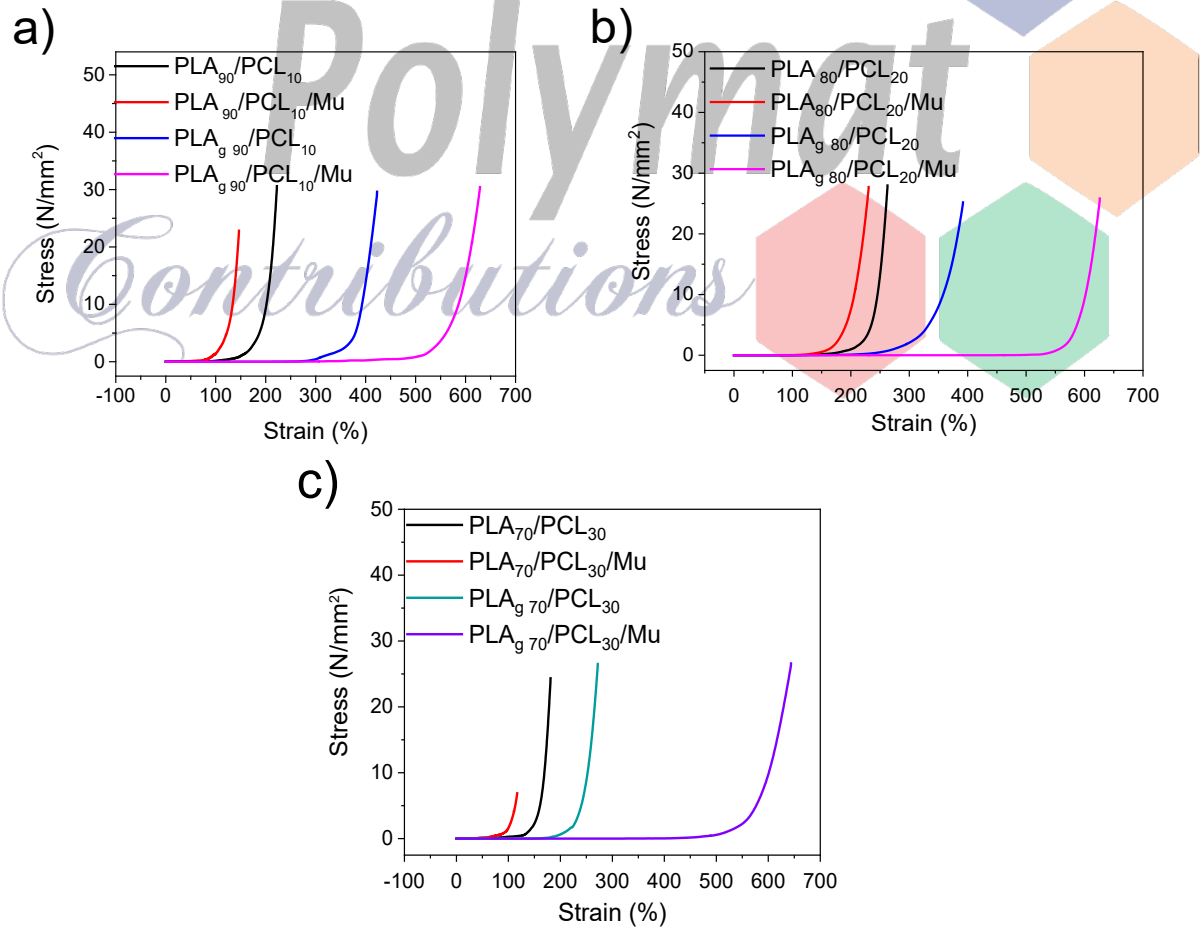

Figure 1. Strain vs. stress curves of blends.

Regarding the CLSM analysis (Figure 2), four evaluations were conducted on selected-PLA_{80}/PCL_{20} and PLA_{90}/PCL_{10} blends, revealing distinct differences in their mechanical behavior. Blends containing modified PLA showed variations compared to those with unmodified PLA, exhibiting a layered-like behavior that accounts for the observed differences. This effect was more pronounced in the PLA_{80}/PCL_{20} blends, which were therefore considered the optimal formulation among the four variants: PLA_x/PCL_{x-y}, $PLA_{g\ x}/PCL_{x-y}$, $PLA_x/PCL_{x-y}/Mu$, $PLA_{g\ x}/PCL_{x-y}/Mu$. Additionally, it was observed that murexide particles do not exhibit fluorescence, which explains the presence of small black voids in micrographs.

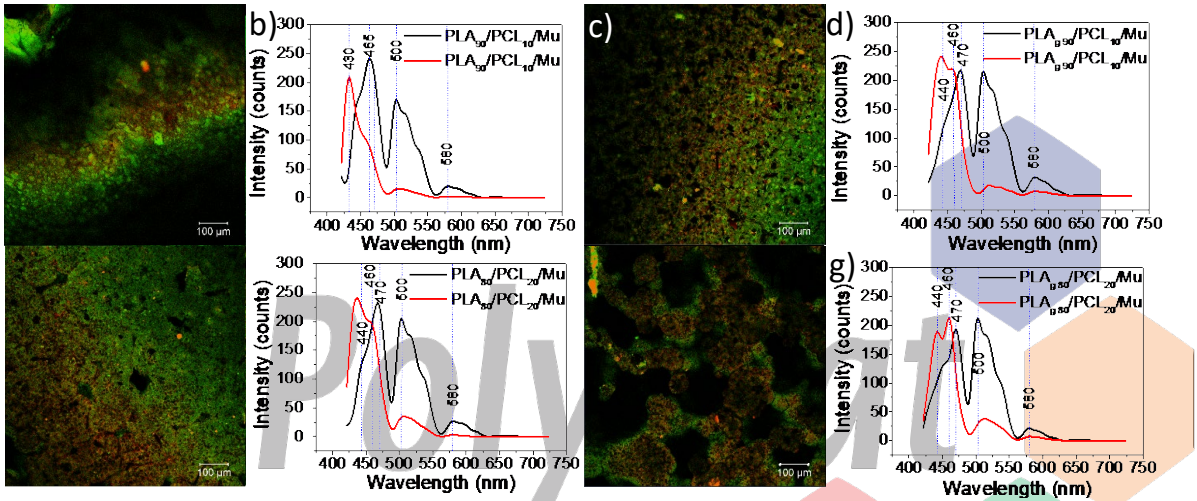

Figure 2. CLSM micrographs and emission spectrum of blends.

In the final analysis, the signals and functional groups of selected-$PLA_{80}/PCL_{20}/Mu$, $PLA_{g\ 80}/PCL_{20}/Mu$ can be observed in Figure 3. Upon analyzing the functional groups of the blends and the raw materials, no new signals were detected. In fact, no significant differences were observed between the PLA and PLA_g samples. Therefore, it can be concluded that the resulting spectra represent only a combination of the signals from the raw materials, without any new signals arising from chemical interactions or reactions that would have significantly altered the blends.

Polymat Contributions

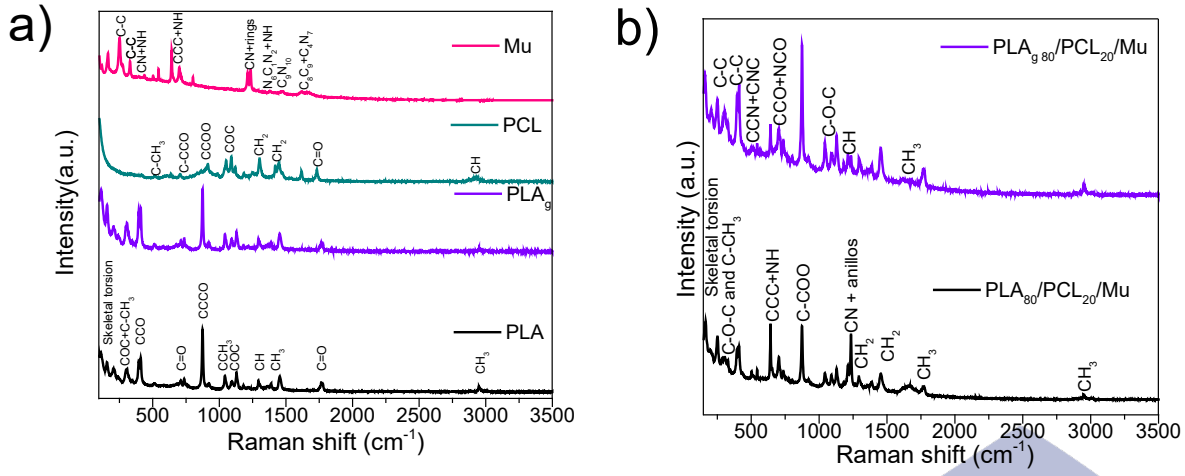

Figure 3. Raman spectra of a) raw materials and b) selected-blends.

Conclusions

The PLA_{80}/PCL_{20} blends proved to be the most suitable for mechanical testing using this method, as evidenced by the stress–strain graphs. Additionally, the micrographs support these findings, showing a layered-like behavior that contributes to improved mechanical properties across various compositions. Raman analysis confirmed that no chemical reactions occurred that would alter the functional groups of the raw materials.

Therefore, the theory behind self-healing materials is upheld, with PLA serving as the polymeric matrix, PCL potentially acting as the microcapsules, and murexide particles functioning as the catalytic agent.

References

[1] F. Lupone, J. Tirillò, F. Sarasini, C. Badini, and C. Sergi, "3D Printing of Low-Filled Basalt PA12 and PP Filaments for Automotive Components," vol. 7, no. 9, p. 367, 2023.

[2] M. Wróbel, S. Szymańska, T. Kowalkowski, and K. Hrynkiewicz, "Selection of microorganisms capable of polyethylene (PE) and polypropylene (PP) degradation," *Microbiological Research,* vol. 267, p. 127251, 2023/02/01/ 2023.

[3] S. Saikrishnan, D. Jubinville, C. Tzoganakis, and T. H. Mekonnen, "Thermo-mechanical degradation of polypropylene (PP) and low-density polyethylene (LDPE) blends exposed to simulated recycling," *Polymer Degradation and Stability,* vol. 182, p. 109390, 2020/12/01/ 2020.

[4] I. L. Hia, V. Vahedi, and P. Pasbakhsh, "Self-Healing Polymer Composites: Prospects, Challenges, and Applications," *Polymer Reviews,* vol. 56, no. 2, pp. 225-261, 2016/04/02 2016.

Acknowledgements

The authors are grateful to the Secretaria de Investigación y Posgrado (SIP) of IPN through the SIP20251064 project, as well as SNII, SECIHTI and Loughborough University.

Polymat Contributions

DNA COMPLEXATION WITH POLY-L-LYSINE AND A NOVEL ANALOGUE POLY-N-LYSINE FOR GENE DELIVERY

Lizeth M. Bravo-Lozano[1,2*], Edgar Figueroa-Ochoa[2], Eduardo Mendizábal-Mijares[2], Colin Bonduelle[3], Sylvain Tranchimand[4], Pascal Loyer[5], L. Mónica Bravo-Anaya[1]**

[1] Institut des Sciences Chimiques de Rennes, Université de Rennes, Rennes, France
[2] Departamento de Ingeniería Química, Universidad de Guadalajara, México
[3] Université de Bordeaux, LCPO, Bordeaux, France
[4] ENSCR, Université de Rennes, Rennes, France
[5] Université de Rennes, Inserm, INRAE, Institut NUMECAN, Rennes, France.
**Lizeth.bravo2900@alumnos.udg.mx, **lourdes-monica.anaya@univ-rennes.fr*

INTRODUCTION

Today, the rising incidence of diseases such as cancer, along with the challenges presented by genetic disorders, has driven the development of new nucleic acid–based therapies capable of improving human health safely and effectively. Gene therapy has emerged as a particularly promising approach, as it involves the transport and transfer of genetic material to specific cells for the treatment of diseases [1]. This strategy requires identifying an appropriate therapeutic gene and ensuring its efficient transfer to the target cells so it can carry out its intended role. To compact, protect, transport and ultimately release this genetic material, an appropriate vector is essential [2].

The negative charges on the nucleic acid backbone enable natural or synthetic polycations to bind DNA or RNA through electrostatic interactions, forming particles known as polyelectrolyte complexes (PECs). These complexes have been widely studied as non-viral vectors for nucleic acid-based therapies, including gene therapy [3]. Compared with other PEC systems that rely on cationic polymers such as polyethyleneimine (PEI), highly efficient but markedly cytotoxic, or chitosan, which exhibits limited transfection efficiency, synthetic polypeptides like poly-L-lysine (PLL) have gained particular interest in recent years due to their biocompatibility, facility of synthesis, and tunable chemical modification [4]. Despite significant advances, current knowledge remains insufficient to fully describe the mechanisms governing the formation, stability and dissociation of gene-delivery complexes, limiting our understanding of their behavior under physiological conditions.

One of the major challenges in this field is identifying and optimizing non-viral vectors that not only protect and transport genetic material but also provide adequate transfection efficiency along with high biocompatibility [5]. Within this context, poly-L-lysine (PLL) remains a promising candidate, yet its physicochemical and biological properties are not fully understood. This research aims to explore the characteristics and differences of polyelectrolyte complexes formed between plasmid DNA and two polycations: conventional poly-L-lysine (PLL) and a novel analogue, poly-N-lysine (PNL). The project will provide a comprehensive characterization of PLL/DNA and PNL/DNA complexes, with particular attention to their stoichiometry, stability and behavior under biologically relevant conditions. The main goal is to improve the basis for the rational design of safe and effective gene-delivery vectors.

MATERIALS AND METHODS

Six polycation samples were used: three poly-N-lysines (PNL) with degrees of polymerization (DP) of 20, 50, and 100, and three poly-L-lysines (PLL) with DP values of 30, 60, and 100. All polymers were synthesized at the Laboratoire de Chimie des Polymères Organiques (LCPO), University of Bordeaux, France. The eGFP-C3 plasmid ($3x10^6$ g/mol) was produced in *Escherichia coli* and purified using a NucleoBond PC10000 genomic DNA kit (Thermo Scientific) at the University of Rennes, France. These materials were used to study the formation of PNL/peGFP-C3 and PLL/ peGFP-C3 polyelectrolyte complexes. The stoichiometry of the complexes was first evaluated by gel electrophoresis and ζ-potential measurements. We then examined how the polycation structure, DP, and charge ratio (R = $[N^+]/[P^-]$ = 3, 5, 10, and 15) influenced the hydrodynamic diameter, polydispersity index (PDI), and ζ-potential. Measurements were taken at 25 °C using a Zetasizer Nano ZS (Malvern) with a detection angle of 173°. Colloidal stability was studied through DLS by monitoring changes in particle size in the presence of PBS and cell culture medium (used later for transfection assays). To evaluate stability over time, the initial particle size was taken as a reference. Complexes were stored at 4 °C, and their hydrodynamic diameter (D_H) was measured daily for seven consecutive days. To study the dissociation of PLL_{100}/peGFP-C3 complexes in the presence of competing biological polyanions, we used heparin. DNA release was monitored by adding increasing amounts of heparin and analyzing the samples by gel electrophoresis. For transfection studies, HEK293T cells were cultured in DMEM supplemented with 10% FBS, L-glutamine, and antibiotics. Cells were seeded at 2 $x10^4$ cells/cm^2 and transfected in PBS buffer (pH 7.4). After daily medium changes, the transfection efficiency was determined 5 days post-transfection by observing peGFP-expressing cells under a fluorescence microscope.

RESULTS AND DISCUSSION

Stoichiometry determination

Figures 1a and **1b** show the evolution of the ζ-potential of the peGFP-C3 plasmid DNA solution after the addition of PLL (a) and PNL (b), resulting in the formation of PLL/peGFP-C3 and PNL/peGFP-C3 complexes, respectively. A significant difference was observed in the volume of polycation added at a concentration of 0.5 mg/mL necessary to reach the isoelectric point (IP) between both structures, suggesting variations in their charge density and complexation capacity [6]. Based on the obtained stoichiometric values, complexes were then prepared at four defined charge ratios, R=$[N^+]/[P^-]$ = 3, 5, 10 and 15, using a one-shot mixing method followed by rapid vortexing.

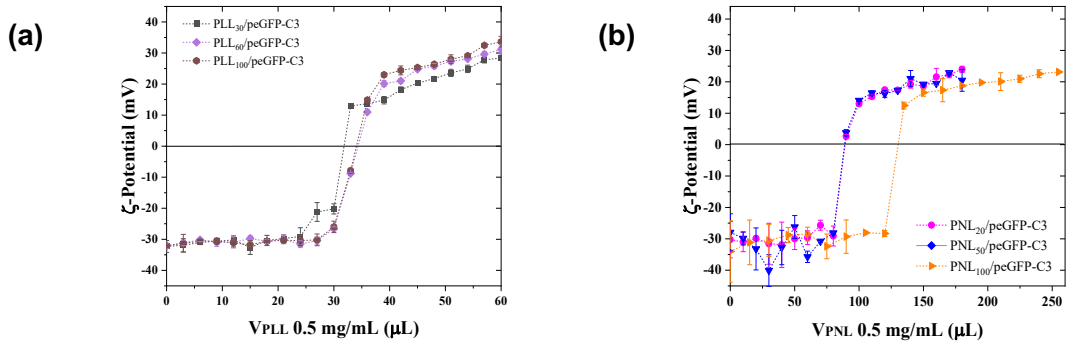

Figure 1. ζ-Potential as a function of polypeptide volume during complexes formation: (a) PLL/peGFP-C3 and (b) PNL/peGFP-C3, using an initial plasmid solution of 5 mL at 0.005 mg/mL, and polypeptide solutions DP = 20, 50, and 100, prepared at 0.5 mg/mL at a pH of 7.4.

Complexes formation and characterization

ζ–potential measurements revealed clear differences between complexes formed with the four PLL samples and the three PNL samples, with the PNL-based complexes exhibiting lower surface charge values (**Figure 2a**). Dynamic light scattering (DLS) analysis showed that all complexes exhibited comparable average D_H, ranging from 50 to 100 nm across all formulations (**Figure 2b**). These results indicate that neither the degree of polymerization (DP) nor the molecular weight significantly influence complex compaction.

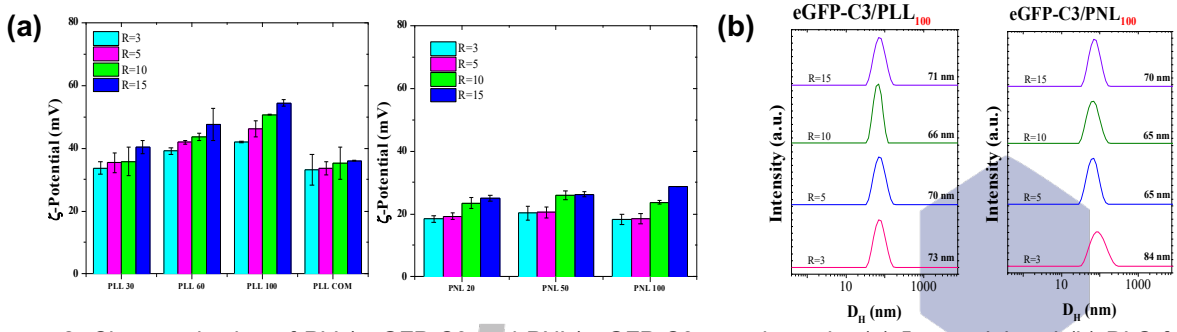

Figure 2. Characterization of PLL/peGFP-C3 and PNL/peGFP-C3 complexes by (a) ζ-potential and (b) DLS for R=3, 5, 10 and 15.

Complexes stability

DLS measurements revealed that PNL-based complexes exhibit lower colloidal stability in biological media than PLL-based complexes, particularly at low degrees of polymerization (**Figure 3a**). In contrast, complexes prepared with the highest DP (60 and 100) remained relatively stable for at least seven days when stored at 4 °C (**Figure 3b**).

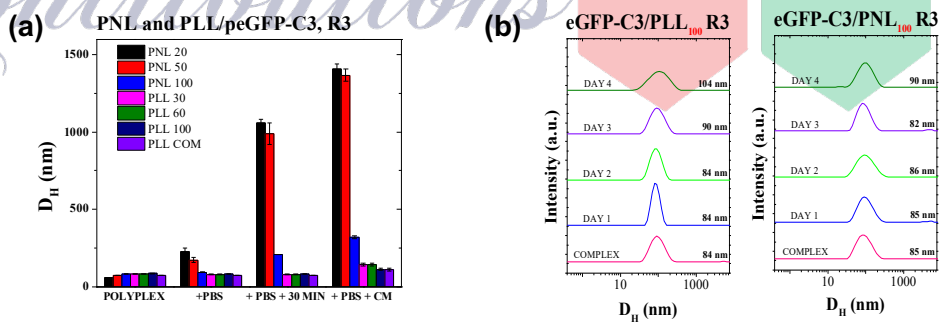

Figure 3. Stability evaluation of PLL/peGFP-C3 and PNL/ peGFP-C3 complexes: (a) average particle size evolution in biological media at R = 3; (b) evolution of D_H distribution for complexes at R = 3 over seven days.

Complexes dissociation in presence of competitive polyanions

The stability of the complexes in the presence of heparin was evaluated to assess their sensitivity to competitive interactions with glycosaminoglycans (GAGs) (**Figure 4**). This analysis confirmed strong electrostatic interactions and showed that complex stability increases with higher charge ratios (R), as more heparin is required to release the plasmid. From these experiments, the heparin concentration needed to fully dissociate each complex formulation was determined.

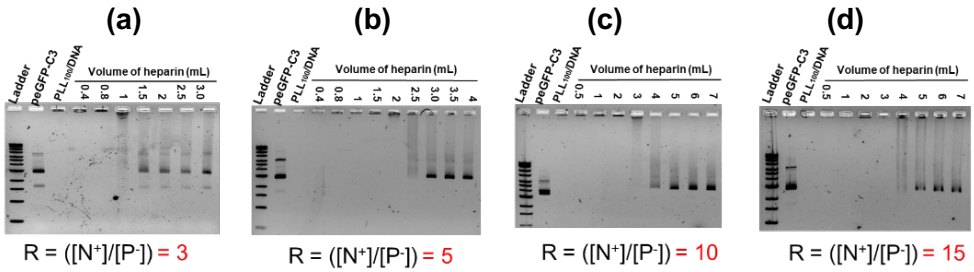

Figure 4. Dissociation profiles, obtained from electrophoresis assays of PLL_{100}/peGFP-C3 complexes exposed to heparin at R = 3 (a), 5 (b), 10 (c), and 15 (d).

Cells transfection

Preliminary transfection studies in HEK293T cells (**Figure 5**) revealed detectable GFP expression for both PNL/peGFP-C3 and PLL/peGFP-C3 complexes. Furthermore, cells transfected with PNL/peGFP-C3 presented higher cell viability, suggesting that the analogous polycation may be less cytotoxic.

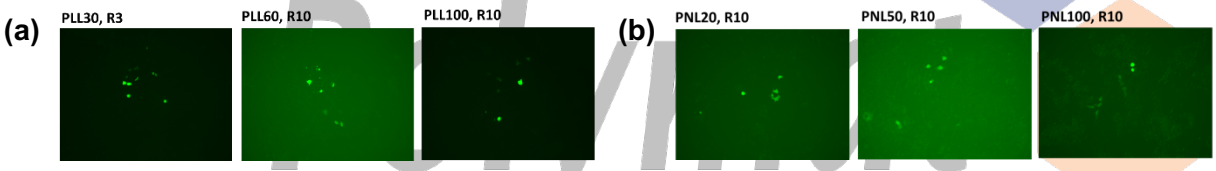

Figure 5. GFP protein expression in HEK cells transfected by (a) PLL/peGFP-C3 and (b) PNL/peGFP-C3 complexes.

CONCLUSIONS

Clear differences were observed between complexes formed with the classical PLL structure and those prepared with the analogous PNL structure. PLL/peGFP-C3 complexes displayed higher stability in biological media and required smaller volumes of polycation to reach stoichiometry. An increase in the charge ratio (R) led to a progressive decrease in particle size, most likely corresponding to enhanced plasmid condensation. Furthermore, PLL/peGFP-C3 complexes were susceptible to destabilization in the presence of heparin, with higher heparin concentrations required for plasmid release as R increased.

References

[1] Cavazzana-Calvo et al. *Nature*. **2004**, 427(6977):779-781.
[2] Alinejad-Mofrad et al., *Human and Experimental Toxicology* **2019,** 38(8), 983-991.
[3] Bravo-Anaya et al., *Journal of Colloid and Interface Science* **2019,** 557, 777-792.
[4] Yang J, Luo GF. *Chemistry (Easton)*. **2023**, 5(3):1696-1718.
[5] Dhurandhar et. al. Indian Journal of Ophthalmology, **2021**, 69(9), 2257-2265.
[6] Naassaoui, I., & Aschi, A. Journal of Macromolecular Science **2019**, 58(8), 673-688.

Acknowledgements

The authors wish to acknowledge the SECIHTY for the Master Scholarship granted to Lizeth Bravo Lozano and to the CNRS-IEA P^2NanoBio for funding the collaboration between México and France. Lizeth Bravo Lozano wishes to acknowledge Dr. Lourdes Mónica Bravo Anaya and Dr. Eduardo Mendizábal Mijares for their support in the development of this project in France and Mexico, respectively.

Polymat Contributions

COPOLYMER MICELLES FORMED WITH A COMBINATION OF PLURONICS® F127 AND P104 USED AS EFFICIENT NANOCARRIERS FOR THE LOADING AND RELEASE OF DOXORUBICIN

Charlotte Bellec[1,2], Ramón A. Gutiérrez-Saucedo[2], Alberto Gutiérrez Becerra[3], Lourdes Mónica Bravo-Anaya[4], Edgar B. Figueroa Ochoa[1]

[1]Laboratorio de Proyectos Modulares, Departamento de Química, CUCEI, Universidad de Guadalajara, Blvd. M. García Barragán 1421, Guadalajara 44430, Jalisco, México.
[2]Université de Bordeaux, ENSMAC, 16 avenue Pey Berland, 33607 Pessac Cedex, France, charlotte.bellec@bordeaux-inp.fr
[3] Departamento de Ciencias Básicas, CUTonalá, Universidad de Guadalajara, México.
[4] Université de Rennes, Institut des Sciences Chimiques de Rennes, Équipe CORINT, CNRS, UMR 6226,
Campus de Beaulieu, Bat 10A, 35042 Rennes Cedex, France

Abstract

Cancer affects nearly 20 million people worldwide each year [1], and current treatment options remain highly invasive, often leading to serious adverse effects. Chemotherapy, in particular, can cause alopecia and severe reductions in white blood cell counts, leaving patients sceptible to severe infections. These limitations highlight the urgent need for advanced drug delivery strategies, such as nanocarriers, that can enhance therapeutic targeting while reducing systemic toxicity. Among the various nanocarrier platforms, Pluronics®, a family of triblock copolymers composed of poly(ethylene oxide)-poly(propylene oxide)-poly(ethylene oxide) (PEO-PPO-PEO), are widely employed in pharmaceutical formulations due to their excellent biocompatibility, colloidal stability, and ability to solubilize diverse bioactive compounds through micelle formation in aqueous media [2]. Furthermore, their thermosensitive behavior enables the development of stimuli-responsive delivery systems. Within this family, Pluronics® F127 and P104 are particularly noteworthy for their capacity to self-assemble into stable micelles capable of encapsulating chemotherapeutic agents.

In this project, Pluronics® F127 and P104 were combined in a novel formulation designed to form thermosentisitve micelles for the transport and controlled release of doxorubicin (DOXO), a hydrophobic and photosensitive anthracycline anticancer drug. This drug acts intercalating between DNA base pairs, inhibiting DNA replication and transcription. Aqueous solutions containing mixtures of P104 and F127 were firstly characterized by Dynamic Ligth Scattering (DLS) to identifiy the formation of copolymer micelles. Then, we determined the influence of the proportion of each copolymer on drug encapsulation, micelle stability and DOXO release. For these, DOXO was encapsulated within the copolymer micelles using a centrifugation and filtration process. The encapsulation capacity was analyzed through the determination of drug loading (D.L.), entrapment efficiency (E.E.), and solubilization capacity per gram of copolymer in solution (Scp). Micelle stability was determined by measuring the size of pure micelles and those loaded with DOXO through DLS. Drug releseae studies were performed by placing the loaded micellar solutions in dialysis tubes immersed in different PBS media [1].

The release profile was evaluated at various pH and analyzed using the Higuchi, Korsmeyer–Peppas and Peppas–Sahlin diffusion models[2].

Methods

Micellar solutions were prepared by dispersing the polymers in water and allowing them to self-assemble via diffusion (**Figure 1**). The spherical morphology of the micelles was examined by studying the turbidity and birefringence under crossed polarizers.

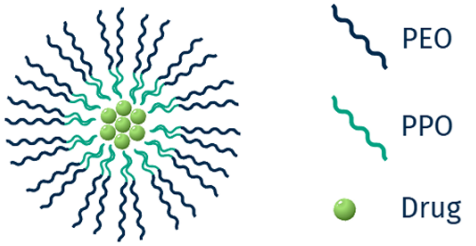

Figure 1: Schematic representation of a micelle formed by Pluronics® encapsulating anticancer drugs.

Drug loading was performed by combining the micellar solution with a dichloromethane solution of hydrophobic doxorubicin (DOXO base) under continuous stirring [4]. After evaporation of the dichloromethane, doxorubicin was encapsulated within the micelles. The loaded solution was subsequently centrifuged to remove any residual free drug and then filtered to retain only the loaded micelles.

Dynamic light scattering (DLS) was used to determine the particle size distribution [5], enabling comparison between empty and DOXO-loaded micelles and confirming successful drug encapsulation. Multiple doxorubicin concentrations were tested to identify the most efficient loading conditions, which were then used for further studies. The optimized formulation consisted of a 3 % polymer micellar solution with a 60:40 F127:P104 ratio, loaded with 60 µg/mL of doxorubicin.

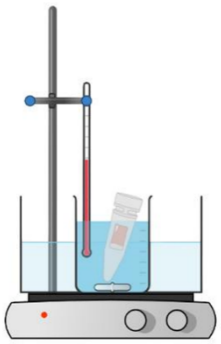

Figure 2: Diagram of the release system.

Drug release studies were performed using dialysis tubes immersed in 250 mL of release medium under controlled temperature and pH conditions. The tested conditions were: 37 °C at pH 7.4 (simulating parenteral administration), 37 °C at pH 5.5 (simulating intestinal fluid), and 20 °C at pH 7.4 (simulating ambient storage). To enhance drug diffusion across the membrane and minimize aggregation, 2 % (v/v) ethanol was added to the medium (**Figure 2**) [6]. At predetermined intervals, 2 mL samples were collected from the release medium and replaced with fresh PBS.

Results

DOXO (base) was added to 2 mL of polymeric micellar solutions containing either 50 (w/w)% F-127 / 50 (w/w)% P-104 or 60 (w/w)% F-127 / 40 (w/w)% P-104. The DOXO concentrations tested ranged from 10 to 100 µg/mL. The amount of drug encapsulated in each micellar solution was quantified by UV-Vis spectrophotometry (λ= 480 nm) [7]. Increasing the amount of DOXO added to the Pluronic® F-127 micellar solutions resulted in a corresponding increase in the encapsulated drug until a saturation point was reached, at which the entrapment efficiency was maximal (**Figure 3**). For the 60 (w/w)% F-127 / 40 (w/w)% P-104 micellar system, the solubilized drug reached its maximum at saturation, with an encapsulation efficiency of 48.3%. Encapsulation efficiencies were similar for both 3 % and 5 % polymer systems; therefore, to optimize the use of raw materials, subsequent experiments were carried out using the 3 % polymer system.

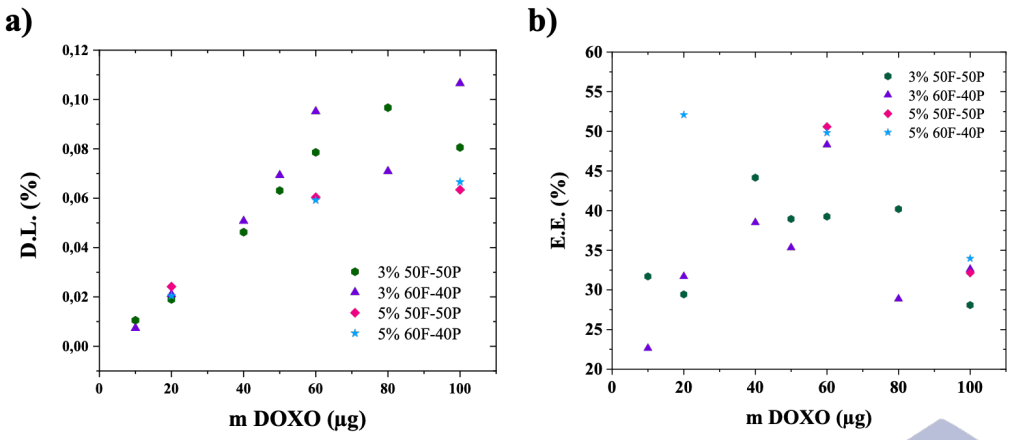

Figure 3. Comparison of doxorubicin loading (a) and entrapment efficiency (b) for the different micellar formulations with doxorubicin.

The size of DOXO-loaded micelles formed from Pluronic® F127 and P104 triblock copolymers was measured by Dynamic Light Scattering (DLS) at 25 °C. All samples were equilibrated at the measurement temperature for 3 minutes prior to analysis. The micellar solutions appeared fluid, homogeneous and transparent. **Figure 4a** shows the particle size distributions of both empty and drug-loaded F127 and P104 micelles. For the empty mixed F127/P104 micelles at 25 °C, the dominant peak corresponds to a particle diameter of 24.4 nm. Upon loading with 60 µg/mL of DOXO base, the primary peak shifted dramatically to 450 nm, indicating micelle enlargement upon drug encapsulation.

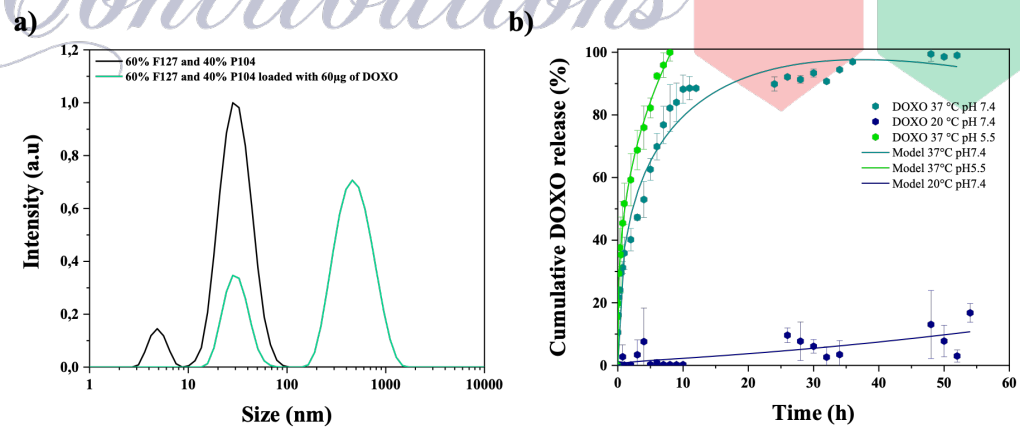

Figure 4.- a) Particle size distribution at 25 °C of unloaded and DOXO-loaded micelles prepared from a combination of Pluronics® P104 and F127. b) In vitro release profiles of DOXO from the loaded micelles at 37 °C under pH 7.4 and pH 5.5, and at 20 °C under pH 7.4.

Furthermore, the particle size distribution was relatively narrow, indicating uniformity in both shape and composition of the mixed F127/P104 micelles. These results are consistent with previous studies evaluating the potential of micellar nanostructures for the delivery of various antineoplastic and antifungal drugs [8]. **Figure 4b** shows the DOXO release profiles from the

micellar solutions under conditions simulating physiological environments (37 °C at pH 7.4 to mimic blood transport, and pH 5.5 to represent intestinal fluid) and storage conditions (20 °C at pH 7.4). The release kinetics were modeled using the Peppas-Sahlin model [9]. At 37 °C and pH 7.4, DOXO release was rapid, with approximately 80 % of the drug released within 10 hours. Release was even faster at pH 5.5, with nearly complete release within 8 hours. In both cases, an initial burst effect occurred during the first hours, followed by a pronounced slowdown, eventually reaching a near-plateau. In contrast, at 20 °C, drug release was minimal, reaching only 10 % after 54 hours (2 days and 6 hours), indicating that storage at this temperature does not significantly affect the stability of the DOXO-loaded micelles.

Conclusions

This study demonstrates that micelles formed from Pluronics® F-127 and P-104 are effective nanocarriers for the encapsulation and controlled release of anticancer drugs such as DOXO. The optimized formulation, comprising 3 % polymers with a 60:40 ratio of F-127 to P-104, exhibited good encapsulation efficiency, while the release kinetics could be precisely modulated by adjusting pH and temperature. These results highlight the potential of these amphiphilic copolymer systems to provide targeted and adaptable drug administration, improving therapeutic efficacy while minimizing side effects. Overall, this project underscores the promising prospects of advanced micellar nanostructures for the development of next-generation anticancer therapies.

References

[1] F. Bray, M. Laversanne, H. Sung, J. Ferlay, R.L. Siegel, I. Soerjomataram, A. Jemal, *CA Cancer J. Clin.* 2024, 74 (3), 229-263.

[2] R.A. Gutiérrez-Saucedo, J.C. Gómez-López, A.A. F.Villanueva-Briseño, A. Topete, J.F.A. Soltero-Martínez, E. Mendizábal, C.F. Jasso-Gastinel, P. Taboada, E.B. Figueroa-Ochoa, *Polymers* 2023, 15(10), 2249.

[3] M. Elsabahy, M.É. Perron, N. Bertrand, G.E. Yu, J.C. Leroux, *Biomacromolecules* 2007, 8, 2250–2257

[4] P. Taboada, G. Velasquez, S. Barbosa, V. Castelletto, S. Nixon, Z. Yang, F. Heatley, I. Hamley, M. Ashford, V. Mosquera, et al., *Langmuir* 2005, 21, 5263–5271.

[5] K.K. Upadhyay, A. Bhatt, E. Castro, A. Mishra, K. Chuttani, B. Dwarakanath, C. Schatz, J. Le, A. Misra, S. Lecommandoux, *Macromol. Biosci.* 2010, 10, 503–512.

[6] E.B. Figueroa-Ochoa, E. Villar-Álvarez, A. Cambón, D. Mistry, J. Llovó, D. Attwood, S. Barbosa, J.A. Soltero, P. Taboada, *Int. J. Pharm.* 2016, 510, 17–29.

[7] N.A. Peppas, J.J. Sahlin, *Int. J. Pharm.* 1989, 57, 169–172.

Acknowledgements

I would like to express my sincere gratitude to CUCEI for their warm welcome and for providing the resources and support essential for this research. I am also deeply thankful to ENSMAC for sharing the knowledge and opportunities that made this work possible. I wish to acknowledge all collaborators who contributed to this project, in particular Mr. Edgar Figueroa, Mrs. Mónica Bravo, and Mr. Sébastien Lecommandoux, for their valuable guidance and advice. Finally, I gratefully acknowledge the IEA P_2Nanobio from CNRS for supporting the collaborative efforts between Mexico and France.

Milling and sintering conditions effect on the solid-state processing of BCZT ceramics

A. L. Conejo-Martínez [1,2*], M. Mureddu[3], L. Pardo[4], A. Reyes-Montero[2].

*[1]Facultad de Química, Universidad Nacional Autónoma de México, Circuito Exterior s/n, Cd. Universitaria, Coyoacán, C. P. 04510, CDMX, Mexico. *ana.conejo.mtz@gmail.com*

[2]Instituto de Investigaciones en Materiales, Universidad Nacional Autónoma de México, Circuito Exterior s/n, Cd. Universitaria, Coyoacán, C. P. 04510, CDMX, Mexico.

[3]Department of Chemical, Physical, Mathematical, and Natural Sciences, University of Sassari, Italy.

[4]Instituto de Ciencia de Materiales de Madrid (ICMM). Consejo Superior de Investigaciones Científicas, c/ Sor Juana Inés de la Cruz, 3. 28049-Madrid, Spain.

Abstract

Lead-free $Ba_{0.85}Ca_{0.15}Ti_{0.9}Zr_{0.1}O_3$ ferroelectric ceramics were synthesized by the solid-state route using two mechanically activated methods with short milling times: conventional (CS) and reactive sintering (RS). TGA and XRD confirmed that mechano-activation by high energy planetary milling lowers the synthesis temperature. Pellets sintered by CS and RS methods developed pseudocubic perovskite phases and characteristic microstructures, depending on the sintering temperature and processing technique.

Introduction.

Ferroelectric ceramic materials are of significant importance to scientific community, due to their variety of applications in industry as sensors and electromechanical trasducers. Their ability to convert mechanical energy into electrical energy, and vice versa, has positioned them as a fundamental element in energy-related issues. Nowdays, lead-based materials dominate the global market. Due to lead-oxide toxicity, efforts have been made in search for environmentally friendly, lead-free, ceramics [1]. Currently, an important candidate for this replacement is the solid solution formed by $BaTiO_3$-$CaTiO_3$-$BaZrO_3$: $(Ba,Ca)(Ti,Zr)O_3$, due to the existence of morphotropic phase boundaries (MPB) with coexistence of ferroelectric phases. However, the challenge for generating optimum ceramic materials persist in order to achieve an optimized microstructure, required for an enhanced piezoelectric and ferroelectric performance.

The processing technique highly influences on the final electrical characteristics of the ceramics. The milling process allows the mechanical activation of the reacting species (reduction of powder particles and surface modifications) before the synthesis of the material. Energetic milling processes produces a decrease in the synthesis temperature along with an homogenous grain growth and, under certain conditions, it has been shown that they can result in mechanosynthesis [2], [3], [4]. Then, to use an efficient milling process becames a cruzial step for design of a energy-efficient solid-state processing route.

Processing BCZT carries the risk of generating secondary phases that may persist in the final ceramic microstructure and adversely affect the electrical properties of the material [5]. Additionally , sintering BCTZ ceramics typically requires high temperatures and long dwell times, which translates into significant energy consumption. In this context, reactive sintering emerges as an attractive processing route. Reactive sintering is a one-step method in which the solid-state reaction and densification occur during the same thermal cycle. This approach has been shown to lower the energetic requirements of sintering, in some instances due to the formation of a transient liquid phase that promotes ion diffusion and accelerates the solid-state reaction before disappearing during the later stages of sintering. Such behavior can reduce the kinetic

barriers associated with diffusion and phase formation, enabling densification at lower temperatures [6]. This route therefore appears promising for obtaining dense BCTZ ceramics.
In this work, two processing routes are explored for the development of $Ba_{0.85}Ca_{0.15}Ti_{0.90}Zr_{0.10}O_3$ ceramics, hereinafer called BCZT. The microestructural and structural characterization is accomplished and the results are discussed.

Experimental

Two processing routes were explored. (figure 1).

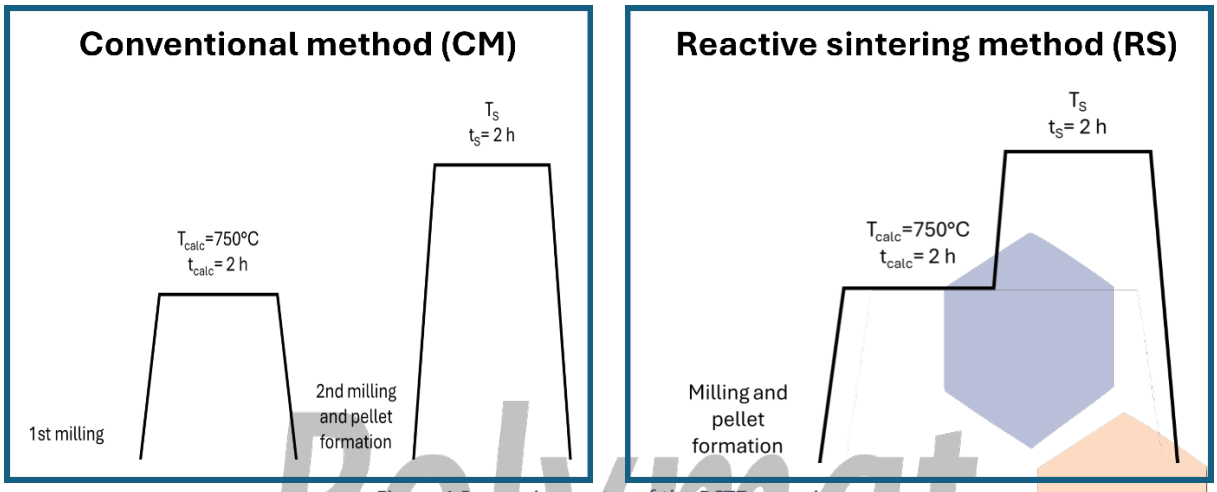

Figure 1 Processing routes of the BCTZ ceramics.

For the conventional method (CM), the reactant mixture was milled in a planetary mill using a 85 ml Zirconia jar with 3 mm Zirconia balls and isopropanol as the medium. Preliminary tests were carried our to optimize the process. As a result of these, milling was carried out at 550 rpm with a mass ball-to-powder ratio of 20:1, using short milling times (1, 3, and 6 h). Afterwards, powders were calcined at 750°C for only 2 h. A second milling process was perfomed (3h) using same conditions, then powders were uniaxially pressed at 3 ton into pellets of ~13.0mm in diameter and ~1.5mm in thickness and sintered at 1200, 1300 and 1400°C for 2h.
For the reactive sintering (RS), the reactants mixture was milled under the same conditions using the optimum milling time of 6h. Same conditions as for the CM method were followed to produce pellets. Then, ceramics were treated by a two-steps thermal profile, the first dwell at 750°C for 2 h and the second at 1200, 1300 and 1400°C for 2h.
Milled powders were characterized by Thermogravimetric Analysis (TGA) using a TGA 2950 (TA-Instruments) from ambient temperature up to 900°C. The phase structure of BCTZ synthesized power and ceramics was analyzed using X-ray (XRD) diffraction with a Cu-kα radiation (1.5419 Å, Rigaku Ultima IV with a 0.02° step size in 2θ). Morphology of the samples was analyzed by a field emission scanning electron microscope (SEM) (JEOL J7600f). Ceramic density was obtained by the Archimedes method.

Results and discussion

The effect that the milling time has on the thermal evolution of the raw materials mixture is shown in figure 2. TGA analysis evidenced the higher reduction of the temperatures with time for the decarbonization (zone I) and the synthesis (zone II) for the higher milling time. Moreover, the X-ray diffraction (XRD) patterns, at different calcination temperatures (figure 2b), revealed the evolution from the BCTZ synthesis to the sintering process. It is observed that at 750°C the perovskite phase is formed although traces of the reactant mixture remain. The BCTZ phase was verified with the ICDD-PDF-00-070-0583 file.

The calcined powder, after a second milling treatment that ensures to enhance sintering process of the BCTZ materials [7], was used to form the CM ceramic pellets. The as milled powder for 6h was used to form the RS ceramic pellets, as the reactiveness of the reactant mixture after milling ensures to enhance synthesis process (fig.2a) and we aim to test the effect on the crystal structure and ceramic microstructure after RS.

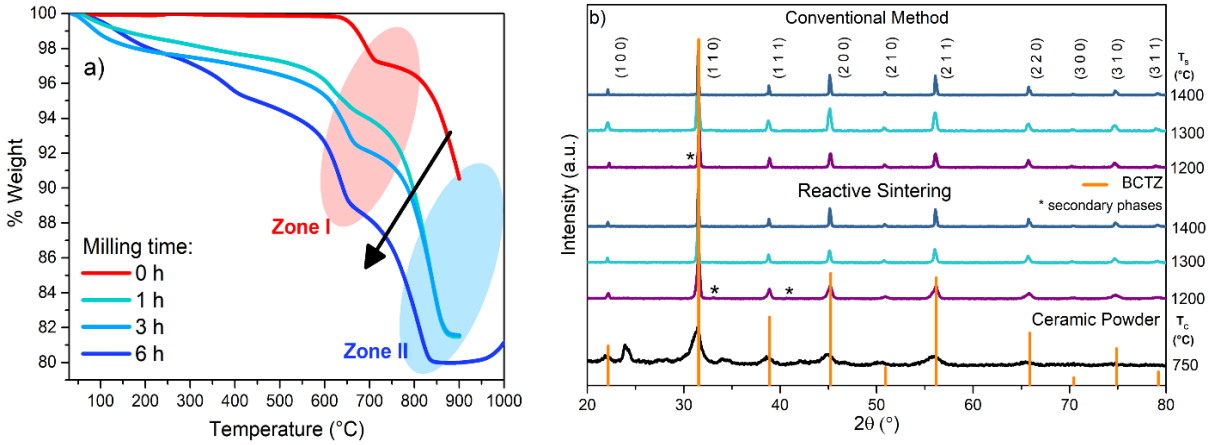

Figure 2. a) TGA of milled powders and b) XRD patterns of milled reactant mixture and calcined BCTZ powders.

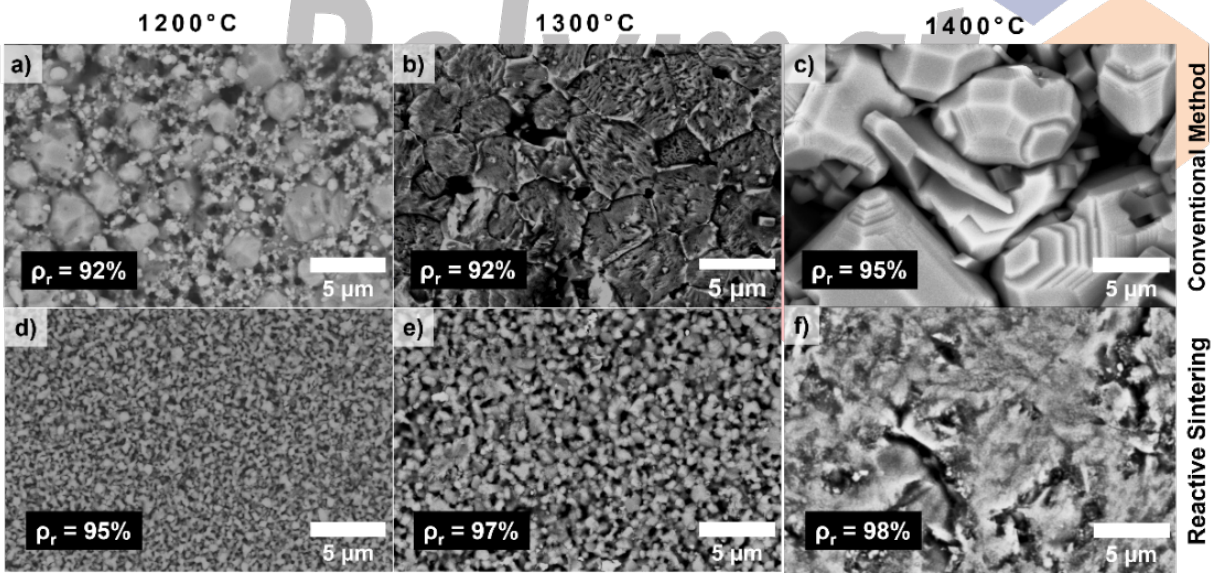

Figure 3. SEM images of sintered pellets. Relative density calculated from a given theoretical density of 5.86 g/cm^3.

Figure 2b shows the XRD patterns of the sintered ceramics, at different temperatures, produced by the CM and RS process. For both methods a complete solid solution was formed at 1300 and 1400°C, as revealed by the pure BCTZ crystal structure (fig. 2b). The diffraction peaks of the samples were indexed to the perovskite-type cubic prototype phase. The pseudo-cubic structure most probably reveals a coexistence of polymorphs.

SEM micrographs (figure 3) revealed a strong correlation between grain growth, the sintering temperature and the ceramic processing. In figure 3a the presence of two, or even three, families of grain size is evident. The smallest size grains could be partly unreacted powder, which is consistent with the residual signals observed in the XRD pattern of CS ceramics sintered at 1200ºC (fig. 2b). However, as the XRD signals intensity could correspond to some 3 to 5% of

content of secondary phases and the fraction of small grains in fig. 3a is much higher, it is reasonably to think that some of the small grains have BCZT composition, but did not grow under these sintering conditions. CS at higher temperatures produces well developed grains and homogeneous microstructures. In contrast, pellets processed through the RS method (figures 3 d, e and f) exhibited significantly homogeneous microstructures with smaller grain sizes across all temperatures. Finally, even when all the sintered pellets have a relatively high density (>90%), the RS method showed a tendency to produce higher densities. It can be reasonably speculated that during molding, the packing of the nanometer-size particles of the milled reagents mixture for 6h for RS route could be better than that of the particles of the synthesized powder milled for 3h for the CS one. While the former develops in denser fine-grained microstructures, the latter gives place to higher grain size ceramics with higher porosity.

Conclusions

BCTZ ceramics were successfully prepared by solid-state reaction using two processing methods. It was found that the fast-milling process of reagents used here reduces the synthesis temperature. After sintering at 1300 and 1400ºC, both types of BCZT ceramics exhibited single phase pseudocubic crystal structure. RS ceramics show dense and fine-grained microstructure, while CS ceramics shows higher grain sizes and slightly higher porosity. The functional ferroelectric, dielectric and piezoelectric properties will be addressed in future work.

References

[1] T. Zheng, J. Wu, D. Xiao, and J. Zhu. Recent development in lead-free perovskite piezoelectric bulk materials. *Prog. Mater. Sci.* vol. 98, pp. 552-624, 2018.

[2] M.J. Sayagués, A. Otero, L. Santiago-Andrades, R. Poyato, M. Monzón, R. Paz, F.J. Gotora, R. Moriche. Fine-grained BCZT piezoelectric ceramics by combining high-energy mechanochemical synthesis and hot-press sintering. *J Alloys Compd*, vol. 1007, p. 176453, 2024.

[3] M. Mureddu . Solid State Processing of BCZT Piezoceramics Using Ultra Low Synthesis and Sintering Temperatures. *Materials*, vol. 16, no. 3, p. 945, 2023.

[4] H. Amorín, M. Venet, E. Chinarro, P. Ramos, M. Algueró, and A. Castro, "Lead-free $Ba_{0.85}Ca_{0.15}Zr_{0.1}Ti_{0.9}O_3$ ferroelectric ceramics with refined microstructure and high strain under electric field by mechanosynthesis," *J Eur Ceram Soc*, vol. 42, no. 12, pp. 4907–4916, 2022.

[5] A. M. Paulik, S. Kunz, M. Widenmeyer, O. Clemens, A. Weidenkaff, and J. Koruza. Solid-state formation reactions of $Ba_{0.82}Ca_{0.18}Zr_{0.08}Ti_{0.92}O_3$ piezoceramics. *J Eur Ceram Soc*, vol. 46, no. 1, 2026.

[6] C. Baudín, 'Reaction Sintering', *Encyclopedia of Materials: Technical Ceramics and Glasses: Volume 1-3*, vol. 1, pp. V1-278-V1-285, 2021.

[7] A. Reyes-Montero, L. Pardo, R. López-Juárez, A. M. González, S O Rea-López, M P Cruz and M E Villafuerte-Castrejón. Sub-10 μm grain size, Ba1−xCaxTi0.9Zr0.1O3 (x = 0.10 and x = 0.15) piezoceramics processed using a reduced thermal treatment," *Smart Mater Struct*, vol. 24, no. 6, p. 065033, 2015.

Acknowledgements

Armando Reyes-Montero acknowledges UNAM-DGAPA (PAPIIT IN115625) for financial support. The authors thank LUME team from LUME RRID:SCR_024400 for SEM image acquisition and technical support. Also, authors thank Karla Eriseth Reyes Morales (IIM-UNAM) for TGA acquisition and technical support. Ana Laura Conejo-Martínez also thanks PITAAE-UNAM and DGECI-UNAM for the financial support of a 3 months stay at ICMM (Spain).

FORMATION AND STABILITY OF POLYPEPTIDE/ENZYME COMPLEXES FOR BIOCATALYSIS

Paulina Itzel DÍAZ FLORES*[1,2], María Fernanda ULLOA JAIMES[1,2], Alberto GUTIÉRREZ BECERRA[2], Marcela AYALA ACEVES [3], Colin BONDUELLE[4], Lourdes Mónica BRAVO-ANAYA[1]**

[1] Institut des Sciences Chimiques de Rennes, Université de Rennes, Rennes, France
[2] Departamento de Ciencias Básicas, CUTonalá, Universidad de Guadalajara, México.
[3] Instituto de Biotecnología, UNAM, Cuernavaca, Morelos, México.
[4] Université de Bordeaux, LCPO, Bordeaux, France
*paulina.diaz6600@alumnos.udg.mx, **lourdes-monica.anaya@univ-rennes1.fr*

Abstract

Proteins are versatile macromolecules, performing biological functions through binding, catalysis, stimuli responsiveness, and as matrix components. Enzymes, in particular, are valuable for catalyzing diverse reactions. However, stabilizing them outside their natural environment remains challenging, and their protection with synthetic materials is still limited. Enzymes can form complexes with oppositely charged polymers, which can protect them and preserve bioactivity. In this study, two synthetic polypeptides, *i.e.* poly-L-lysine (PLL) and its analogue, poly(N-aminobutyl)glycine (PNL), with varying degrees of polymerization (DP_{PLL}: 20, 50, 100; DP_{PNL}: 30, 60, 100) were used to investigate complex formation and stability with chloroperoxidase (CPO) and versatile peroxidase (VP). ζ-potential measurements were used to determine the stoichiometry of PLL/VP, PNL/VP, PLL/CPO, and PNL/CPO complexes. Scanning Electron Microscopy (SEM) showed spherical complexes in the nanometer range, with size variations depending on the polypeptit, DP, enzyme and charge ratio (R=[+]/[-], molar concentrations of positively charged groups from polypeptides and negatively charged groups from the enzyme, respectively). Circular dichroism showed a slight evolution of the secondary structure of the enzymes in the complexes. The complexes were pH-responsive, swelling as pH decreased from 6 to 4. These results provide a foundation for further studies of CPO and VP enzymatic activity in the presence of PLL and PNL.

Introduction

Biocatalysis, through the use of enzymes, plays an important role in a wide range of fields, particularly in the chemical, pharmaceutical and healthcare industries. Enzymatic catalysis offers exceptionally high reaction rates and selectivities that are often impossible with conventional small-molecule catalysts, allowing highly efficient and environmentally friendly transformations [1]. This unique capability positions enzyme-based processes as attractive alternatives or complements to traditional chemical methods [2]. However, despite their advantages, enzymes frequently exhibit limited stability under non-natural conditions, such as extreme temperatures, the presence of organic solvents, pH variations, and mechanical agitation, which restrict their broader industrial applications [2]. Various strategies have been explored to improve enzyme stability, including immobilization, chemical modification and encapsulation. Among these, the use of synthetic polymers to form protein-polycation complexes has emerged as a promising approach, providing a protective microenvironment that can protect enzymes from harsh conditions while preserving their catalytic activity. In this context, the present study focuses on the complexation of chloroperoxidase (CPO) and versatile peroxidase (VP) within protein/polylysine-type complexes using synthetic polypeptides. This approach aims to shield enzyme thermal and oxidative stability, improve solubility and maintain structural integrity under challenging conditions [3].

Materials and methods

The materials used were poly-L-lysine (PLL) and an analogue of PLL (PNL). The enzymes were chloroperoxidase (CPO) and versatile peroxidase (VP). All solutions were prepared in phosphate buffer at pH 6. Stock solutions of PLL and PNL were made at 1 mg/mL in Milli-Q water, adjusted to pH 6, and diluted to 0.1 mg/mL. Enzymes were diluted to 0.01 mg/mL in Milli-Q water or phosphate buffer at the same pH.

Zeta potential and dynamic light scattering (DLS) were measured with a Malvern Zetasizer Nano ZS at 25 °C. Zeta potential was calculated using the Smoluchowski equation (mean ± SD, n = 3). DLS measurements at 90° scattering provided particle size and polydispersity index (PDI) (mean ± SD, n = 2). SEM was performed on a JEOL JSM-7100F. Drops were air-dried on silica wafers, sputter-coated with Au/Pd for 40 s, and imaged with a secondary electron detector. Particle sizes were analyzed using ImageJ.

Circular dichroism (CD) spectroscopy was used to characterize the secondary structures of PLL, CPO, VP, and their PLL/CPO and PLL/VP complexes, and to identify any conformational changes upon complex formation. Measurements were performed on a Jasco J-815 spectropolarimeter using a 10 mm quartz cuvette with a 2 mm path length.

Results and discussion

Titrations were performed to follow the evolution of enzyme ζ-potential as a function of the progressive addition of polypeptides to 5 mL solutions of versatile peroxidase (VP) and chloroperoxidase (CPO) at 0.01 mg/mL (**Figures 1a** and **1b**). These measurements allowed the determination of the stoichiometry of the resulting enzyme-polypeptide complexes.

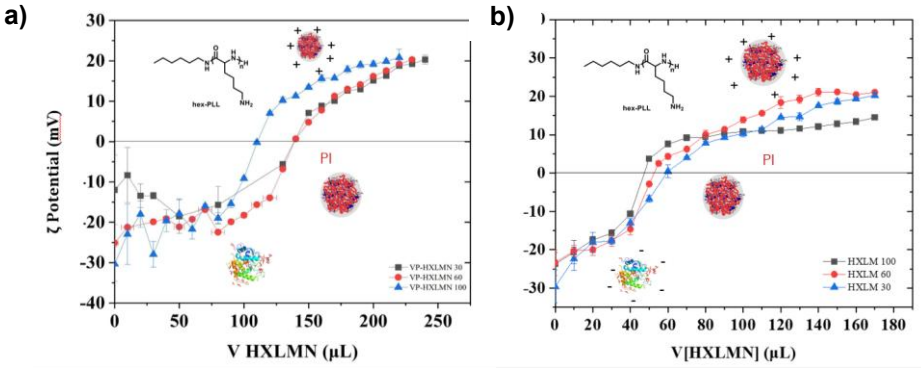

Figure 1. *Evolution of the ζ-potential as a function of the volume of polylysine added (PLL, DP = 20, 50, 100; 0.1 mg/mL, pH 6) to 5 mL solutions of (a) VP and (b) CPO in water (enzyme concentration = 0.01 mg/mL, pH 6).*

The first plateau observed in ζ-potential graph corresponds to an excess of enzyme and a low presence of polylysines, reflected by the predominance of negative charges (**Figure 1**). As the volume of polylysines increases, the ζ-potential increases until it reaches a value of 0 mV, where negative charges from the enzyme's carboxyl groups and positive charges from the protonated amino groups of the polylysines are balanced. At this stage, there is no excess of either component. The second plateau observed at the end of the titration indicates the formation of PLL/enzyme complexes with an excess of positive charges, or an excess of polypeptide. The purpose of this experiment was to determine the isoelectric point of each enzyme-polypeptide system. **Table 1** summarizes the necessary volumes of polypeptide to reach the isoelectric points obtained using 5 mL of enzyme solution at 0.01 mg/mL.

Table 1. *Volume of polypeptide required to reach the isoelectric point in 5 mL of CPO or VP solutions at 0.01 mg/mL.*

Polylysine	Enzyme	PNL_{30}	PNL_{60}	PNL_{100}	PLL_{20}	PLL_{50}	PLL_{100}
Volume (µL)	CPO	375	338	323	58.87	50.87	47.15
	VP	660	630	600	138	135	108

Using the experimental conditions summarized in **Table 1**, PLL/CPO and PLL/VP complexes were formed and monitored by Dynamic Light Scattering (DLS). Phosphate buffer or Milli-Q water at pH 6 were used as solvents. In a one-shot vortex titration approach, defined volumes of each polypeptide (0.1 mg/mL) were added to CPO or VP (0.01 mg/mL) solutions. After each addition, the mixture was vortexed and the particle size measured by DLS. The resulting complexes were then characterized by scanning electron microscopy (SEM), as shown in **Figure 2**. SEM micrographs and size distributions of PLL_{100}/CPO and PLL_{100}/VP complexes prepared at R = 0.8 (**Figure 2a** and **2b**, respectively) confirm the formation of spherical nanoparticles with sizes consistent with those obtained by DLS.

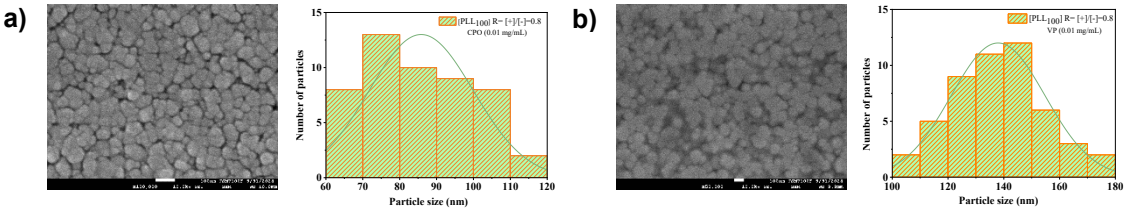

Figure 2*.- SEM micrographs and size distribution of a) PLL_{100}/CPO complexes prepared at R=0.8, and b) PLL_{100}/VP complexes prepared at R= 0.8.*

Circular dichroism (CD) experiments were performed to examine the secondary structure of the polypeptides, the CPO and VP enzymes, and within their corresponding PLL/CPO and PLL/VP complexes

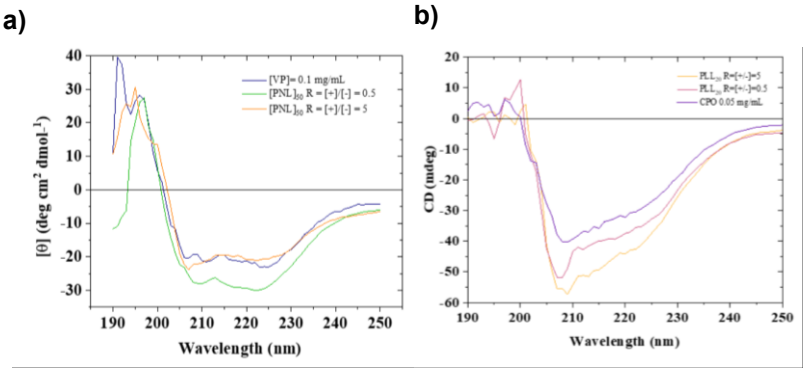

Figure 3. *Circular dichroism (CD) spectra of: a) VP and b) CPO (0.1 mg/mL) alone, and within their respective complexes formed with PLL_{100} at charge ratios of R = 0.5 and R = 5.*

CD spectra of the enzymes within the complexes formed with polypeptides were compared to those of the free enzymes to assess structural changes upon complex formation. The results indicate that the secondary structure of both enzyme complexes undergoes only minor changes upon interaction with polypeptides. Nevertheless, VP retains a predominantly α-helical conformation, while CPO maintains features consistent with a random coil structure.

The pH stability of both complexes was further evaluated by gradually lowering the pH from 6 to 4 using 0.1 M HCl. For PLL/VP complexes, particle size increased progressively from ~200 nm at pH 6 to ~400 nm at pH 4, indicating swelling of the complexes. Similarly, PLL/CPO complexes increased in size from ~300 nm and eventually formed large aggregates at lower pH, revealing an interesting pH sensitivity.

Conclusions

This study investigated the formation and characterization of enzyme-polypeptide complexes using PLL, PNL, CPO, and VP. Complex formation was monitored through ζ-potential measurements, allowing the identification of the isoelectric points for each system. The resulting complexes exhibited spherical morphology at the nanometer scale, as demonstrated by DLS, SEM and TEM analyses. Circular dichroism revealed that complexation induced minor changes in the enzymes' secondary structures, with VP maintaining a predominantly α-helical conformation and CPO keeping a random coil structure, indicating that the structural integrity of the enzymes is mainly preserved upon interaction with the polypeptides. pH stability studies showed that decreasing pH caused an increase in particle size.

References

[1] M. Ayala, E. Torres, The Royal Society of Chemistry, **2015**, 4, 309-333.

[2] S. Gao, A. Holkar, S. Srivastava, *Polymers,* **2019**, 11, 1-34.

[3] S. Kim, H.V. Sureka, A.B Kayitmazer, G. Wang, J.W Swan, B.D Olsen, Biomacromolecules, **2020**, 21, 3026-3037.

[4] E. Undiano, R. Roman, M. Miranda, M. Ayala, Natural Product Research, **2021**, 5353-5357.

Acknowledgements

Authors acknowledge the CNRS-IEA P^2NanoBio program for supporting the collaboration between Mexico and France. The University of Guadalajara, particularly the University Center of Tonalá and the University Center of Exact Sciences and Engineering, is thanked for its invaluable support and resources. P. Díaz also sincerely thanks their advisors for their guidance, encouragement, and support throughout this research project.

CROSSLINKED CHITOSAN-MALTODEXTRIN pH-SENSITIVE NANOGELS: SYNTHESIS, CHARACTERIZATION AND DOXORUBICIN ENCAPSULATION FOR CONTROLLED RELEASE

Karla Gricelda FERNÁNDEZ SOLÍS[1,2], Guillermo TORIZ[3], Pascal LOYER[4], Eduardo MENDIZABAL MIJARES[2], Julien ROSSELGONG[1], Edgar FIGUEROA OCHOA[2], Lourdes Mónica BRAVO ANAYA[1]

[1] Institut des Sciences Chimiques de Rennes, Université de Rennes, Rennes, France
[2] Universidad de Guadalajara, Departamento de Química, Universidad de Guadalajara, México
[3] Universidad de Guadalajara, Departamento de Madera, Celulosa y Papel, Zapopan, Jalisco, México.
[4] Université de Rennes, Inserm, INRAE, Institut NUMECAN, Rennes, France.
** karlag.fersol@gmail.com; lourdes-monica.anaya@univ-rennes.fr*

Abstract: Polysaccharide-based nanogels offer a wide range of chemical compositions and are of great interest due to their biodegradability, biocompatibility, non-toxicity and the ability of displaying sensitivity to stimuli such as pH and temperature. In this work, pH-responsive nanogels were synthesized using chitosan (CS) and maltodextrin (MD). These polysaccharides are classified as safe, biocompatible and readily available materials. The crosslinking reaction between chitosan and partially oxidized maltodextrins was performed through a reductive amination reaction. CS/MD nanogels exhibited diameters ranging from 63 ± 9 to 279 ± 16 nanometers, presenting a nearly spherical, cauliflower-like shape. Doxorubicin hydrochloride was encapsulated in CS/MD nanogels, reaching loading efficiencies between 55 % and 75 %. Total drug release was achieved at around 100 and 120 minutes in media adjusted at a pH of 5.5 and 7.4, respectively.

Introduction

Nanogels are commonly described as three-dimensional networks formed by physically or chemically crosslinked polymers with nanoscale dimensions. They are considered ideal carriers for delivering active ingredients to target sites thanks to their small size, chemical versatility and swelling properties []1]. Biopolymer-based nanogels offer a broad range of chemical compositions, enabling the incorporation of multiple molecules within their structure. Controlled drug release in specific cellular microenvironments can be achieved through nanogels that respond to stimuli such as pH, temperature, light or redox conditions [2]. This project aims to exploit the characteristics and advantages of chitosan and maltodextrins to develop pH-responsive nanogels for the transport and release of doxorubicin, a widely used chemotherapeutic agent. The nanogels were produced through a crosslinking reaction between CS and partially oxidized maltodextrins (ox-MD) via reductive amination [3]. The chemical modifications were monitored using IR and ^{1}H NMR spectroscopy. The resulting maltodextrin/chitosan (MD/CS) nanogels were characterized by Dynamic Light Scattering (DLS) and ζ-potential measurements to determine particle size, polydispersity index (PDI), and surface charge [3]. Their morphology was examined using Scanning Electron Microscopy (SEM). Finally, the encapsulation efficiency of the MD/CS nanogels was assessed using a series of formulations in which doxorubicin hydrochloride (DOXO) solutions of various

concentrations were incorporated. DOXO-loaded nanogels were then dialyzed in media at pH 5.5 and pH 7.4 to evaluate their drug-release capacity at different pHs.

Materials and methods

Three chitosan samples with different molecular weights (MW) and degrees of acetylation (DA) were used in this study: MW_1= 38,484 g/mol, DA_1 = 0.33; MW_2 = 86,750 g/mol, DA_2 = 0.22 and MW3 = 417,600 g/mol, DA_3 = 0.16) (Sigma Aldrich). Maltodextrin (MD-C, ref. 41, 969-9), sodium periodate, ethylene glycol and sodium cyanoborohydride ($NaBH_3CN$) were also obtained from Sigma Aldrich. A regenerated cellulose dialysis membrane with a molecular cut-off of 3.5 kDa was used throughout the nanogel purification process.

Partial oxidation of maltodextrin chains was performed before the reductive amination reaction (**Scheme 1**). Oxidation percentages ranging from 10 to 75% were achieved through oxidative cleavage of the glycol groups using sodium periodate.

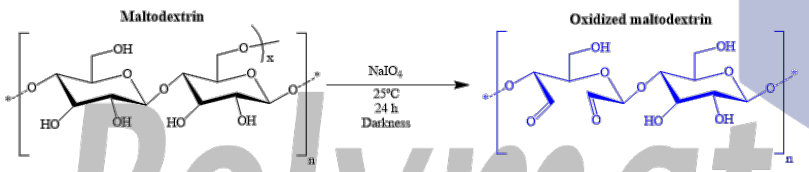

Scheme 1. Partial oxidation of maltodextrin with sodium periodate [3].

A crosslinking reaction between CS and partially oxidized MD was carried out through a reductive amination reaction (**Scheme 2**). The reactions were conducted at two pH values (3.5 and 5.5), adjusted using a sodium acetate buffer, at a constant temperature of 50 °C.

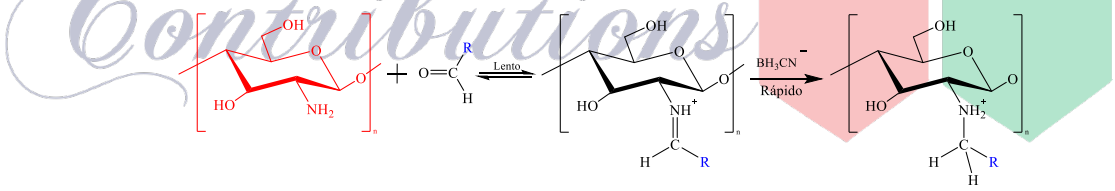

Scheme 2. Reductive amination reaction (R corresponds to the MD chain).

Several characterization techniques were used in both stages of the process, including IR spectroscopy, nuclear magnetic resonance (NMR) and dynamic light scattering (DLS). Additional morphological analyses were performed using various microscopy methods such as atomic force microscopy (AFM), scanning electron microscopy (SEM), and transmission electron microscopy (TEM). Furthermore, to evaluate the encapsulation efficiency and drug-delivery capacity, lyophilized doxorubicin (Zuclodox, Zurich Pharma) was used. The release studies were conducted through a temperature-controlled dialysis process at 37 °C under two pH conditions (pH 5.5 and pH 7.4). Doxorubicin release was quantified by UV–Vis spectroscopy. Finally, the mathematical model Kormeyer-Peppas, typically used in controlled-release systems like nanogels, was applied to determine the drug-release kinetics.

Results and discussion

The oxidation process was successfully carried out on MD, and the six resulting ox-MD samples with different oxidation percentages (10, 20, 30, 40, 50 and 75%) were characterized by IR spectroscopy and ^{1}H NMR. The appearance of a signal between 8 and 9 ppm in the ^{1}H NMR spectrum (**Figure 1a**), together with the characteristic aldehyde band at 1720 cm^{-1} in the

IR spectra (**Figure 1b**), confirmed the oxidation reactions. As expected, the intensity of these aldehyde signals increased with the degree of oxidation in both spectroscopic methods.

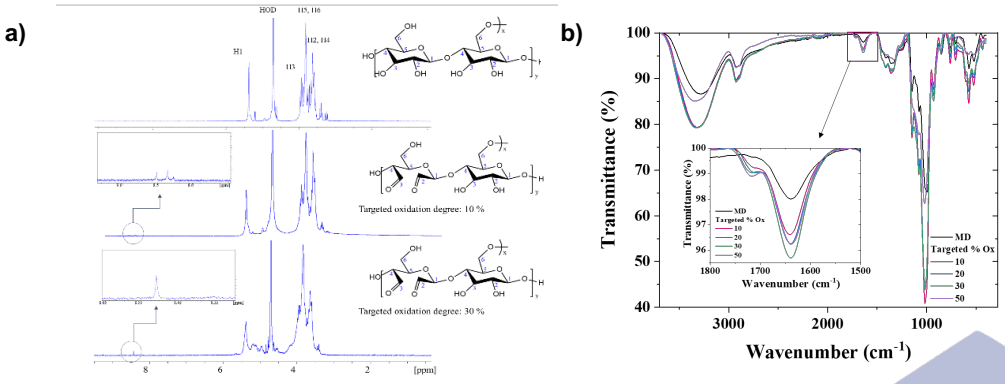

Figure 1. a) ^{1}H NMR spectra of the initial MD and the ox-MD sample with a calculated 48% oxidation in D_2O at 25 °C. b) IR spectra of the initial MD and MD samples at different oxidation percentages.

Nanogels were synthesized using three CS samples with varying MW and DA, combined with all ox-MD samples. The MD/CS nanogels exhibited the smallest particle sizes, ranging from 63 ± 9 to 279 ± 16 nm. Nanogel sizes were found to depend on the pH of the medium, the DA of chitosan, and the oxidation degree of maltodextrin. Synthesis at pH 3.5, CS concentrations in the unentangled regime, low DA and high maltodextrin oxidation resulted in smaller nanogels (**Figure 2a**). SEM analysis revealed nanogels with a slightly spherical morphology and a cauliflower-like surface structure (**Figure 2b**), consistent with the size distribution determined by DLS (**Figure 2c**).

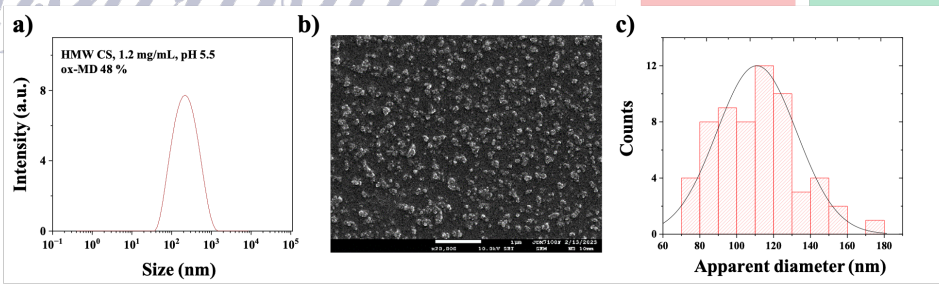

Figure 2. a) Size distribution in terms of intensity for nanogels prepared with high-MW CS at 1.2 mg/mL, pH 5.5 and 48% MD-ox; b) typical morphology observed by SEM; and c) size distribution determined with ImageJ analysis.

The encapsulation efficiency (E.E.) (**Equation 1**) was evaluated using nanogels loaded with different amounts of doxorubicin (50-1000 mg). A calibration curve was used to determine the E.E., and particle-size comparisons were made between nanogels before and after drug loading.

$$E.E. = \left[\frac{Weight\ of\ drug\ in\ NG\ solution}{Weight\ of\ drug\ added}\right] \times 100 \qquad (1)$$

Nanogels selected for doxorubicin loading displayed initial hydrodynamic diameters below 200 nm. We obtained E.E. between 55 % and 75 %, accompanied by a noticeable increase in particle size according to DLS measurements (from 149 to 762 nm). The drug-release kinetics

were analyzed using the Korsmeyer-Peppas model, commonly applied to describe drug release from polymeric systems. It is expressed as: $\frac{M_t}{M_\infty} = k_r t^n$, where *Mt/M∞* is the fraction of drug released at time *t, kr* is the release constant related to polymer-drug interactions, and *n* the diffusion exponent indicating the release mechanism [4].

Complete DOXO release occurred between 100 and 120 minutes under the tested dialysis conditions. A comparative study at pH 5.5 and pH 7.4 (**Figures 3a** and **3b**) showed faster release at pH 5.5 for both nanogels. At acidic pH, protonation of chitosan amino groups increases the positive charge, likely causing chain repulsion, swelling of the nanogel, and enhanced drug release.

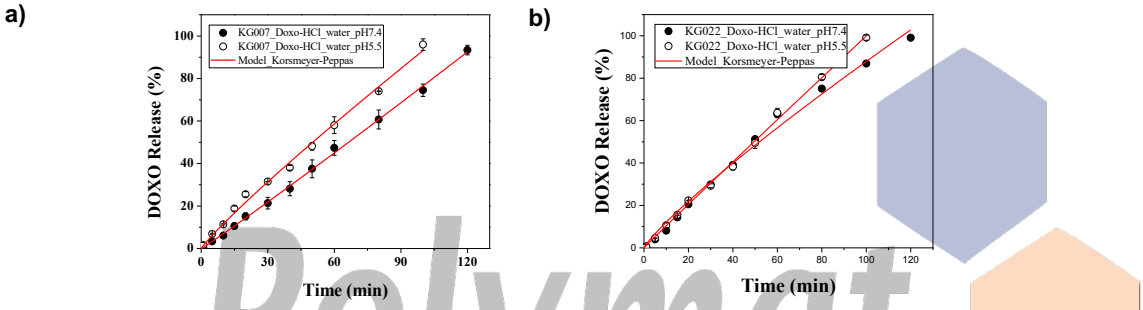

Figure 3. Kinetics of DOXO release for: a) nanogels synthesized with MMW CS, pH 5.5, 1.42 mg/mL and 10% oxidized maltodextrin b) nanogels synthesized under HMW CS, pH 5.5, 0.8 mg/mL and 48% ox-MD, both of them in media at two pH (5.5 and 7.4). Continuous lines represent the Korsmeyer-Peppas model used to fit the experimental data.

Conclusions

In this work, we synthesized pH-responsive nanogels by crosslinking chitosan and maltodextrins through a reductive amination reaction, yielding biocompatible and carriers. The nanogels exhibited nanometric dimensions and high doxorubicin encapsulation efficiency. Release studies performed at pH 5.5 and 7.4 confirmed a clear pH-dependent behavior, with faster drug release under acidic conditions relevant to endosomal environments. These results highlight the potential of chitosan-maltodextrin nanogels as robust platforms for controlled drug delivery, particularly for chemotherapeutic applications where selective release is essential.

References

[1] Rinaudo, M. Chitin and chitosan: Properties and applications, *Eur. Polym. J.*, 2010, 46, 1537–1544.

[2] Ekkelenkamp, A. E.; Elzes, M. R.; Engbersen, J. F. J.; Paulusse, J. M. J. Responsive crosslinked polymer nanogels for imaging and therapeutics delivery. J. *Mater. Chem. B*, 2018, 6, 210–235.

[3] Fernández-Solís, K. G.; Domínguez-Fonseca, E.; González Martínez, B. M.; Gutiérrez Becerra, A.; Toriz, G.; Figueroa Ochoa, E.; Mendizábal Mijares, E.; Loyer, P.; Rosselgong, J.; Bravo-Anaya, L. M. Synthesis, characterization and stability of crosslinked chitosan-maltodextrin pH-sensitive nanogels. *Int. J. Biol. Macromol.*, 2024, 274, 133277.

[4] Grassi, M.; Grassi, G. Mathematical modeling and controlled drug delivery: Matrix systems. *Current Drug Delivery*, 2005, 2(1), 97–116.

Acknowledgements

K.G. Fernández Solis wishes to acknowledge to the CONAHCYT, to all the co-authors, specially to L. M. Bravo-Anaya, to the University of Guadalajara, the University of Rennes, and to the CNRS-IEA P_2NanoBio for funding the collaboration between México and France.

Degradation of methylene blue in water using heterogenous photocatalysis with biochar

Maritza Stephania Flores Garcia[1], Alexis Eduardo Rea Flores[1], Jeannete Ramírez Aparicio[2], Carolina Godoy Alcántar[1], María Luisa García Betancourt[1]*

[1]Centro de Investigaciones Químicas, UAEM Av. Universidad 1001 Col. Chamilpa, 62209 Cuernavaca, Morelos, México; mluisa.garcia@uaem.mx.
[2]Secretaría de Ciencia, Humanidades, Tecnología e Innovación, CIICAP, UAEM, Av. Universidad 1001, Col. Chamilpa, 62209 Cuernavaca, Morelos, México.

Introduction

Methylene blue (MB) is a common dye found in industrial effluents that must be removed due to its toxicity and environmental persistence (9-10). Its release into aquatic systems can lead to harmful effects on human health, aquatic life, and overall water quality, making its removal an urgent environmental priority. Conventional treatment methods often face limitations in terms of efficiency, cost, and recovery of the treatment agents, highlighting the need for sustainable and cost-effective alternatives.

The use of carbon-based materials such as biochar offers an environmentally friendly solution for MB degradation (1–4). Biochar is a porous, carbon-rich material obtained through biomass pyrolysis, which exhibits thermal stability, surface functionality, and high adsorption capacity. Furthermore, it can act as a heterogeneous photocatalyst under sunlight, facilitating the degradation of organic contaminants without the need for harmful chemical additives (5, 8). This photocatalytic potential, combined with its adsorption properties, makes biochar a versatile material for water treatment applications. An important advantage of biochar is its production from plant residues, which makes it a sustainable, low-cost material with minimal environmental impact. In addition, its use contributes to waste valorization by converting agricultural by-products into value-added materials for environmental remediation.This study focuses on evaluating the efficiency of biochar derived from *Machaerium isadelphum* stems for the removal of MB from aqueous solutions through a photocatalytic approach. By assessing its degradation efficiency, stability, and potential for reuse, this research aims to contribute to the development of greener water treatment technologies and to provide insights into the mechanisms by which biochar interacts with sunlight to promote pollutant degradation.

Methods and materials

Biochar synthesis: 500 mg of stem of *Machaerium isadelphum* stem were placed in a quartz tube and pyrolyzed at 550 °C in a tubular oven, using a constant flow of argon of (~0.2 L min^{-1}) to ensure an inert atmosphere.

Caracterization: The sample was characterized with a stereomicroscope AmScope; thermogravimetric analysis (TGA), Fourier Transform infrarred (FTIR) and Raman spectroscopy of 532 nm.

Photocatalysis experiment: A methylene blue solution (2.5 mg in 200 mL of water) was prepared and divided into four fractions. Biochar (100 mg) was added to two of them, while 100 mg of *Machaerium isadelphum* stem were added to the other two. The samples were exposed to direct sunlight (UV index = 12). From each type of sample (one with biochar and one with stem), 5 mL of solution were withdrawn every 60 minutes over seven hours. From the other samples, 1 mL was collected at the same intervals. The MB concentrations were determined using a UV-Vis spectrophotometer.

Results and discussion

Figure 1 shows photographs of (a) the *Machaerium Isadelphum* stem before were pyrolysis (539 mg) and (b) biochar (141 mg). The mass was reduced by 74%, resulting in a material with similar morphology much lower density.

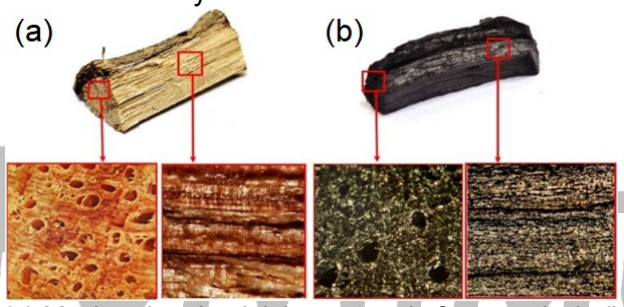

Figure 1. *(a) Machaerium Isadelphum stem before pyrolysis (b) biochar.*

Figure 2 (a) shows the thermogravimetric analysis (TGA) of the stem, which exhibits a major mass loss above 250 °C, attributed to the decomposition of plant components. In contrast, the biochar exhibits a lower mass loss, since pyrolysis at 550 °C removes most of the organic constituents. The figure 2 (b) presents the FTIR spectra: the stem spectrum shows bands assigned to carboxylic groups, aliphatic chains and C-O bonds, typical of plant matter (2,10). The biochar spectra (A and B), on the other hand, mainly exhibit carboxylic groups and C-O bonds, which are essential for methylene blue adsorption, acting as proton-donor sites (10). The duplicated spectra obtained for biochar A and B indicate that both materials share similar functional characteristics, confirming the reproducibility of the pyrolysis process.

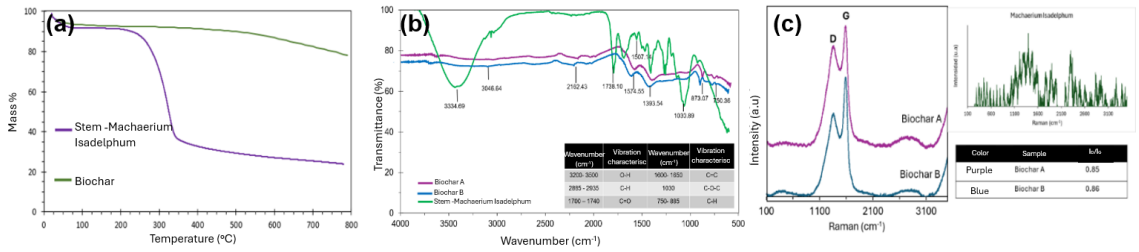

Figure 2. (a) TGA of MI stem and biochar. (b) FTIR spectres of Machaerium Isadelphum stem and biochar A and B (duplicated). (c) Raman spectres of MI stem and Biochar A and B.

The figure 2 (c) presents the Raman spectra of biochar A and B, both showing the characteristic G and D bands, with similar ID/IG ratios. The G band, associated to C-C sp^2 bonds stretching, is located between 2500-2800 cm^{-1}, while the D band indicate structural defects in sp^2 carbon lattice (turbostratic disorder) (10). Figure 3 shows that both the biochar and stem A samples follow first-order kinetic for methylene blue degradation, with high R^2 values that supporting an efficient adsorption process (~80% of decolorization). The biochar retains more effectively (90%) and the stem (80%). The low linearity suggests a dynamic equilibrium between adsorption and desorption, influenced by saturation and pollutant release (5-7). Biochar also acts as an effective photocatalyst under solar radiation, while the photolysis of MB is <20% of degradation (11). In the absence of irradiation, no significant changes were observed over the 7-hour interval, suggesting that is needed more time for a comparative reduction of MB concentration (5).

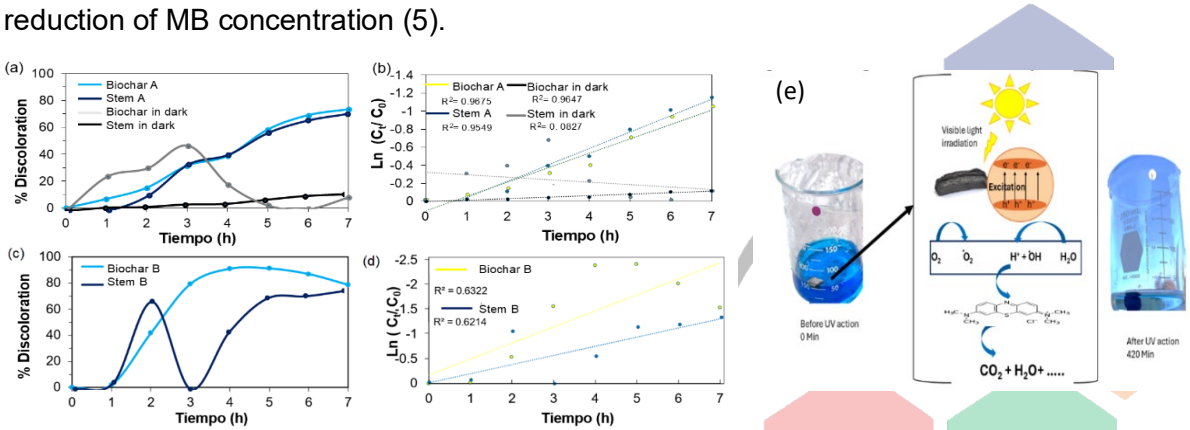

Figure 3. (a-d) Methylene Blue *degradation* kinetics *over* 7 *hours.* (e). Methylene blue degradation pathway leading to mineralization.

The degradation of methylene blue using biochar occurs under visible light irradiation, generating electron-hole pairs in the biochar. The excited electrons react with oxygen molecules, forming superoxide radicals ($\cdot O_2^-$), which attack the electrophilic regions of the dye molecules, while the holes oxidize water or hydroxyl ions, producing hydroxyl radicals (·OH). These reactive species subsequently attack π bonds and functional groups of MB, generating intermediate compounds such as sulphones and carboxylic acids, eventually leading to mineralization. As illustrated in Figure 4, these intermediates are ultimately mineralized into CO_2, H_2O, and minor inorganic ions (7).

Conclusions

Methylene blue degradation (MB) in water by applying heterogeneous photocatalysis using biochar obtained from *Machaerium Isadelphum* stem was studied in this work. The biochar, with its oxygen-containing functional groups, acts effectively as a photocatalyst, adsorbing MB, a cationic dye. The photocatalysis is heterogeneous due to between the solid (biochar) and liquid (MB solution). The desorption of methylene blue, influenced by the dynamic equilibrium between adsorption and desorption, allows a continuous degradation. The experiments highlight that solar radiation is essential for photocatalytic activity, demonstrating that biochar

exhibits high retention efficiency under direct sunlight. Compared to *Machaerium Isadelphum* stem, the biochar shows superior photocatalytic performance, stability, reusability, and recovery capacity, making it a promising material for water treatment applications.

References

1. Amin, F. R.; Huang, Y.; He, Y.; Zhang, R.; Liu, G.; Chen, C. Biochar applications and modern techniques for characterization. *Clean Technol. Environ. Policy* 2016, *18*, 1457–1473. https://doi.org/10.1007/s10098-016-1218-8.
2. Cha, J. S.; Park, S. H.; Jung, S. C.; Ryu, C.; Jeon, J.-K.; Shin, M. C.; Park, Y. K. Production and utilization of biochar: A review. *J. Ind. Eng. Chem.* 2016, *40*, 1–15. https://doi.org/10.1016/j.jiec.2016.06.002.
3. Din, M. I.; Khalid, R.; Najeeb, J.; Hussain, Z. Fundamentals and photocatalysis of methylene blue dye using various nanocatalytic assemblies—A critical review. *J. Clean. Prod.* 2021, *298*, 126567. https://doi.org/10.1016/j.jclepro.2021.126567.
4. Qiu, M.; Hu, B.; Chen, Z.; Yang, H.; Zhuang, L.; Wang, X. Challenges of organic pollutant photocatalysis by biochar-based catalysts. *Biochar* 2021, *3* (2), 117–123. https://doi.org/10.1007/s42773-021-00098-y.
5. Ramírez-Aparicio, J.; Samaniego-Benítez, J. E.; Murillo-Tovar, M. A.; Benítez-Benítez, J. L.; Muñoz-Sandoval, E.; García-Betancourt, M. L. Removal and surface photocatalytic degradation of methylene blue on carbon nanostructures. *Diam. Relat. Mater.* 2021, *119*, 108544. https://doi.org/10.1016/j.diamond.2021.108544.
6. Osorio, D. M.; Saldarriaga, H. A.; Murillo, M. A.; Vergara, J.; Ramírez, J.; Magallón, L.; García-Betancourt, M. L. Adsorption and photocatalytic degradation of methylene blue in carbon nanotubes: A review with bibliometric analysis. *Catalysts* 2023, *13* (12), 1480. 0. https://doi.org/10.3390/catal13121480
7. Sutar, P.; Otari, S. V.; Jadhav, S. V. Biochar based photocatalyst for degradation of organic aqueous waste: A review. *Chemosphere* 2022, *287*, 132200. https://doi.org/10.1016/j.chemosphere.2021.132200.
8. Hassan, W.; Farooq, U.; Ahmad, M.; Athar, M.; Khan, M. A. Potential biosorbent, *Haloxylon recurvum* plant stems, for the removal of methylene blue dye. *Arab. J. Chem.* 2017, *10* (Suppl. 2), S1512–S1522. https://doi.org/10.1016/j.arabjc.2013.05.002.
9. Khan, I.; Saeed, K.; Khan, I.; Zhang, L.; Cui, J.; Zhao, X.; Liu, H.; Zhang, P.; Zhang, W. Review on methylene blue: Uses, toxicity, and photodegradation. *Water* 2022, *14* (2), 242. https://doi.org/10.3390/w14020242.
10. Dresselhaus, M. S.; Jorio, A.; Hofmann, M.; Dresselhaus, G.; Saito, R. Perspectives on carbon nanotubes and graphene Raman spectroscopy. *Nano Lett.* 2010, *10* (3), 751–758. https://doi.org/10.1021/nl904286r.
11. Olivares-Lugo, L. I.; Rosales-González, O.; Sánchez de Jesús, F.; Martínez-Luévanos, A.; Bolarín Miró, A. M. Degradación de azul de metileno por fotólisis: efecto de variables del proceso. *Tóp. Invest. Cienc. Tierra Mater.* 2023, *10* (10), 72–76. https://doi.org/10.29057/aactm.v10i10.11226.

Acknowledgements

The authors thanks to LMA (IF-UNAM) and LANEM (CIQ-UAEM) for the Access to the installations and characterization. For the technical support to Ph. D. Cristina Zorrilla Cangas, Ph D. Perla Román Bravo, Ph. D. Diana Gabriela Vargas Pineda, Ph. D. Paola Elizabeth Sánchez Portillo and Ph D Melchor Solís Santos.

Organogels based on amino-acid vinyl hybrid polymers

Gad Fuks[1], Claire Beddok[1,2], Alicia Zimmer[1], Carole Calas Blanchard[2]

[1]Centre de Recherches Insulaires et Observatoire de l'Environnement, Université de Perpignan Via Domitia. UAR 3278 UPVD-CNRS-EPHE-PSL Labex CORAIL, France.

gad.fuks@univ-perp.fr

[2]Biocapteurs-Analyse-Environnement, Université de Perpignan Via Domitia, F-66860, Perpignan, France

Polymer gels can be derived from natural polymers or synthetic polymers [1]. Natural polymers empower gels with interesting properties such as biocompatibility, biological activity. [2] On the other hand, synthetic polymers provide them with better mechanical strength. [3] For this reason, there is a growing interest in the formation of hybrid polymers offering the possibility to combine the best of both worlds.[4] Because they have a large diversity in terms of functional groups, amino acids have found applications in various fields such as drug delivery [5], tissue engineering[6] and regenerative medicine[7]. However, peptide-based polymers often suffer from low resistance since they can be very sensitive to pH changes or enzymatic activity. In order to increase their resistance while keeping their functionalities, amino acids can be introduced in polymers avoiding the use of amide bonds through grafting of amino acids to olefin-based monomers [8].

We've been working on a facilitated synthesis of amino-acids based vinyl monomers obtained through reductive amination, their reticulated polymerization into gels and an extensive characterization of those gels by SEM, TGA, DSC, rheology and solid-state NMR.

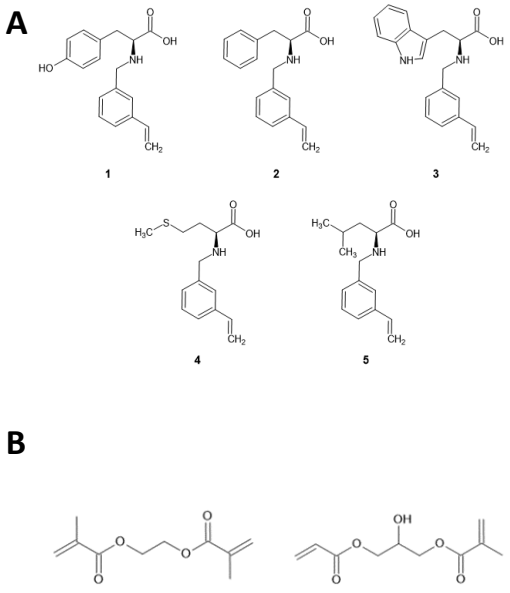

Figure 1: Figure 1. A: Structures of the vinyl monomers derived from tyrosine (1), phenylalanine (2), tryptophan (3), methionine (4) and leucine (5). B: Structures of EGDMA (left) and AHPMA (right). Figure adapted from ref 10.

The synthesis was an adaptation of the protocol described by Narita and Akiyama.[9] A reductive amination was carried out in basic conditions between 3-vinylbenzaldehyde and different amino acids. This two steps one pot synthesis was very convenient since it involved easy purification steps, without chromatography and led to amino-acids derived vinyl monomers **1** to **5** in good yields (Figure 1A). These monomers have been reacted with two kinds of crosslinking agents EGDMA and AHPMA (Figure 1B). The crosslinking process has been performed in a 2/3 mixture of aqueous 1M NaOH solution to ethanol. The initiation was achieved either photochemically or thermally by decomposition of AIBN. All the conditions tested led to solid gels which are transparent and colorless to yellowish (Figure 2). In a control experiment, EGDMA alone was put under polymerization conditions. In this case, no gel was obtained but rather a white suspension confirming the importance of the vinyl monomer in the gel formation. In a second control, the vinyl monomer was replaced by styrene, here also no gel was formed highlighting the role of the amino-acid moiety in the formation of the gel. [10]

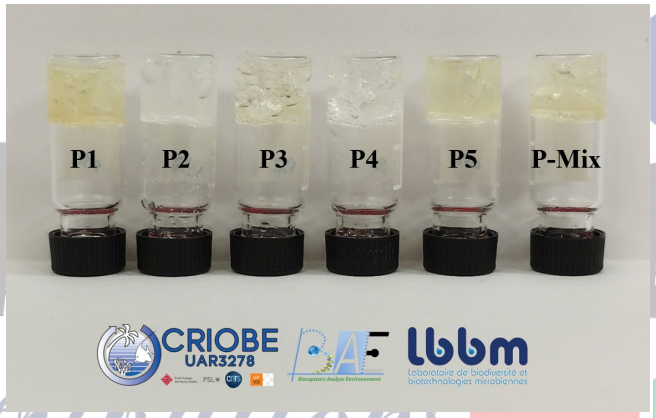

Figure 2: Picture of gels samples. From left to right, P1, P2, P3, P4, P5 and P-Mix. Reproduced from ref 10.

The obtained gels **P1** to **P5** and **Pmix** (containing a stoichiometric mixture of monomers **1** to **5**) were thoroughly characterized by a combination of complimentary techniques. Solid state NMR analysis on dried pieces of gel was used to assess the broadening of NMR signals associated with a polymerization process. It also allowed to verify the absence of unbound monomers in the gels. TGA was used to determine thermal profiles of the polymers. All the gels prepared displayed only one degradation around 420 °C indicating the robustness of the obtained material which as one of the objectives of this work. DSC experiments were used to determine the glass transition temperature of the gels. Interestingly, only one transition was observed for aged gels indicating that gels were a statistical distribution of monomer and crosslinker rather than block copolymers. The elasticity of the gels could be assessed by rheological studies. Although the behaviors were roughly the same for all gels (elastic solids with G'>G''), the values of *modulii* were influenced by the chemical nature of the monomers with G' ranging between 1000 and 10000 Pa. *In situ* rheology measurement allowed to monitor the kinetics of gel formation through photopolymerization, it revealed that after a transient phase where the system behaved like a viscous liquid, it transitioned to an elastic solid after 2h of irradiation.

This work focused on a new library of amino acid-derived gels. An easy synthetic route was developed and the crosslinking reaction was thoroughly investigated by studying the influence of various parameters such as nature of the crosslinking unit, nature of the amino acid, type of initiation. The complementarity of the characterization techniques used allowed to get insight on the nature of the gels at the molecular level as well as the macroscopic scale. The availability of such hybrid gels dervived from amino-acids can give rise to potential applications in various fields such as drug delivery or biosensing.

References

[1] Zrínyi, M. Gels, Steinkopff Heidelberg.; *Progress in Colloid and Polymer Science*; **2007**.

[2] Zhao, L.; Zhou, Y.; Zhang, J.; Liang, H.; Chen, X.; Tan, H. Natural Polymer-Based Hydrogels: From Polymer to Biomedical Applications. *Pharmaceutics* **2023**, 15 (10), 2514. https://doi.org/10.3390/pharmaceutics15102514.

[3] Barui, A. Synthetic Polymeric Gel. In *Polymeric Gels*; Elsevier, **2018**; 55–90. https://doi.org/10.1016/B978-0-08-102179-8.00003-X.

[4] Klok, H. Biological–Synthetic Hybrid Block Copolymers: Combining the Best from Two Worlds. *J. Polym. Sci. Part Polym. Chem.* **2005**, 43 (1), 1–17. https://doi.org/10.1002/pola.20527.

[5] Brisson, E. R. L.; Xiao, Z.; Connal, L. A. Amino Acid Functional Polymers: Biomimetic Polymer Design Enabling Catalysis, Chiral Materials, and Drug Delivery. *Aust. J. Chem*. **2016**, 69 (7), 705. https://doi.org/10.1071/CH16028.

[6] Klimek, K.; Ginalska, G. Proteins and Peptides as Important Modifiers of the Polymer Scaffolds for Tissue Engineering Applications—A Review. *Polymers* **2020**, 12 (4), 844. https://doi.org/10.3390/polym12040844.

[7] James, K.; Levene, H.; Parsons, J. R.; Kohn, J. Small Changes in Polymer Chemistry Have a Large effect on the Bone-implant Interface: Evaluation of a Series of Degradable Tyrosine-Derived Polycarbonates in Bone Defects. *Biomaterials* **1999,** 20, 2203-2212.

[8] Roy, S. G.; Bauri, K.; Pal, S.; De, P. Tryptophan Containing Covalently Cross-Linked Polymeric Gels with Fluorescence and PH-Induced Reversible Sol–Gel Transition Properties. *Polym. Chem*. **2014**, 5 (11), 3624. https://doi.org/10.1039/c3py01691a.

[9] Narita, M.; Akiyama, M. Syntheses and Reactions of Optically Active Polymers. I. Syntheses and Polymerizations of N-Vinylbenzyl-L-Amino Acid Derivatives. *Bulletin of Chemical Society of Japan* **1974**, 47 (1), 197–201. https://doi.org/10.1246/bcsj.47.197.

[10] Beddok, C.; Zimmer, A.; Calas Blanchard, C.; Fuks, G. Synthesis and Comprehensive Characterization of Amino Acid-derived Vinyl Monomer Gels. *ACS Omega* **2024**, 9 (45), 45053-45058. https://doi.org/10.1021/acsomega.4c05246.

Polymat Contributions

SUSTAINABLE IMPLEMENTATION OF CARBON NANOMATERIALS IN INDUSTRIAL PROCESSES: CHALLENGES, OPPORTUNITIES, RISK ASSESSMENT AND MANAGEMENT

María Luisa García Betancourt[1]

[1]*Centro de Investigaciones Químicas, UAEM Av. Universidad 1001 Col. Chamilpa, 62209 Cuernavaca, Morelos, México; mluisa.garcia@uaem.mx.*

Abstract

The sustainable integration of carbonaceous nanomaterials into industrial processes presents significant challenges and opportunities. They face challenges in production, purification, dispersion, environmental and health risks, and market acceptance [1-4]. Nanotechnology, including materials such as carbon nanotubes, graphene, and biochar, offers innovative solutions across various industrial applications due to their unique properties. However, implementing these materials requires a careful approach to address existing regulations and manage associated risks. Risk management is crucial and encompasses hazard identification, risk assessment, and the implementation of control measures to mitigate negative impacts. This work proposes a comprehensive risk assessment and management strategy to prevent and mitigate adverse effects associated with carbon nanomaterials in industrial processes, from manufacturing to the final use of nanotechnological products. Opportunities include developing new materials that could revolutionize sectors such as manufacturing and other diverse applications. Nevertheless, challenges such as scientific uncertainty and difficulties in harmonizing international regulations need to be addressed. Ongoing research and education are essential to promote the safe and effective use of carbon nanomaterials.

Introduction

Carbon nanomaterials include natural structures like graphite and diamond, synthetic such as carbon dots, carbon nanotubes, graphene, activated carbon and biochar, and incidental nanoparticles wich generate during combustioon processes (some of the resumed in Figure 1). Those nanostructures are now relevant for environmental and industrial applications because of their affinity interactions with polutants, however casues concerns by their possible toxicological and envorinmental effects.

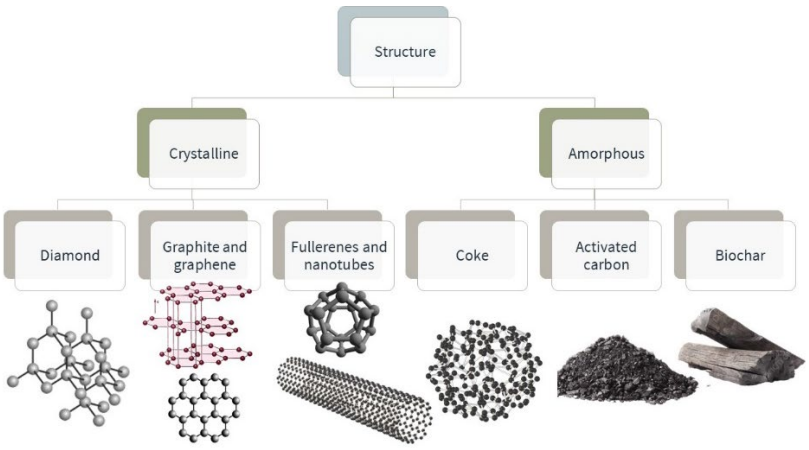

Figure 1. Carbon materials classification according their structure.

Results y Discussion

The high affinity of carbon nanomaterials with polutants is due to high surface area, surface funticonal groups and specific interactions like π-π, hidrogen bonds, etc [5]. This makes them effective in removing volatile organic compounds (VOCs), heavy metals, aromatic pollutants such as BTEX and PAHs, and even inorganic pollutants such as nitrates and phosphates [6].

In previous works, adsorption and photocatalytic degradation of methylene blue in carbon nanotubes and other carbon nanostructures have reached decoloration of 100% [7-8]. More receantly, we reported the study of adsorption and removal of carbamazepine and acetaminophen using activated carbon from sugarcane bagasse, with efficiency of ~100 % [9]. Despite such advantages and favourable results, which make them ideal for remediation and pollutant removal, their toxicological and environmental risks should not be underestimated. The shape, size, and surface reactivity of these nanostructures have been shown to influence their toxicity [10]. There is evidence of bioaccumulation, generation of reactive oxygen species (ROS), and effects on aquatic and terrestrial organisms [11]. These findings highlight the importance of developing specific regulations and risk management strategies that include environmental and health risk assessment, nanomaterial recovery and regeneration methods, and implementation of a closed-loop process that allows for their reuse.

A proposal for environmental and health risk assessment could be disclosed as follows. The first step is to identify each risk and assign the probability of occurrence against the possible impact. The correlation between probability and impact perhaps to build a risk matrix (Table 1).The intersection of probability and impact categories determines the risk level. Risks could be very low, low, medium, high, very high, or extreme. The risk level guides the actions and control measures.

Table 1. Environmental and health risk assessment matrix applied to nanotechnology process.

	Impact			
Probability	Low (1)	Moderate (2)	Severe (3)	Probability
Very High(4)	Medium 4	High 8	Very High 12	Extrem 16
High (3)	Medium 3	Medium 6	High 9	Very High 12
Medium (2)	Low 2	Medium 4	Medium 6	High 8
Medium (2)	Low 2	Medium 4	Medium 6	High 8

Table 2 presents several risk events correlated with nanotechnology processes. For example, the discharge of untreated effluents and accidental spills may cause water contamination with a high probability and moderate impact, resulting in a medium risk value in the assessment. This risk can be mitigated through continuous monitoring and the implementation of wastewater treatment systems. Nanoparticle release and gaseous emissions have a similar evaluation, which can be mitigated through the adoption of cleaner technologies and emission control systems. For severe incidents, such as nanoparticle toxicity and health risks, the

emission of nanomaterials with reactive surfaces and potential damage to biological systems requires accurate protective equipment, continuous exposure assessment, and strict handling protocols. Finally, under a catastrophic impact scenario involving nanoparticle accumulation and environmental degradation, it is of vital importance to develop prevention and remediation strategies, emphasizing the need for long-term environmental monitoring. This approach facilitates the visualization and prioritization of preventive and corrective actions, ensuring that the application of nanotechnology processes adheres to safety and sustainability principles.

Table 2. Risk management examples, their probability of occurrence and the impact, and possible control measures.

Risk	Description	Probability	Impact	Control Measures
Water Pollution	Possible contamination of water sources due to chemical spills or waste.	High	Moderate	• Implement wastewater treatment systems. • Regularly monitor water quality to detect contaminants.
Nanoparticle Toxicity	Risk of toxicity associated with the release of nanoparticles into the environment.	Medium	Severe	• Establish safe handling protocols for nanoparticles. • Implement nanoparticle emission control measures.
Health Risks	Potential adverse health effects due to exposure to nanomaterials.	High	Severe	• Conduct risk assessments to identify potential health impacts. • Implement personal protection measures for handling nanomaterials.
Air Pollution	Emission of gases and pollutants affecting air quality and public health.	High	Moderate	• Install filters and control systems at pollution sources. • Promote the use of clean technologies and renewable energy.
Environmental Degradation by Nanoparticles	Risk of negative environmental impact due to nanoparticle accumulation in the environment.	Medium	Catastrophic	• Implement environmental monitoring measures to detect nanoparticle accumulation. • Develop remediation strategies in case of nanoparticle contamination.

Conclusions

Carbon nanomaterials offer promising solutions for remediation and industrial applications thanks to their tunable properties and high surface area. However, large-scale implementation faces challenges such as reproducibility, scalability, and manufacturing cost, as well as concerns about toxicity to human health and the environment. Therefore, it is crucial to promote regulatory systems and standardized methodologies for risk assessment. Risk management assessed through a probability; impact matrix and continuous monitoring provides a structural basis for the identification, evaluation, and mitigation of adverse effects throughout the nanomaterial's life cycle. Additionally, promoting eco-friendly synthesis routes, safe design strategies, and circular economy principles contributes to minimizing the environmental impact while maintaining technological efficiency. In summary, ensuring that the synthesis and application of nanomaterials adhere to sustainability and safety principles supports responsible and long-term implementation in environmental and industrial fields.

References

[1] Zhang, Q.; Huang, J.; Qian, W.; Zhang, Y.; Wei, F. The road for nanomaterials industry: a review of carbon nanotube production, post-treatment, and bulk applications for composites and energy storage. *Small* **2013**, 9(8), 1237-65.
[2] Goswami, A.; Trivedi, D.; Jadhav, N.; Pinjari, D. Sustainable and green synthesis of carbon nanomaterials: A review. *J. Environ. Chem. Eng.* **2021**, 9(5), 106118.
[3] Gopinath, K.; Vo, D.; Prakash, D.; Joseph, A.; Viswanathan, S.; Arun, J. (). Environmental applications of carbon-based materials: a review. *Environ. Chem. Lett*. **2020**, 19, 557-582.
[4] Jha, R., Singh, A., Sharma, P., & Fuloria, N. Smart carbon nanotubes for drug delivery system: A comprehensive study. *J. Drug Deliv. Sci. Technol.* **2020**, 58, 101811.
[5] Rezania, S.; Darajeh, N.; Rupani, P. F.; Mojiri, A.; Kamyab, H.; Taghavijeloudar, M. Recent Advances in the Adsorption of Different Pollutants from Wastewater Using Carbon-Based and Metal-Oxide Nanoparticles. *Appl. Sci.* **2024**, *14*, 11492.
[6] Asghar, N.; Hussain, A.; Nguyen, D. A.; Ali, S.; Hussain, I.; Junejo, A.; et al. Advancement in Nanomaterials for Environmental Pollutants Remediation: A Systematic Review on Bibliometrics Analysis, Material Types, Synthesis Pathways, and Related Mechanisms. *J. Nanobiotechnol.* **2024**, *22*, 26.
[7] Ramírez-Aparicio, J.; Samaniego-Benítez, J. E.; Murillo-Tovar, M. A.; Benítez-Benítez, J. L.; Muñoz-Sandoval, E.; García-Betancourt, M. L. Removal and surface photocatalytic degradation of methylene blue on carbon nanostructures. *Diamond Relat. Mater.* **2021**, *119*, 108544.
[8] Osorio-Aguilar, D. M.; Saldarriaga-Noreña, H. A.; … García-Betancourt, M. L. Adsorption and photocatalytic degradation of methylene blue in carbon nanotubes: a review with bibliometric analysis. *Catalysts* **2023**, *13*(12), 1480.
[9] Márquez, R. A. L.; Saldarriaga-Noreña, H.; García-Betancourt, M. L.; Rodríguez-Solís, A.; Morera-Boado, C.; Albañil-Sánchez, L.; Murillo-Tovar, M. A. Adsorptive removal of carbamazepine and paracetamol using sugarcane bagasse-derived activated carbon: Experimental optimization and mechanistic insights. *Sep. Purif. Technol.* **2025**, 135377.
[10] Fito López, C.; et al. Exposure Assessment and Risk Characterization of Carbon-Based Nanomaterials at Different Production Scales. *Sustainability* **2023**, *15*(16), 12544.
[11] Tao Jiang; et al. Comparative and Mechanistic Toxicity Assessment of Structure-Dependent Toxicity of Carbon-Based Nanomaterials. *J. Hazard. Mater.* **2021**, 418, 126282.

Polymat Contributions

Wet atmospheric deposition fluxes and atmospheric corrosion at two urban sites and one rural site in México

R. García[1*], A. Carrillo-Chávez[2], R. M. Cerón[3], J. G. Cerón[3]

[1]Instituto de Ciencias de la Atmósfera y Cambio Climático, Universidad Nacional Autónoma de México, C.P. 04510, México. *gmrocio@atmosfera.unam
[2]Instituto de Geociencias, Universidad Nacional Autónoma de México, Campus Juriquilla. Blvd. Juriquilla 3001, Juriquilla, Querétaro, C.P. 76230, México.
[3]Facultad de Química Universidad Autónoma del Carmen, Ciudad del Carmen, C.P.24180, Campeche.

Atmospheric corrosion is the deterioration of a material due to electrochemical reactions of its surface with the constituents of the surrounding atmosphere [1, 2]. In the present investigation, sampling campaigns were carried during the 2020-2024 rainy season. Sampling was on the the Institute of Geosciences-UNAM, Juriquilla Campus (IGeo-Jur), a site belonging to the University Network of Atmospheric Observatories of the UNAM (RUOA), the second site on the roof of a house, located in the center of Santa Rosa Jáuregui, Querétaro (SRJ-Qro). The objective of this work was to determine and evaluate the average deposition rate of SO_4^{2-}, NO_3^-, Na^+, Cl^- and NH_4^+ and the physicochemical properties of the atmospheric deposit. The results obtained from the deposition obtained for IGeo-Jur in the sampled events was 90.69 mg/m^2 and the estimated for the days without event sampling was 954.39 mg/m^2 and for SRJ-Qro the deposition observed in the sampled events was 768.83 mg/m^2 and the estimated value for days without event sampling was 1122.59 mg/m^2. The figure 1A, present the correlation of H^+ with sulfates (SO_4^{2-}) r=0.5527, r^2=0.3054 ($p<0.05$) for IGeo-Jur, which is due to the fact that the acidity of the samples is mainly given by H_2SO_4, and therefore, the higher the concentration of sulfates, the higher the acidity, the lower the pH and the higher the H^+. The figure 1B, show SRJ-Qro the correlation of H^+ with sulfates (SO_4^{2-},) is observed r= 0.6118, r^2=0.3743 ($p<0.05$), which is due to the fact that the acidity of the samples is mainly given by H_2SO_4 and therefore, the higher the concentration of SO_4^{2-}.

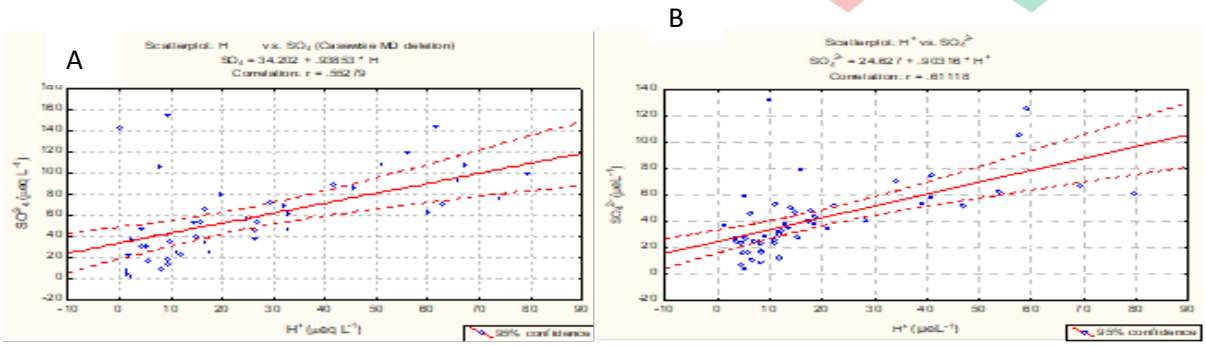

Figure 1A and 1B. Correlation of H^+ with sulfates (SO_4^{2-}) for IGeo-Jur and for SRJ-Qro.

References

[1] Lohmann, U., Lüönd, F., y Mahrt, F. (2016). An introduction to clouds: from the microscale to climate. Cambridge University Press. https://doi.org/10.1017/CBO9781139087513

[2] Zeng, J., Yue, F. J., Li, S. L., Wang, Z. J., Wu, Q., Qin, C. Q., y Yan, Z. L. (2020). Determining rainwater chemistry to reveal alkaline rain trend in Southwest China: evidence from a frequent-rainy karst area with extensive agricultural production. Environmental Pollution, 266, 115166.

OPTIMIZATION OF MILLING TIME FOR NANOBIOCHAR PRODUCTION: DETAILED CHARACTERIZATION AND EVALUATION OF FUNCTIONAL PROPERTIES

Aneyda Yadira Popoca Bustos[1], Melchor Solis Santos[2], María Luisa García Betancourt[2]*

[1]Facultad de Farmacia, UAEM. Av. Universidad 1001 Col. Chamilpa, 62209 Cuernavaca, Morelos, México
*[2]Centro de Investigaciones Químicas, UAEM. Av. Universidad 1001 Col. Chamilpa, 62209 Cuernavaca, Morelos, México; *mluisa.garcia@uaem.mx.*

Abstract

Nanobiochar (NB), a porous carbon material derived from biomass, has significant potential in environmental remediation, soil improvement, pollutant adsorption, and energy storage. By integrating biochar technology with nanotechnology, NB exhibits enhanced pollutant adsorption and soil mobility. This study focuses on optimizing the milling time for NB production and analyzing its impact on structural and functional properties. The methodology involved the pyrolysis of Machaerium isadelphum leaves to produce biochar, which was subsequently milled for different durations (10, 20, and 30 minutes) using a ball mill. The resulting nanobiochars were characterized using techniques such as TGA, FTIR, and Raman spectroscopy, along with dispersibility and fluorescence evaluations in various solvents.
The results indicate that increased milling time significantly improves the dispersibility and functionalization of NB, particularly in aqueous environments, thereby enhancing its potential for catalytic and environmental applications. In addition, the shifts observed in the absorption and emission bands suggest that the particle size of NB in aqueous solution, at different concentrations, ranges approximately from 40 to 60 nm. Notably, the NB milled for 20 minutes demonstrated superior surface functionalization, as evidenced by FTIR and Raman analyses. This study concludes that optimizing the milling time is crucial for producing high-quality NB, emphasizing its improved adsorption capabilities and potential for broader application in sustainable technologies.

Introduction

Nanobiochar derived from biomass is a porous carbon material with potential applications in environmental remediation, soil enhancement, contaminant adsorption, and energy storage. Used in water remediation and as an additive in various products, nanobiochar offers sustainable solutions to current challenges. Combining biochar technology with nanotechnology can revolutionize research by producing nanobiochar with excellent contaminant adsorption capacity and soil mobility [1–2]. This study aims to optimize the milling time for nanobiochar production, specifically analyzing how milling duration influences its structural and functional properties. The objective is to establish optimal parameters that maximize efficiency and quality through characterization and evaluation.

Materials and methods

Approximately 3.828 g of dried *Machaerium isadelphum* (*MI*) leaves were pyrolyzed at 340 °C for 10 min in a quartz tube inside a Thermo Scientific Lindberg Blue M tubular furnace. A constant argon flow of ~0.2 L/min was maintained to ensure an inert atmosphere. Milling was

carried out in an Anton Paar BM500 steel ball mill at 20 Hz for 10, 20, and 30 min. The five samples were designated as leaves, biochar, NB10, NB20, and NB30. Dispersibility was evaluated after 5 min of agitation in different media: deionized water, glycine solution, acetone, and ethanol. Characterization techniques included thermogravimetric analysis (TGA), Fourier-transform infrared spectroscopy (FTIR), Raman spectroscopy to evaluate the properties.

Results and discussion

Figure 1 shows the TGA analysis, revealing mass loss in the samples due to moisture evaporation at approximately 100 °C. The leaves exhibit an additional weight loss above 250 °C, associated with the degradation of cellulose, hemicellulose, and lignin (above 600 °C) [4]. The biochar and nanobiochar samples (NB10, NB20, NB30) demonstrate higher thermal stability, retaining approximately 50% of their mass at 800 °C.

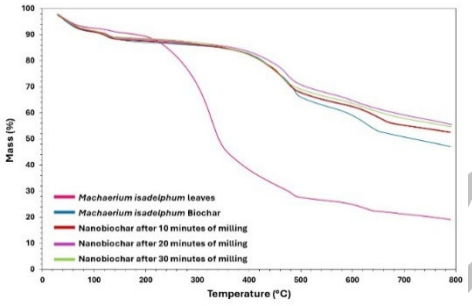

Figure 1. Thermogravimetric Analysis (TGA) of *MI* stem, biochar, NB10, NB20 and NB30.

Figure 2(A) displays the FTIR spectra of the leaves, showing carboxylic and C–O groups [4]. The biochar and NB samples exhibit O–H, carboxylic, C–O, C–C, and C=C groups [3]. NB20 (purple line) stands out with higher intensities, indicating greater surface functionalization [4]. Figure 2(B) presents the Raman spectra, highlighting the D (~1300 cm^{-1}) and G (~1600 cm^{-1}) bands. The D band indicates the presence of defects or non-sp^2 carbon, while the G band corresponds to sp^2 carbon [5]. The similar I_D/I_G ratio suggests that milling did not significantly modify the biochar structure.

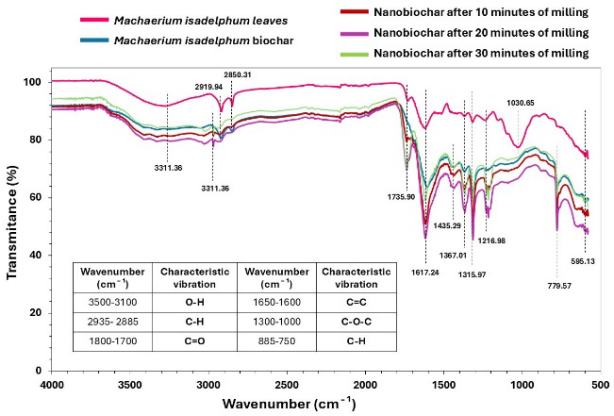

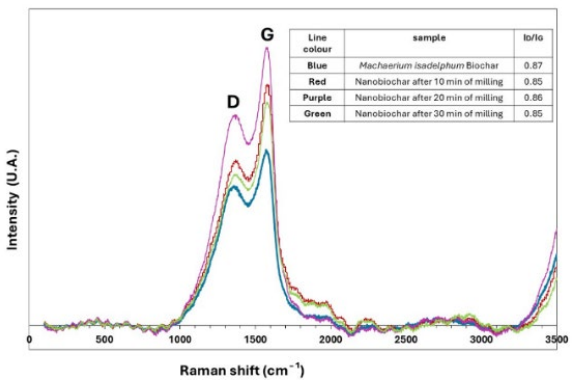

Figure 2. (A) FTIR spectra and (B) Raman spectra of *Machaerium Isadelphum* of stem, biochar, NB10, NB20 and NB30.

Figure 3 shows the dispersibility of NB in aqueous media. The dispersed NB in water is clearly observed; after one-week, small particles remain suspended, indicating colloidal stability, high dispersibility, and effectiveness [6].

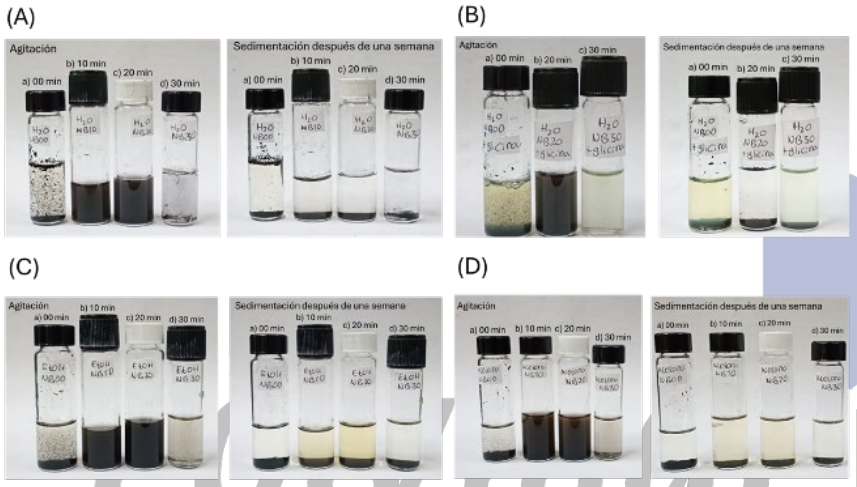

Figure 3. (A) Samples with water, (B) Samples with water and glycine, (C) Samples with ethanol, and (D) Samples with acetone.

Figure 4 demonstrates that nanobiochar emits fluorescence, attributed to aromatic structures and oxygenated functional groups [7]. The presence of glycine further intensifies fluorescence, particularly in NB30. Figure 5 shows the absorption and fluorescence spectra of NB in aqueous solution. The observed redshift in both absorption and emission bands suggests particle sizes ranging from 40 to 60 nm. Luminescence intensity varied with concentration, displaying a broad emission band, as expected, due to the sample's purity.

Figure 4. Fluorescence test.

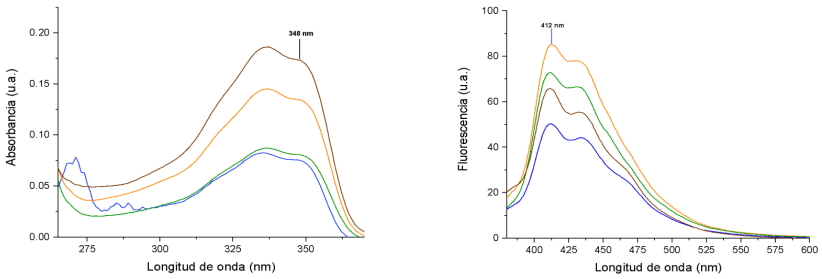

Figure 5. Absorption and fluorescence spectra of NB.

Conclusions

This work highlights the importance of optimizing milling time to obtain nanobiochar with improved physicochemical properties. Extended milling time improves dispersibility in aqueous media, which also exhibits fluorescence, confirming the functionalization of NB surfaces. NB20 for 20 min of milling demonstrated best structural integrity and functionalization. This method avoids the use of acids or hazardous dissolvents, resulting in a sustainable synthesis method. Additionally, controlled milling is an alternative that influencing optical and adsorption properties, supporting applications in sustainable technologies.

Acknowledgements

The authors thank LMA (IF-UNAM) and LANEM (CIQ-UAEM) for access to facilities and characterization. They also express their gratitude for technical support to Cristina Zorrilla Cangas, Perla Román Bravo, Diana Gabriela Vargas Pineda, and Paola Sánchez Portillo.

References

[1] Chausali, N.; Saxena, J.; Prasad, R. Nanobiochar and Biochar-Based Nanocomposites: Advances and Applications. *J. Agric. Food Res.* **2021**, *5*, 100191.
[2] Chaubey, A. K.; et al. Definitive Review of Nanobiochar. *ACS Omega* **2024**, *9*(11), 12331–12379.
[3] Ng, L. Y. F.; Ariffin, H.; Yasim-Anuar, T. A. T.; Farid, M. A. A.; Hassan, M. A. High-Energy Ball Milling for High Productivity of Nanobiochar from Oil Palm Biomass. *Nanomaterials* **2022**, *12*(18), 3251.
[4] Khan, H. A.; et al. A Performance Evaluation Study of Nano-Biochar as a Potential Slow-Release Nano-Fertilizer from Wheat Straw Residue for Sustainable Agriculture. *Chemosphere* **2021**, *285*, 131382.
[5] Dresselhaus, M. S.; Jorio, A.; Filho, A. G. S.; Saito, R. Defect Characterization in Graphene and Carbon Nanotubes Using Raman Spectroscopy. *Philos. Trans. R. Soc. A Math. Phys. Eng. Sci.* **2010**, *368*(1932), 5355–5377.
[6] Jia, Q.; Chen, F.; Li, H.; Zhang, L. Effect of Particle Size on Dispersion Velocity of Inert Particles under Shock Wave. *Proc. 2023 5th Int. Acad. Exch. Conf. Sci. Technol. Innov. (IAECST)* **2023**, 819–823.
[7] Bhandari, G.; Gangola, S.; Dhasmana, A.; Rajput, V.; Gupta, S.; Malik, S.; Slama, P. Nano-Biochar: Recent Progress, Challenges, and Opportunities for Sustainable Environmental Remediation. *Front. Microbiol.* **2023**, *14*, 1214870.

Polymat Contributions

Composite Hydrogels Based on Chitosan and Poly(vinyl alcohol) for Efficient Removal of Azo Dyes from Water

I.M. Garnica-Palafox[1,2,*], F.M. Sánchez-Arévalo[1], M. Bizarro[1], A.M. Velázquez-Benítez[2], N. Qureshi[2]

[1] *Instituto de Investigaciones en Materiales, UNAM, Cd. Universitaria, CDMX 04510, México.*
[2] *Instituto de Ciencias Aplicadas y Tecnología, UNAM, Cd. Universitaria, CDMX 04510, México.*
**marisol.garnica@materiales.unam.mx*

Abstract

We evaluated the use of hybrid hydrogel membranes based on chitosan (CS) and poly(vinyl alcohol) (PVA), chemically crosslinked with genipin (GEN) and filled with multi-walled carbon nanotubes (MWCNTs), as dye adsorbents. Methyl orange (MO) and acid blue 113 (AB113) dye solutions were used as model pollutants. The hydrogels' dye removal efficiency was assessed under both acid and basic pH conditions. The CS/PVA/GEN and CS/PVA/GEN/MWCNTs hydrogels exhibited adsorption capacities (q_t) of up to 0.65 and 0.41 mg/g (88% and 60% removal efficiency) for AB113, and 0.35 and 0.36 mg/g (97% and 93% removal efficiency) for MO. Experimental data were successfully fitted to a non-linear pseudo-first-order kinetic model, suggesting that physisorption processes are responsible for capturing the dye. The refractive index of the hydrogels at THz frequencies decreased due to the presence of dye molecules in their polymeric network. FT-IR spectroscopy demonstrated that the amino (-NH_2) and hydroxyl (-OH) groups are primarily involved in adsorption.

Introduction

Azo dyes used in the textile, paper, pharmaceutical, cosmetic, and food industries are recognized as significant environmental contaminants in waterways [1]. These synthetic organic dyes modify vital conditions in aquatic environments, adversely affecting aquatic organisms and human health. Numerous studies have demonstrated that adsorption is an effective method for removing these persistent pollutants due to its high efficiency, cost-effectiveness, and operational simplicity [2-4]. Among the materials explored for water remediation, hydrogels based on chitosan (CS) have attracted considerable attention. CS is an abundant natural polysaccharide derived from chitin and is characterized by a high content of amino (-NH_2) and hydroxyl (-OH) groups that enable strong interactions with a wide range of water pollutants. However, its practical applications are limited by its inherently poor mechanical properties. For this reason, CS has been combined with natural or synthetic polymers and crosslinking reagents to enhance its mechanical strength and overall structural stability [5, 6].

In this work, we propose the development of composite hydrogels prepared by blending CS with poly(vinyl alcohol) (PVA), a biocompatible and hydrophilic synthetic polymer, and using genipin (GEN) as a natural and environmentally benign crosslinking reagent. The incorporation of PVA into the CS network is expected to provide additional hydroxyl groups, thereby enhancing both the swelling capacity and the affinity toward organic dyes. GEN crosslinking will further improve the mechanical and structural stability of the CS/PVA hydrogels in aqueous media. In addition, the incorporation of multi-walled carbon nanotubes (MWCNTs) is anticipated to increase their dye removal capacity. We evaluate the stability, adsorption efficiency, feasibility, and adsorption kinetics of CS/PVA/GEN and CS/PVA/GEN/MWCNTs hybrid hydrogels using methyl orange (MO) and acid blue 113 (AB113) as representative azo dye pollutants.

Materials and methods

CS powder (75–85% deacetylation, medium molecular weight), PVA (99% hydrolysis, 89,000–98,000 g/mol) and GEN (≥98% purity) was used to prepare the hydrogel membranes, using

deionized water and HPLC-grade acetic acid as solvents. For the nanocomposites, MWCNTs with 6–9 nm diameter and 5 μm length were incorporated as fillers.

Hydrogels' Synthesis

To produce thin membranes, crosslinked CS/PVA/GEN hydrogels and CS/PVA/GEN/MWCNTs nanocomposites were prepared by a solvent casting method, following the procedure described in our previous works [3, 5].

Dye sorption experiments

To evaluate the dye sorption performance of the hydrogels, batch sorption experiments were conducted using aqueous solutions of the azo dyes acid blue 113 (AB113) and methyl orange (MO), selected as models of anionic dyes found in textile effluents. Samples of CS/PVA/GEN and CS/PVA/GEN/MWCNTs hydrogel films (3.85 cm^2) were individually immersed in 10 mL of AB113 or MO solutions with an initial concentration of 10^{-5} M. The pH of the dye salutions was adjusted to 6.2±0.2 or 10.0±0.4 using NaOH (0.05 M) to assess the effect of initial pH on adsorption performance. Aliquots of the dye solutions were collected at determine time intervals, and the absorbance spectra were recorded using a Shimadzu 1800UV–Vis spectrophotometer. Dye concentrations were obtained from calibration curves at the maximum absorbance wavelength (566 nm for AB113 and 464 nm for MO). The adsorption capacity $q_t(mg/g)$ was calculated using Eq. 1:

$$q_t = {(C_0 - C_t)\,V}/{m} \quad (1)$$

where C_0 and C_t (mg/L) represent the initial time and time-dependent dye concentrations, respectively; V(L) is the solution volume, and m (g) refers to the weight of the hydrogel sample. To elucidate the adsorption mechanism, the kinetic data were fitted using the pseudo-first-order (PFO, Eq.2) and pseudo-second-order (PSO, Eq. 3) non-linear models.

$$q_t = q_{e,T}\,(1 - e^{-k_1 t}) \quad (2)$$

$$q_t = k_2\,q_{e,T}^2\,t/(1 + k_2\,q_{e,T}\,t) \quad (3)$$

Here, $q_{e,T}$ (mg/g) is the theoretical equilibrium adsorption capacity, k_1 (min^{-1}) is the PFO rate constant, and k_2 (g/(mg min)) is the PSO rate constant.

Fourier Transform Infrared Spectroscopy (FT-IR)

FT-IR spectroscopy was conducted on dry hydrogel samples using attenuated total reflectance (ATR) with a diamond crystal module (Smart-iTX ATR, Nicolet iS50, Thermo Scientific Inc.). Spectra were collected in the 4000 to 500cm^{-1} range with a resolution of 0.5 cm^{-1}, acquiring 32 scans per sample.

Terahertz Spectroscopy

Terahertz time-domain spectroscopy (THz-TDS) in transmission mode was used to detect the presence of AB113 dye within the polymeric networks by monitoring changes in their THz complex refractive index. Time domain signal were adquired over a total time window of 136.5 ps, with a temporal resolution of 33.33 fs. The effective bandwidth of the system was 0.3-1.5 THz range. The real refractive index (n) of the samples was calculated using Eq. 4, as detailed in [7].

$$n = \Delta\phi \frac{c}{2\pi\nu d} + 1 \quad (4)$$

where, $\Delta\phi$ is the phase difference between reference and sample signals ($\Delta\phi$ = ϕref −ϕsample), c the speed of light in vacuum, ν the THz frequency, and d the sample thickness.

Results and discussion

Dye Adsorption Capacity and Kinetic models

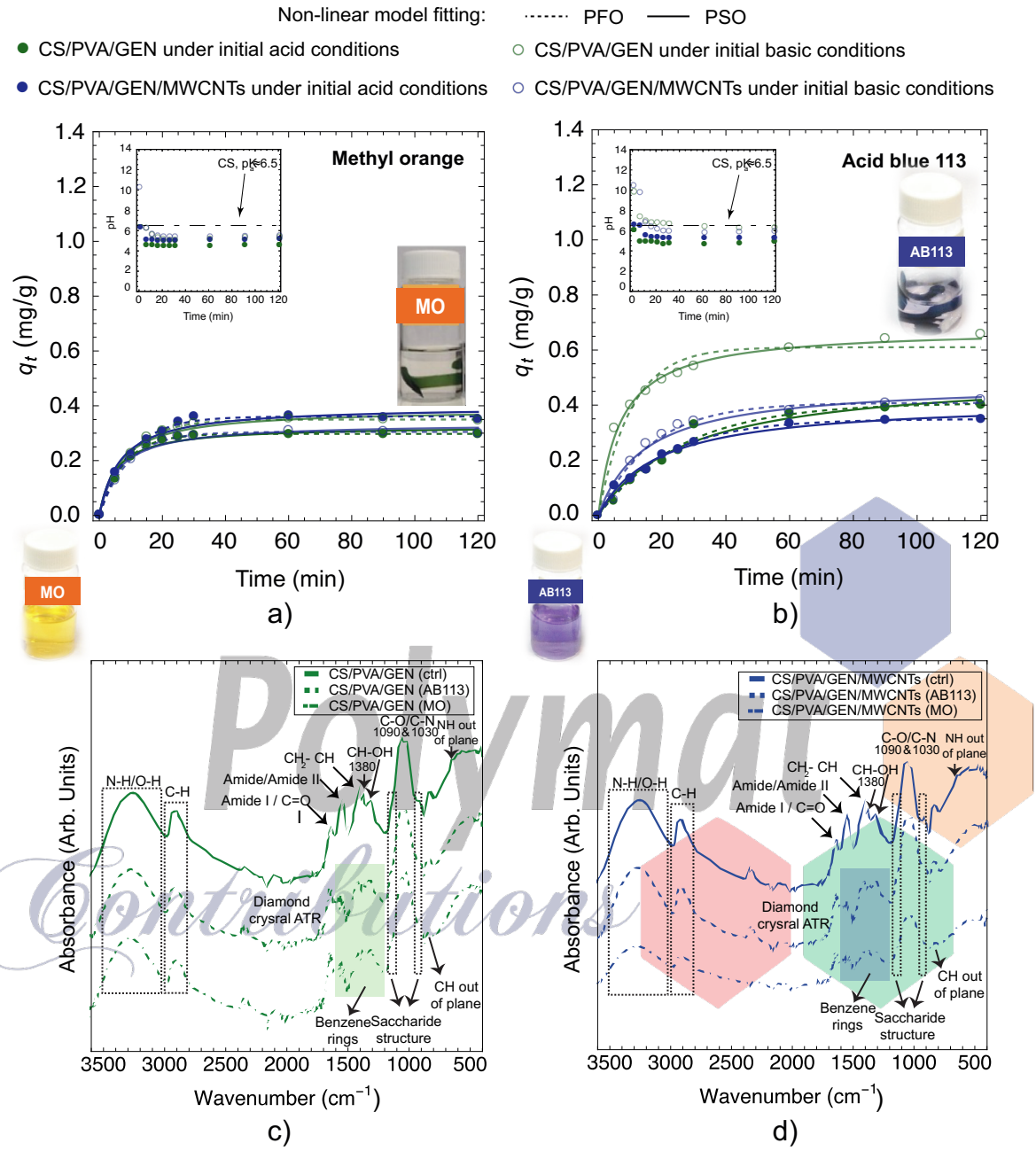

Figure 1. Adsorption kinetics of a) methyl orange (MO) and b) acid blue 113 (AB113) onto CS/PVA/GEN and CS/PVA/GEN/MWCNTs hybrid hydrogels. FT-IR spectra of hydrogels before and after dye adsorption: c) CS/PVA/GEN interacting with azo dyes, and d) CS/PVA/GEN/MWCNTs interacting with azo dyes.

The analysis of adsorption kinetics is fundamental for understanding both the efficiency and the underlying mechanisms of the adsorption process. Figures 1a) and 1b) show the effects of contact time and initial pH on the adsorption of MO and AB113 by CS/PVA/GEN and CS/PVA/GEN/MWCNTs hydrogels. In both systems, adsorption proceeds in three stages: an initial rapid uptake due to the high availability of active sites (-OH, $-NH_2$, or $-NH_3^+$ depending on pH), followed by a gradual decrease in adsorption rate as these sites become occupied, and finally a near-equilibrium state when steric hindrance or site saturation limits further dye uptake.

For MO (Fig. 1a)), adsorption capacity stabilizes after 60 min, reaching $q_t \approx 0.25–0.35$ mg/g at 120 min for both hydrogels. No significant differences were observed between acidic and basic

initial conditions, as the basic solutions spontaneously acidified (pH < 6.5) within the first 5–10 min, favoring electrostatic interactions regardless of the initial pH. In contrast, AB113 adsorption (Fig. 1b)) remained strongly dependent on pH. Under basic conditions, CS/PVA/GEN hydrogels exhibited higher adsorption throughout the experiment, as the solution remained alkaline for up to 60 min (pH > pKa of CS). In this state, the hydrogel surface is neutral and adsorption likely proceeds through hydrogen bonding, van der Waals forces, or π–π interactions via the free hydroxyl groups of CS and PVA. The nanocomposite hydrogels showed lower adsorption due to partial crystallization of PVA around MWCNTs, reducing the availability of polar groups. After 120 min, q_t values for AB113 were 0.40 mg/g (acid) and 0.66 mg/g (basic) for CS/PVA/GEN, and 0.35 mg/g (acid) and 0.42 mg/g (basic) for CS/PVA/GEN/MWCNTs. The slower adsorption of AB113, which did not reach equilibrium within 120 min, is attributed to its larger molecular size compared with MO.

Kinetic analysis using the pseudo-first-order (PFO) and pseudo-second-order (PSO) models (Fig. 1a–b) showed that the non-linear PFO model provided the best fit for both dyes. The high correlation coefficients ($R^2 \approx$ 0.994–1) indicate that physisorption is the rate-controlling mechanism.

FT-IR Spectroscopy

To verify the interaction of MO and AB113 with the hybrid hydrogels, FT-IR spectra were obtained before and after adsorption. Figures 1a) and 1b) show the spectra of the membranes prior to dye exposure (solid lines) and after adsorption (dashed lines). The hydrogels exhibited the characteristic bands of their functional groups [5]. After contact with the dye solutions, slight but consistent spectral changes appeared. Specifically, the bands associated with chitosan amine groups (3500–3000 cm^{-1}, 1600–1500 cm^{-1}, 640 cm^{-1}, 1090 cm^{-1}, 1030 cm^{-1}) and with PVA hydroxyl groups (3500–3000 cm^{-1}, 1320 cm^{-1}, 1090 cm^{-1}, 1030 cm^{-1}) showed reduced intensity. This behavior is consistent with adsorption driven by electrostatic attraction between dye sulfonate groups ($–SO_3^-$) and protonated chitosan amines ($–NH_3^+$) at pH<6.5, as well as by hydrogen bonding, Yoshida-type interactions, and n–π stacking between PVA/CS hydroxyl groups and dye molecules in either acidic or alkaline media.

After adsorption, additional bands corresponding to aromatic structures were detected between 1700–1200 cm^{-1}: benzene ring signals for MO and benzene/naphthalene signatures for AB113 (highlighted in Figs. 1c) and 1d)). These bands confirm the presence of adsorbed dye molecules on the hydrogel surface. Since no new FT-IR bands appeared after adsorption, and only intensity variations were observed, the process is consistent with physisorption rather than chemisorption.

THz refractive index

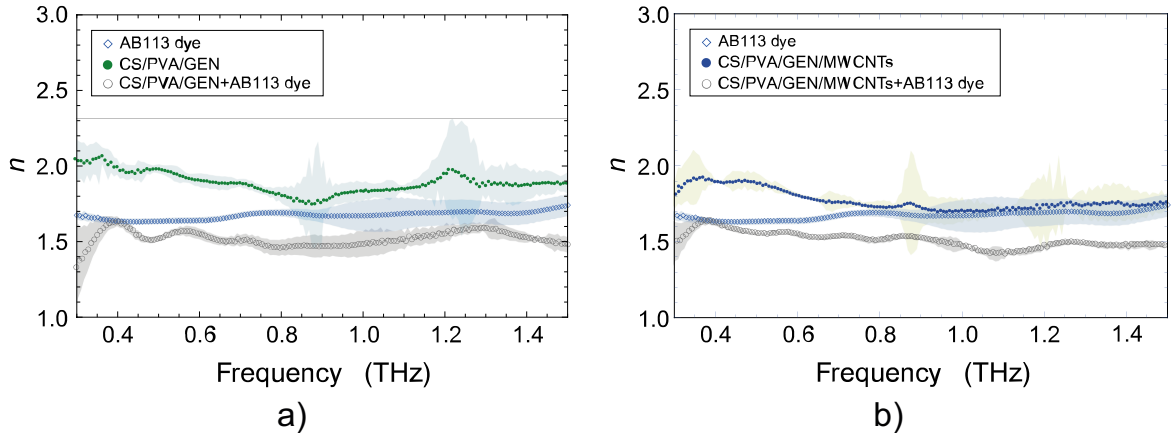

Figure 2. Refractive index, n, of the AB113 dye pressed pellet (unfilled blue diamonds) and the dry hydrogel membranes, both with and without AB113 dye (unfilled gray circles and solid color circles, respectively). a) CS/PVA/GEN cross-linked hybrid hydrogel, b) CS/PVA/GEN/MWCNTs nanocomposite hydrogel.

The real part of the refractive index for the dry hydrogels before and after AB113 adsorption is shown in Figs. 2a) and 2b) (solid-colored circles and unfilled gray circles, respectively). Pristine hydrogels exhibit a dispersive refractive index ranging from 2.05 to 1.76 as frequency increases. After AB113 uptake, the spectra become flatter and display consistently lower refractive index values. These variations arise from the incorporation of dye molecules into the polymer network, which increases the intermolecular spacing and the specific volume of the material, effectively reducing its density and increasing the propagation velocity of THz radiation through the medium [7]. The refractive index changes confirm that THz-TDS is highly sensitive to the sorption behavior of the hydrogels toward the AB113 azo dye.

Conclusions

CS/PVA/GEN and CS/PVA/GEN/MWCNTs hydrogels demonstrated effective adsorption of the azo dyes MO and AB113, with adsorption behavior strongly influenced by the physicochemical characteristics of each dye and the solution pH. MO exhibited rapid adsorption and early stabilization of q_t, whereas AB113 adsorption proceeded more slowly due to its larger molecular size. The incorporation of MWCNTs reduced the number of available polar functional groups, slightly decreasing adsorption capacities compared with the CNT-free hydrogels. Non-linear kinetic modeling showed that the PFO model provided the best fit for both dyes, indicating that physisorption dominates the adsorption mechanism through electrostatic attraction, hydrogen bonding, and π-type interactions. Overall, the materials exhibit suitable adsorption performance and well-defined physicochemical interaction pathways, supporting their potential for applications in dye removal from aqueous media.

References

1. Hashemi, S.H. and M. Kaykhaii, *Chapter 15 - Azo dyes: Sources, occurrence, toxicity, sampling, analysis, and their removal methods*, in *Emerging Freshwater Pollutants*, T. Dalu and N.T. Tavengwa, Editors. 2022, Elsevier. p. 267-287.
2. Zhang, N., et al., *Recent investigations and progress in environmental remediation by using covalent organic framework-based adsorption method: A review.* Journal of Cleaner Production, 2020. **277**: p. 123360.
3. Garnica-Palafox, I.M., et al., *Influence of Genipin and Multi-walled Carbon Nanotubes on the Dye Capture Response of CS/PVA Hybrid Hydrogels.* Journal of Polymers and the Environment, 2022. **30**(11): p. 4690-4709.
4. Ruíz-Nieto, L.G., et al., *Sponge shape semi-interpenetrating polymeric networks based on PDMS/CS/PVA/GEN to capture an azo dye.* Journal of Materials Science, 2025. **60**(38): p. 18113-18135.
5. Garnica-Palafox, I.M. and F.M. Sánchez-Arévalo, *Influence of natural and synthetic crosslinking reagents on the structural and mechanical properties of chitosan-based hybrid hydrogels.* Carbohydrate Polymers, 2016. **151**: p. 1073-1081.
6. Abdel Maksoud, M.I.A., et al., *Effect of gamma irradiation on the free-standing polyvinyl alcohol/chitosan/Ag nanocomposite films: insights on the structure, optical, and dispersion properties.* Applied Physics A, 2021. **127**(8): p. 619.
7. Garnica-Palafox, I.M., et al., *Terahertz Detection of Acid Blue 113 Dye Using Hybrid Hydrogels.* Journal of Infrared, Millimeter, and Terahertz Waves, 2024. **45**(3): p. 300-321.

Acknowledgements

Funding is from UNAM-DGAPA (PAPIIT IG101424, IN115924, IN101824 and IN101624). I.M. Garnica-Palafox would like to thank DGAPA-UNAM for the fellowship received to conduct her postdoctoral research at ICAT-UNAM.

Polymat Contributions

Evaluation of the Electrical Properties in $SrTiO_3$-Based Ceramic Materials by Impedance Spectroscopy

L. Martinez-Hernandez[1,3], E. Pradal-Velazquez[1], J. Prado-Gonjal[2] and A. Reyes-Montero[3]

[1]Faculty of Chemistry, National Autonomous University of Mexico, Mexico; lavismartinez@gmail.com
[2]Faculty of Chemical Sciences, Complutense University of Madrid, Spain.
[3] Materials Research Institute, National Autonomous University of Mexico, Mexico.

Abstract

The present work shows $SrTiO_3$-based ceramic materials co-doped with Sm^{3+} and Nb^{5+} synthesized through the conventional solid-state reaction route. Structural analysis by X-ray diffraction confirmed the successful formation of the characteristic perovskite structure. Complementarily, scanning electron microscopy revealed progressive grain refinement and well-formed intergranular contacts across the doped compositions, indicating an effective sintering process.

The incorporation of Sm^{3+} and Nb^{5+} ions directly modify the concentration and mobility of charge carriers in the perovskite, altering its electrical response. The controlled structural substitution adjusts the resistivity and conduction mechanisms of the material. Doping both sites of the perovskite enhanced the electrical conductivity of the ceramic.

Introduction

Strontium titanate ($SrTiO_3$) is a ceramic material with a perovskite-type structure that exhibits a cubic crystalline arrangement at room temperature. $SrTiO_3$ is characterized by remarkable photocatalytic and electrical properties (such as for energy conversion) [1], excellent thermal stability, resistance to corrosion, and a strong structural robustness [2]. Additionally, the formation of solid solutions has been shown to enhance cation mobility within the lattice.

Doping with elements such as niobium (Nb^{5+}) and samarium (Sm^{3+}) modifies the crystal structure and the electrical properties of the ceramic, by the formation of solid solutions [3]. When donor dopants are incorporated into the A or B sites of the perovskite lattice, electrons are introduced into the vacant t_{2g} orbitals, resulting in a unique combination of a high thermal and good electrical conductivity, attributed to the large effective carrier mass and the degenerate conduction band of the material.[4]

In this work, doped $SrTiO_3$-based materials were prepared via solid-state synthesis. The effects of Nb^{5+} and Sm^{3+} ions on the electrical properties of the ceramics were evaluated by impedance spectroscopy.

Experimental

$SrTiO_3$ and its solid solutions were synthesized by mixed oxide conventional route. The stoichiometric mixture of reagents was milled for 6 h with 3 mm zirconia balls. Then, the powders were calcined at 900 °C for 1 h, and milled again for 3 h. Afterwards, the mixture was dried. Then, the powders were pressed at 3 ton to form pellets of ~10.0 mm in diameter and ~1 mm in thickness and sintered at 1400 °C for 2 h.

For the structural characterization, X-ray diffraction (XRD) was performed with Cu-Kα radiation (1.5419 Å, Bruker AXS D8 Advance with a 0.02° step size in 2θ). A LEICA Stereoscan 440 emission scanning electron microscope (SEM) was used to assess the morphology of the samples, and the acquired images were further analyzed through ImageJ software. The bulk

density of the sintered ceramics was measured by the Archimedes method using distilled water as a medium. For electrical characterization, the pellets were polished and silver paste was applied on both sides of the pellet. Then, the paste was fired at 550 °C for 10 min to form electrodes. The impedance spectra were measured between 10^{-1} and 10^{7} Hz with a precision impedance analyzer (SOLARTRON 1260A) from temperatures ranging between 400 °C to 600 °C.

Results and discussion

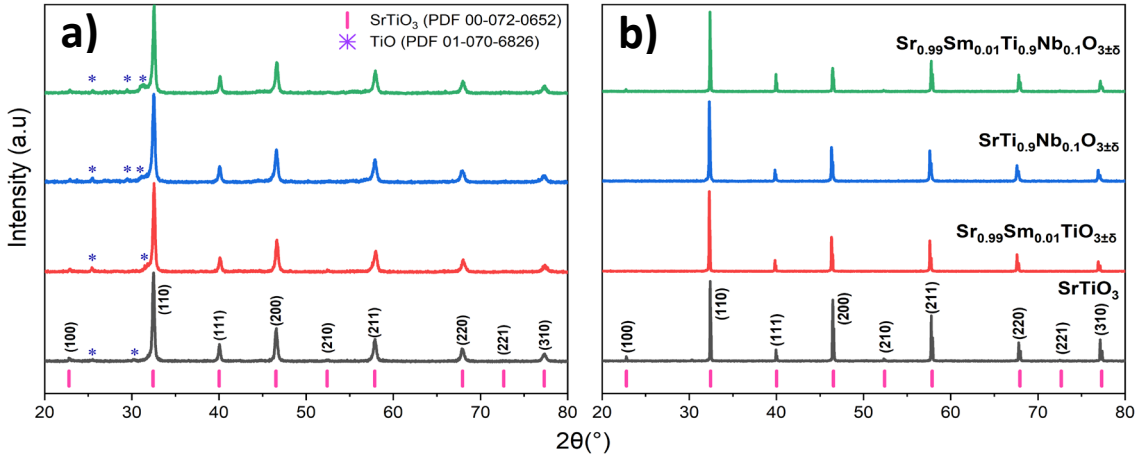

Figure 1. XRD patterns of the a) powder calcined at 900 °C/1 h and b) pellets sintered at 1400 °C/2 h.

The XRD patterns of the ceramic powders and pellets are shown in Figure 1. For the calcined powders (Figure 1a), a perovskite phase was formed, although peaks from a secondary phase (TiO_2) are observed. After the sintering process (Figure 1b), a single-phase material is observed resulting in a single-phase perovskite structure. The diffraction peaks of the samples were indexed to the perovskite-type cubic prototype phase.

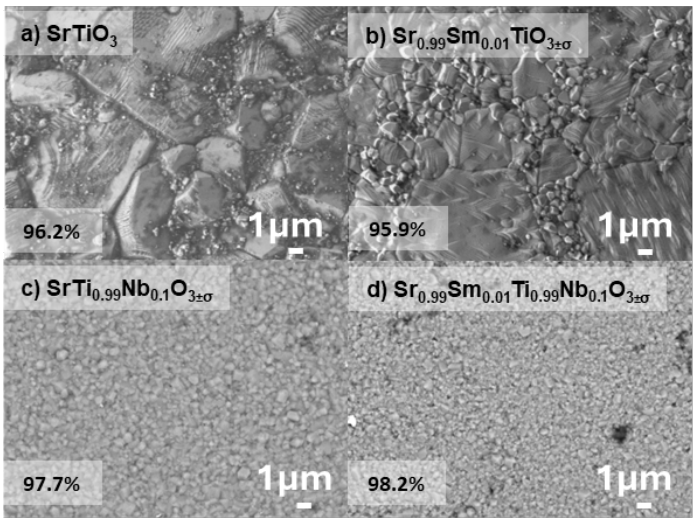

Figure 2. SEM micrographs of $SrTiO_3$ and calculated densification.

Figure 2 shows the surface of the sintered samples $SrTiO_3$ and solid-solutions with Sm^{3+} at the A-site and Nb^{5+} at the B-site. The undoped sample exhibits large and defined grains with a densification of 96.2 %, related to an unrestricted grain growth during the sintering process. However, each dopant exerts a distinct effect: Sm leads to a more heterogeneous microstructure and slightly decreases densification (95.9 %), whereas Nb produces a finer and more homogeneous grain structure, achieving a higher densification among these samples (> 97 %), while the Sm–Nb co-doped sample results in an even more refined and consolidated microstructure, reaching the highest densification among all studied compositions (> 98 %).

Impedance spectroscopy is an analytical technique that offers extensive and valuable information on the electrical response of different regions in the ceramic. Figure 3a presents the complex impedance plots for $SrTiO_3$ and solid solutions evaluated at temperatures ranging from 400 °C to 600 °C. As the temperature increases, the resistance clearly decreases as observed in Figure 3a.

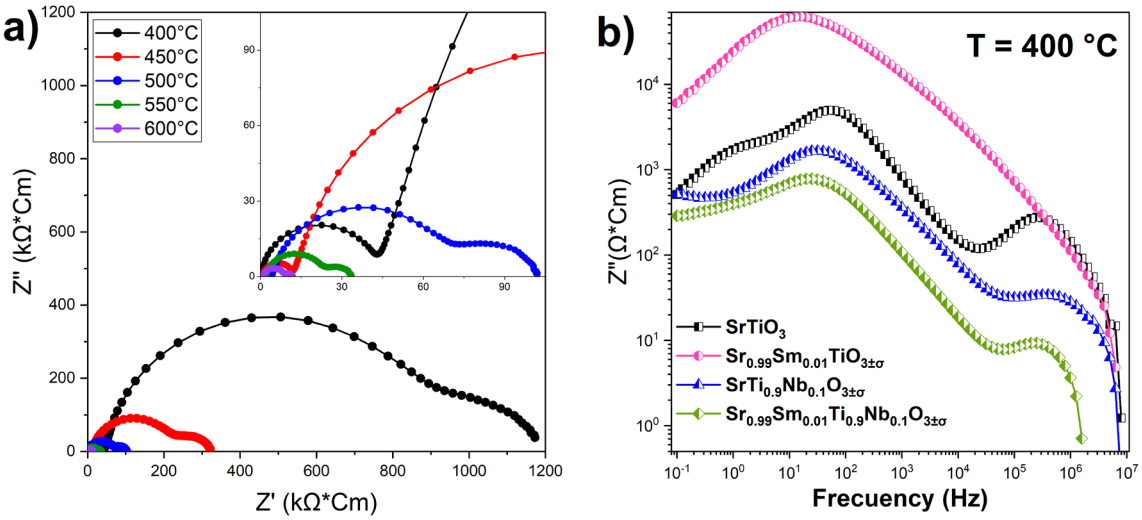

Figure 3. a) Complex impedance plots for $SrTiO_3$ at different temperatures and b) Z'' spectroscopic plots for $SrTiO_3$ and its solid solutions.

In figure 3b, the Z″ spectra for all compositions at 400 °C are shown, maxima associated with different regions are appreciated, these were identified with the capacitance values calculated using the Z″ maxima and their corresponding peak frequencies. Capacitances on the order of ~10^{-10}–10^{-9} F for the high frequency responses were assigned to the bulk response, values of ~10^{-11}–10^{-8} F for the intermediate frequency element were identified as grain boundary contributions, and the low frequency responses with capacitances of ~10^{-7} - 10^{-5} F were assigned as electrode responses [5]. At low frequencies, the undoped sample exhibits two well-defined maxima, suggesting the coexistence of two relaxation processes: one corresponding to the electrode interface and another attributable to the grain boundary. In contrast, the doped samples display only a single response in the low-frequency region, associated with the electrode. At higher frequencies they exhibit a response corresponding to the bulk. The sample doped only at the A-site of the perovskite (Sm^{3+}) shows a distinct behavior: it presents only one broad maximum at low frequencies, and the impedance does not decrease but instead increases, resulting in a much higher peak. This more resistive grain boundary response masks the bulk contribution. The increase in Z″ reflects a significant rise in

internal resistance produced by the incorporation of Sm^{3+} ions. Whereas in the other compositions the overall behavior remains qualitatively similar to undoped $SrTiO_3$. This effect indicates that the incorporation of dopant ions modifies the relaxation dynamics, allowing certain contributions to become more distinguishable, although not necessarily dominant in all cases.

Conclusions

- $SrTiO_3$-based solid solutions were successfully obtained with the optimized synthesis and sintering conditions. For ceramic powders a small amount of TiO_2 traces are observed.
- Microstructural analysis showed a progressive reduction on the grain size with a homogeneous microstructure in the samples with the incorporation of Nb^{5+}.
- The Archimedes method confirmed densifications greater than 95%.
- The incorporation of Sm^{3+} increased the grain boundary resistive and strengthened the interfacial relaxation process, whereas Nb^{5+} doping lowered it by acting as a donor dopant that enhance the electrical conductivity. These opposite effects confirm the critical role of doping chemistry in the fine tuning of the electrical properties of $SrTiO_3$.

References

[1] Zhou, E.; Raulot, J.-M.; Xu, H.; Hao, H. 2022, Phys. B: Condens. Matter, 643, 414160. Structural, electronic, and optical properties of rare-earth–doped $SrTiO_3$ perovskite: A first-principles study.

[2] Sahu, M. 2014, Microstructural Evolution in Strontium Titanate. KIT Scientific Publishing, Germany.

[3] Adindu, C.; Ivasara, I.; Schmidt, W. L.; Boston, R.; Sinclair, D. C.; Reaney, I. M. 2017, Mater. Today: Proc., 4, 12360–12367.La- and Sm-codoped $SrTiO_{3-\delta}$ thermoelectric ceramics.

[4] Prado-Gonjal, J.; López, A. C.; Piñacca, R. M.; Serrano-Sánchez, F.; Nemes, N.; Durán, A.; Martínez, L.; Fernández-Díaz, M. T.; Alonso, J. A. 2020, Crystals, 10, 100.Correlation between crystal structure and thermoelectric properties of $SrTiO_3Nb_{0.10}Sm_{0.03\pm\delta}$ ceramics.

[5] Irvine, J. T. S.; Sinclair, F.; West, A. R. 1990, Adv. Mater., 2, 935–964. Electroceramics: Characterization by impedance spectroscopy.

Acknowledgements

Armando Reyes-Montero acknowledges UNAM-DGAPA (PAPIIT IN115625) for financial support. The authors thank LUME team from LUME RRID:SCR_024400 for SEM for the image acquisition and technical support. Also, authors thank Adriana Tejeda (IIM-UNAM) for XRD data acquisition and technical support.

Polymat Contributions

Study of incorporation of crystalline nanocellulose into an automotive paint for noise isolation

Fabrizo Sosa Castillo[1], Leonel Toledo Sesma[2], Diana Palma Ramírez[2*],

*[1]Instituto Politécnico Nacional, Unidad Profesional Interdisciplinaria de Ingeniería Campus Hidalgo (UPIIH), Pachuca 42162, México, *dpalmar@ipn.mx*

Abstract

This work deals with nanocellulose (NC) extracted from commercial cellulose, which is studied to be dispersed into an automotive paint and evaluate the structural, morphological, and some physical properties associated with the isolation properties of a car cabin. NC was isolated from commercial cellulose and dispersed in 1, 3, and 5 wt% into acrylic paint. The analysis includes Raman spectroscopy, X-ray diffraction, confocal laser scanning microscopy, optical analysis, and sound pressure tests, which provide information about the functional groups of each phase and additives, crystalline structure, dispersion features, and acoustic properties. Optimal acoustic results were found using 5 wt% of NC into the commercial paint.

Introduction

In the automotive industry, changes have been made through the development of new materials, achieving a significant economic impact. The material sector in the automotive industry has focused on meeting consumer expectations by obtaining lighter, more sustainable, and functional materials in terms of driving comfort, safety, and ergonomics [1].

Traditional materials, which were once effective at dampening chassis noise, are used in minimal thickness or replaced by lighter polymer-based components. As a result, users of modern vehicles complain about poor sound insulation. The elevated position of the body seats causes greater air resistance, and the large tires, greater rolling resistance, which generates more noise while driving. The leading companies in the automotive acoustic materials industry are: 3M, Harman International Industries, Inc. (Samsung Electronics), BASF SE, Covestro, DOW Chemicals, du Pont de Nemours and Company (DuPont), Tex Tech Industries, LyondellBasell, Sika AG, Toray Industries, Henkel, Rockwool International, Fabri-Tech Components, Huntsman International LLC, Saint-Gobain Ecophon AB, and Thomas net (Thomas Industrial Network, Inc.), among others. Automotive acoustic materials are expected to be the focus by 2032 [2-4].

The current trend is the development of new materials to produce functional acoustic products that can have a competitive advantage in the automotive market [5, 6]. For this reason, the aforementioned companies focus on the development of new materials. Sound pollution is a serious problem that affects us all, and multiple researchers have investigated ways to prevent it, focusing on fibers with high porosity which have the capacity to absorb sound [4, 5]. Therefore, this work focuses on the dispersion of NC fibers obtained in the laboratory through chemical methods in a commercial paint used for car bodies in the automotive industry in order to evaluate the effect of incorporating different percentages on the improvement or deterioration of acoustics.

Methodology

A commercial white automotive paint (PR) was used as the base material and mixed with NC at 0.1, 1, 3 and 5 wt%. The mixtures were homogenized using an ultrasonic bath. The samples were characterized using Raman spectroscopy, X-ray diffraction (XRD), confocal laser scanning microscopy, optical microscopy, and sound pressure measurements. Raman spectra were obtained with a LabRAM HR800 spectrometer (200–4000 cm^{-1} range, 50× objective). XRD patterns were recorded with a Bruker D2 Phaser diffractometer. Fluorescence imaging was performed using a Carl ZEISS LS 700 confocal microscope with a 405 nm wavelength at room temperature. Optical microscopy involved placing a drop of paint on a coverslip and analyzing it with an FCM 5000 metallographic microscope. For acoustic tests, aluminum alloy boxes (40 × 10 × 10 cm) were coated internally with a 110 nm thick paint layer containing the different NC concentrations. The sound pressure level measurement was carried out with a sound meter in a range of minimum and maximum dB.

Results and discussion

Raman spectrum shows signals of functional groups of acrylic binder corresponding to the PR and the pigment, TiO_2 (Figure 1a). Upon the addition of NC (Figure 1b), no significant difference was observed due to low content incorporation [6]. The X-ray diffraction patterns (Figure 2) for the PNC sample show the (110), (101), (200), (111), (210), (211), (220), (310) and (112) crystallographic planes, corresponding to rutile tetragonal phase (PDF #01-089-4921) and (204) and (220) planes of tetragonal anatase phase (PDF # 01-089-4921) with no significant changes compared to PR. A low-intensity signal was observable at low diffraction angles, which is specifically attributed to the NC fibers belonging to mixture of type I and II polymorphs. It is also important to note that the characteristic peaks of the acrylic paint matrix were not detected due to the amorphous nature of the polymer coating; consequently, the resulting diffractograms are exclusively dominated by the signals from the crystalline pigment. Confocal microscopy (Figure 3) was employed to assess the dispersion of the NC within the PR. However, the intrinsic fluorescence generated by the paint significantly interfered with the measurements, thereby preventing accurate visualization of the particle dispersion. Conclusive images regarding the homogeneous distribution of NC could not be obtained. The results of optical analysis (Figure 4) demonstrated that the NC addition induced the formation of agglomerates. In the 0.1 wt% formulation, the agglomerations were small and nearly imperceptible. The visibility and size of these agglomerates increased proportionally with the increasing NC percentage in the PR. By analyzing higher magnification to these agglomerated regions, it was possible to resolve smaller structures. Nevertheless, the resolution limit of the 40x objective prevented the visualization of particles smaller than this limit.

The acoustic performance of the coatings was evaluated by applying white noise to the aluminum boxes coated with the PR and the NC-modified paints (PNC) at 1 wt%, 3 wt%, and 5 wt%. The PR exhibited a sound pressure level ranging from a minimum of 76.1 dB to a maximum of 82.9 dB when subjected to white noise. The coatings containing NC generally achieved a modest percentage of reduction. The highest reduction was observed at 5 wt% NC concentration, where the minimum SPL decreased by 1.83 % (equivalent to 1.4 dB and the maximum decreased by 0.60 (equivalent to 0.5 dB). An exception was the NC 1 wt% coating, which registered a minimum 76.5 dB, slightly higher than the PR 76.1 dB, indicating a minimal acoustic performance change at this concentration.

Polymat Contributions

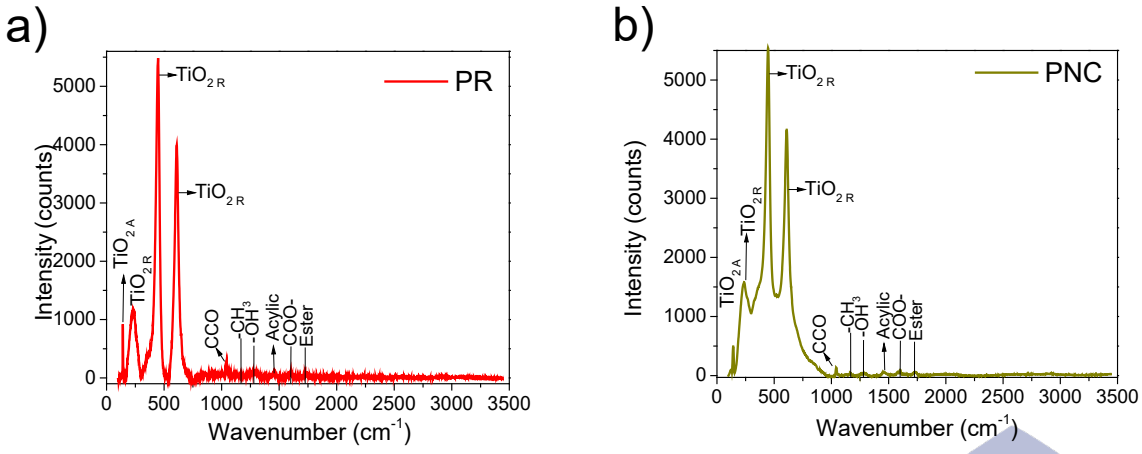

Figure 1. Raman spectra of PR (a) and PNC (b).

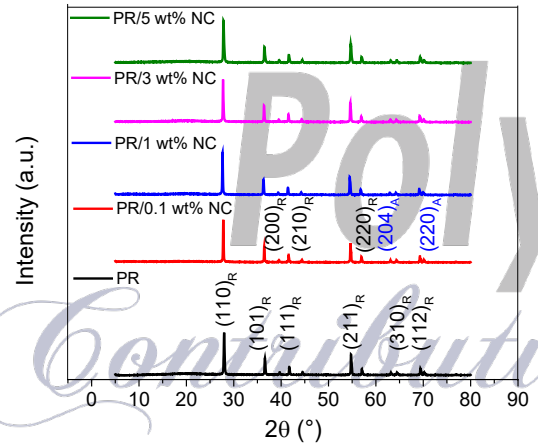

Figure 2. XRD pattern of PR and PR/NC.

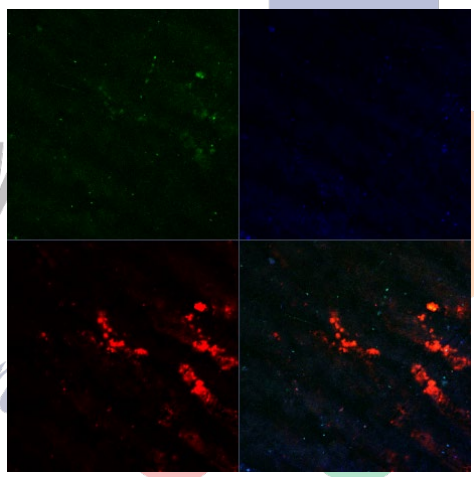

Figure 3. CLSM micrograph of NC in PR.

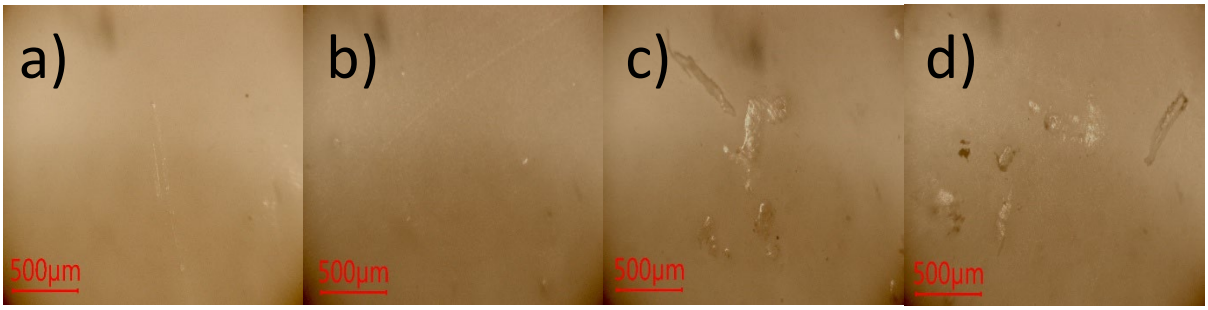

Figure 4. Optical micrographs a) PR/0.1 wt% NC, b) PR/1 wt% NC, c) PR/3 wt% NC, d) PR/5 wt% NC.

Table 1. Sound pressure test results

PR with NC wt%	Minimum (dB)	Maximum (dB)
PR	76.1	82.9
NC 1 wt%	76.4	82.7
NC 3 wt%	75.9	82.6
NC 5 wt%	74.7	82.4

Conclusion

Raman spectroscopy confirmed the successful chemical extraction of cellulose without structural changes and the identification of TiO_2 pigments and acrylic functional groups in the PR. XRD analysis revealed cellulose as a mixture of polymorphs (types I and II) and confirmed TiO_2 crystalline phases, with no structural changes in the PR after adding NC. There was no possibility to evaluate the NC dispersion because the fluorescence of the PR. Optical microscopy showed visible agglomerates of smaller clusters for NC. The acoustic evaluation indicates that NC-modified coatings provide only a slight improvement in sound attenuation compared to the PR. The best performance was achieved at 5 wt% NC, reducing the minimum SPL by 1.4 dB and the maximum by 0.5 dB. Lower concentrations (1 and 3 wt%) showed negligible or inconsistent effects. Overall, NC addition offers limited acoustic benefits at the tested concentrations. For further investigations, it is recommended to compare with microcellulose.

References

1. Ghosh, G., R. Bhattacharyya, and D. Penumadu, *Advances in multi-functional composite materials: applications and opportunities in automotive industry*. Functional Composites and Structures, 2025. **7**(4): p. 042001.
2. Yang, T., et al. *Sound Absorption Properties of Natural Fibers: A Review*. Sustainability, 2020. **12**, DOI: 10.3390/su12208477.
3. Elkasaby, M.A. *Development of polymer based nanocomposite using electrospinning for sound absorption and isolation*. 2017.
4. Dumbre, R. Chavan, and S. Devi, *Impact of Noise Pollution on the Health of Car Drivers – A Review Article.* Universal Journal of Public Health, 2024. **12**: p. 266-270.
5. Yang, T., et al., *Acoustic evaluation of Struto nonwovens and their relationship with thermal properties.* Textile Research Journal, 2016. **88**.
6. Silva, R., J. Ferreira, and Á. Meneguzzi, *Anticorrosive acrylic intelligent paint.* Chemical Papers, 2019. **74**: p. 631–639.

Acknowledgements

Authors are grateful for financial support provided by Instituto Politécnico Nacional (IPN) through SIP20251064 projects.

Polymat Contributions

Valorization of single-use cups into interpenetrating polymer networks based on PMMA/PU/PMMA-g-cellulose

Mayra E. Juárez Méndez[1,2], S. Beatriz Brachetti Sibaja[2], Diana Palma Ramírez[1*]

*[1] Instituto Politécnico Nacional, Unidad Profesional Interdisciplinaria de Ingeniería Campus Hidalgo (UPIIH), Department of Polymers and Nanomaterials, Pachuca, Hidalgo, 42162, México, *dpalmar@ipn.mx*

[2]Tecnológico Nacional de México-IT de Ciudad Madero, D.E.P.I., México

ABSTRACT

The objective of this work is to present the results of the chemical structure identification of cellulose fibers extracted from used carbonated-beverage cups. The functional groups were analyzed by Fourier-transform infrared spectroscopy (FTIR). The reduction in fiber diameter resulting from acid concentration was evaluated using dynamic light scattering (DLS). Raman spectroscopy was used to confirm the chemical information of the cellulose, whereas the decrease in fiber size was observed using scanning electron microscopy (SEM). Dispersion of cellulose particles was performed into an interpenetrating polymer network (IPN) to evaluate the tensile properties, and the dispersion was analyzed using confocal laser scanning microscopy (CLSM).

Keywords: hydrolysis, nanocellulose, polymorphs.

INTRODUCTION

The excessive use of single-use plastics—particularly carbonated beverage cups—and the improper disposal of their waste have contributed to various environmental impacts, including public health risks, loss of biodiversity, and the release of hazardous pollutants. These materials are accumulated in landfills, burned, scattered onto soil, or transported by wind and waterways. They degrade over time into microplastics, remaining trapped in the environment. Carbonated beverage cups are generally not recycled due to the complexity of their components, consisting of 95% cellulose fibers and 5% polyolefins. Cellulose is a renewable biopolymer that, due to its abundance and biodegradability, can be widely used—for example, as a pharmaceutical excipient and in papermaking, among other applications. The extracted cellulose from other types of raw materials, such as paper dust, has displayed a ribbon-like, rod-shaped morphology with a crystalline structure and a low degradation temperature [1]. Also, the cellulose molecular chains, through the synergistic effect of cations and anions, have been reported to successfully transform cellulose from type I to type II [2]. This work deals with the cellulose modification through grafting methyl methacrylate (MMA) monomer into it to analyze if particles can be used to improve the mechanical properties of interpenetrating polymer networks based on poly(methyl methacrylate) and poly(urethane), having potential applications for outdoor uses.

METHODOLOGY

Cellulose was extracted using a mechanical stirring method and bleached with acetic acid (CH_3COOH) and sodium chlorite ($NaClO_2$). The resulting material was then hydrolyzed with sulfuric acid (H_2SO_4) at concentrations of 40% and 64%. Dynamic light scattering (DLS) was used to determine the polydispersity index (PDI) and hydrodynamic diameter (Hd) of the crystalline cellulose particles isolated from the cellulose fibers. Measurements were performed

using distilled water as the dispersion medium for the hydrolyzed cellulose samples treated with 40% and 64% H_2SO_4. Crystalline cellulose was characterized by Fourier-transform infrared spectroscopy (FTIR) in the range of 4000 to 450 cm^{-1}, using 30 scans to identify the functional groups present. High-resolution photonic characterization using vibrational spectroscopy was performed with a spectrometer coupled to a microscope. Measurements were carried out over a wavenumber range of 200 to 4000 cm^{-1}, using a 600 lines/mm grating and a 785 nm excitation laser. Grafting reaction was performed according to [3] using x = 5, 10, 20 and 30% of cellulose (CNC_x) with MMA monomer to obtain particles which were dispersed into 50/50 PMMA/PU synthesis [4]. Tensile strength and percent elongation were evaluated using a universal testing machine with a 50 kN load capacity, operated at a crosshead speed of 20 $mm \cdot min^{-1}$ and equipped with a 2 kN load cell.

RESULTS

The cellulose fibers treated with 64% H_2SO_4 showed an Hd of 26.70 nm and an average PDI of 0.63, whereas those treated with 40% H_2SO_4 exhibited an Hd of 98.53 nm and an average PDI of 0.27. Figure 1 shows the FTIR spectra comparing the cellulose fibers treated with 40% and 64% H_2SO_4. In both treatments, characteristic cellulose signals were detected, including the O–H stretching at 3370 cm^{-1}, symmetric C–H stretching at 2900 cm^{-1}, C–O stretching at 1050 cm^{-1}, and the glycosidic deformation band at 895 cm^{-1}. The Raman spectra of the crystalline cellulose samples treated with 40% and 64% sulfuric acid are presented in Figure 2. The O–H stretching vibration appears between 3500 and 3200 cm^{-1}. The signals also show a weak band at 2330 cm^{-1} corresponding to a C=C bond vibration, which may be associated with oxidation processes [5]. The region between 1790–1730 cm^{-1} corresponds to C=O stretching attributed to acetylation [6]. O–H bending is observed at 1700 cm^{-1} [129]. Another O–H bending vibration, associated with the hydrogen of water and the hydroxyl groups of the pyranose ring, is detected at 1660 cm^{-1} [7]. Additional bands include HCC and HOC bending at 1445 cm^{-1}, HCC, HCO, and HOC bending at 1383 cm^{-1}, and the HCC and HCO vibrations of cellulose II at 1325 cm^{-1} [8]. The glycosidic ring deformation of cellulose II appears at 1260 cm^{-1} [9]. The deformation of the CCC and CCO ring modes is observed at 491 cm^{-1}, while glycosidic linkages are detected at 700 cm^{-1} [8]. CCH bending was identified at 600 cm^{-1} [10], and the COC glycosidic linkage vibration of cellulose at 491 cm^{-1}, along with additional ring deformation bands (CCC, CCO) at 430 cm^{-1} [9]. The SEM micrographs in Figure 3 ($CNC_{40\%}$, $CNC_{64\%}$), present a ribbon-shaped morphology, consisting of a heterogeneous mixture of fibers with visibly different lengths, widths, and thicknesses. For the mechanical tests, the curve and data of the pure PMMA/PU (50/50) IPN are presented. This material exhibits a rigid mechanical response, achieving a tensile strength of 395 N, a Young's modulus of 104 MPa, with an elongation reaching 10%. After incorporating 0.1 wt% CNC_5 into the 50/50 PMMA/PU system (CNC_5PMMA_{50}/PU_{50}), the sample shows enhanced ductility, with elongation rising to 33%. Likewise, both the Young's modulus (25 MPa) and the tensile strength (154 N) decrease. A comparable trend was noted with the addition of 0.1 wt% CNC_{20}, leading to a slight decrease in tensile strength (97 N) and elongation (26%) relative to CNC_5PMMA_{95}. A Young's modulus of 24 MPa was obtained for this system, comparable to the value measured for CNC_5.

Conversely, when the CNC content was increased to CNC_{30} the curves shifted toward those of the pure PMMA/PU system, showing a high tensile strength (458 N), a Young's modulus of 121 MPa, and an elongation of 10%. In comparison with the pure IPN, incorporating an intermediate CNC level — 0.1 wt% of the CNC_{10} system — resulted in the most favorable tensile properties for its use as a reinforcing agent. In this case, the Young's modulus and tensile strength slightly decreased to 73 MPa and 285 N, respectively. Additionally, the

elongation increased to 52%, representing a fourfold improvement over pure PMMA/PU. Finally, the CLSM micrograph in Figure 5 displays a well dispersion of the CNC particles into the PMMA/PU IPN.

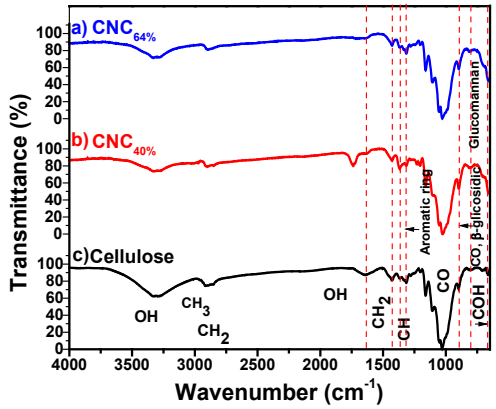

Figure 1. FTIR spectrum of Cellulose, $CNC_{40\%}$ and $CNC_{64\%}$.

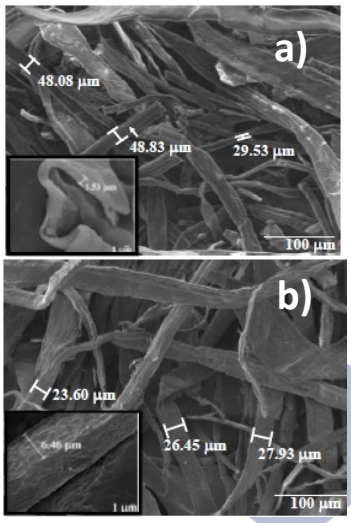

Figure 2. SEM micrographs of a) $CNC_{40\%}$ and b) $CNC_{64\%}$.

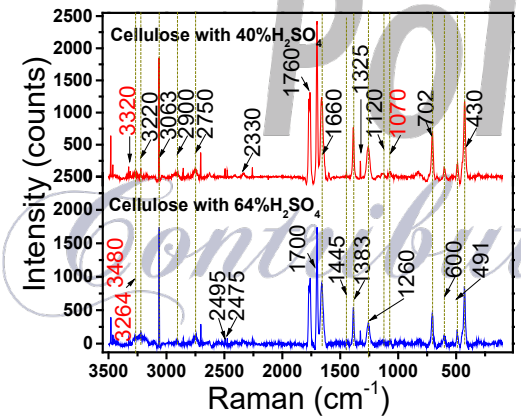

Figure 3. Raman spectrum of $CNC_{40\%}$ and $CNC_{64\%}$.

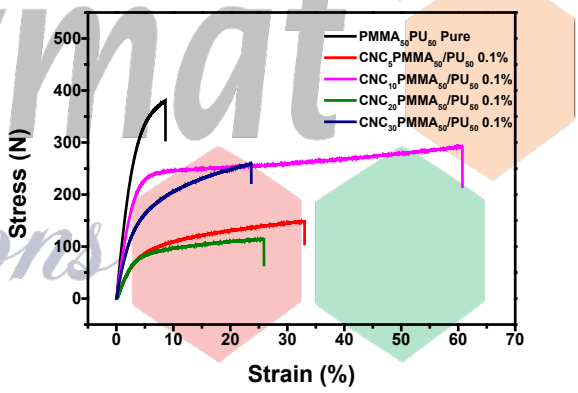

Figure 4. Stress vs. strain curves of CNC_xPMMA_{50}/PU_{50} IPNs

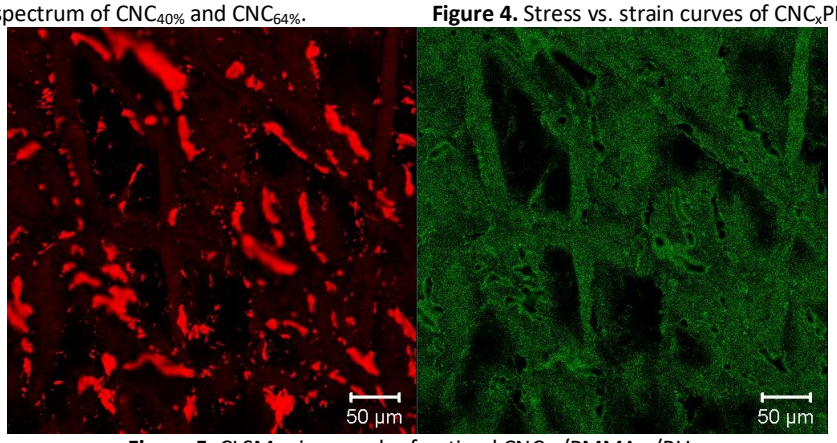

Figure 5. CLSM micrograph of optimal $CNC_{10}/PMMA_{50}/PU_{50}$

CONCLUSIONS

Based on the DLS analyses of the fibers treated with 40% and 64% H_2SO_4, CNC was obtained. The acid concentration also contributed to reducing particle size by promoting more complete cellulose degradation; in contrast, concentrations that are too low yield only fibers and large, poorly dispersed aggregates. The structural analysis revealed the characteristic features of cellulose. IPNs of pure PMMA/PU at a 50/50 ratio were successfully prepared, and its tensile properties were evaluated upon incorporation of 0.1 wt% dispersed PMMA-g-CNC (CNC_5, CNC_{10}, CNC_{20}, and CNC_{30}). The proposed reinforcing agents generally rendered the 50/50 PMMA/PU IPNs more ductile, leading to a reduction in tensile strength and Young's modulus. Among the materials studied, the CNC_{10} formulation exhibited the most favorable overall performance with good dispersion.

REFERENCES

[1] Chen J *et al.* Synthesis and structure of carboxymethylcellulose with a high degree of substitution derived from waste disposable paper cups. Carbohydr. Polym. 2020; 237 116040.

[2] Xu Z *et al.*, "Transparent Cellulose-Based Films Prepared from Used Disposable Paper Cups via an Ionic Liquid," *Polymers*, vol. 13, no. 23, doi: 10.3390/polym13234209.

[3] Juárez-Méndez ME *et al.* CNCs extraction from single-use cups: effects of grafting it onto MMA monomer. Journal of Chemical Technology & Biotechnology. 2023; 98 (8): 1847-1862.

[4] Juárez-Méndez ME *et al.* Study of cellulose extraction from disposable cups for potential application as a reinforcement of engineering polymers. MRS Advances. 2021; 6 (38): 881-884.

[5] Alves APP *et al.* The structure of different cellulosic fibres characterized by Raman spectroscopy. Vibrational Spectroscopy. 2016; 86 324-330.

[6] Adebajo MO, Frost RL, Kloprogge JT, and Kokot S. Raman spectroscopic investigation of acetylation of raw cotton. Spectrochimica Acta Part A: Molecular and Biomolecular Spectroscopy. 2006; 64 (2): 448-453.

[7] Fujisawa R *et al.* Dynamical study of the water penetration process into a cellulose acetate film studied by coherent anti-Stokes Raman scattering (CARS) microspectroscopy. Chemical Physics Letters. 2016; 655-656 86-90.

[8] Wiley JH and Atalla RH. Band assignments in the raman spectra of celluloses. Carbohydrate Research. 1987; 160 113-129.

[9] Schenzel K and Fischer S. NIR FT Raman Spectroscopy–a Rapid Analytical Tool for Detecting the Transformation of Cellulose Polymorphs. Cellulose. 2001; 8 (1): 49-57.

[10] Kavkler K and Demšar A. Examination of cellulose textile fibres in historical objects by micro-Raman spectroscopy. Spectrochimica Acta Part A: Molecular and Biomolecular Spectroscopy. 2011; 78 (2): 740-746.

ACKNOWLEDGEMENTS

M.E. Juárez-Méndez expresses gratitude for her postgraduate fellowship to CONAHCYT. Authors are grateful for financial support provided by Instituto Politécnico Nacional (IPN) through SIP20251064 project as well as SNII-SECIHTI.

OPTIMIZATION OF MILLING TIME FOR NANOBIOCHAR PRODUCTION

Aneyda Yadira Popoca Bustos [1], Melchor Solis Santos [2], María LuisaGarcía Betancourt[2]*

[1]*Facultad de Farmacia, UAEM Av. Universidad 1001 Col. Chamilpa, 62209 Cuernavaca, Morelos, México*

[2]*Centro de Investigaciones Químicas, UAEM Av. Universidad 1001 Col. Chamilpa, 62209 Cuernavaca, Morelos, México; mluisa.garcia@uaem.mx.**

Introduction

Nanobiochar derived from biomass is a porous carbon material with potential applications in environmental remediation, soil enhancement, contaminant adsorption, and energy storage. Used in water remediation and as an additive in various products, nanobiochar offers sustainable solutions to current challenges. Combining biochar technology with nanotechnology can revolutionize research by producing nanobiochar with excellent contaminant absorption capacity and soil mobility [1-2]. This study aims to optimize the milling time for nanobiochar production, specifically analyzing how milling duration influences its structural and functional properties. The objective is to establish optimal parameters that maximize efficiency and quality through characterization and evaluation.

Materials and methods

Biochar preparation: Approximately 3.828 g of dried Machaerium isadelphum leaves were pyrolyzed at 340 °C for 10 min in a quartz tube inside a Thermo Scientific Lindberg Blue/Blue M tubular furnace. A constant argon flow of ~0.2 L/min was maintained to ensure an inert atmosphere.

Nanobiochar preparation: Milling was carried out in an Anton Paar BM500 steel ball mill at 20 Hertz for 10, 20, and 30 min. The names of the five samples were leaves, biochar, NB10, NB20, and NB30.

Characterization: Dispersibility was evaluated following 5 min of agitation in different media: deionized water, glycine solution, acetone, and ethanol. Characterization techniques included thermogravimetric analysis (TGA), Fourier-transform infrared spectroscopy (FTIR), and Raman spectroscopy was performed to evaluate nanobiochar properties.

Results and discussion

Figure 1 shows the photographs of (A) leaves before pyrolysis (3.828 g) and (B) biochar (1.420 g); the mass was reduced by 63.2%. (C) nanobiochar after milling in a ball mill.

Figure 1. (A) Leaves before pyrolysis, (B) biochar, and (C) nanobiochar after milling.

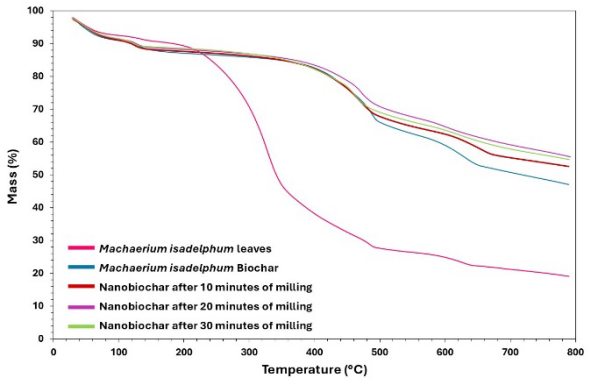

Figure 2. Thermogravimetric Analysis (TGA) of MI stem, biochar, NB10, NB20 and NB30.

Figure 2 shows that all samples exhibit mass loss due to moisture evaporation 100 °C. The leaves display additional weight loss above 250 °C, associated with the degradation of cellulose, hemicellulose, and lignin (above 600 °C) [4]. Biochar and nanobiochar samples (NB10, NB20, NB30) demonstrate higher thermal stability, retaining approximately 50% of their mass at 800 °C.

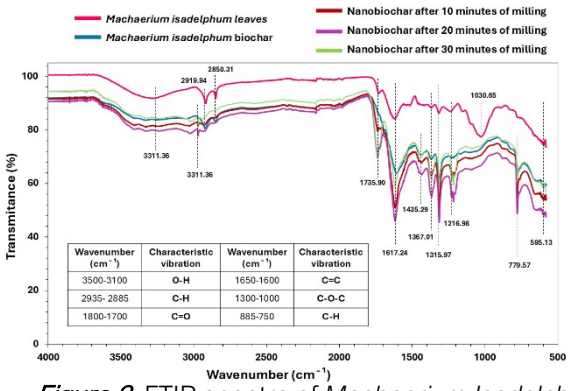

Figure 3. FTIR spectra of *Machaerium Isadelphum* stem, biochar, NB10, NB20 and NB30.

Figure 3 displays FTIR spectra of leaves showing carboxylic and C-O groups [4]. Biochar and NB samples display O-H, carboxylic, C-O, C-C, and C=C groups [3]. NB20 (purple line) stands out with higher intensities, indicating greater surface functionalization [4].

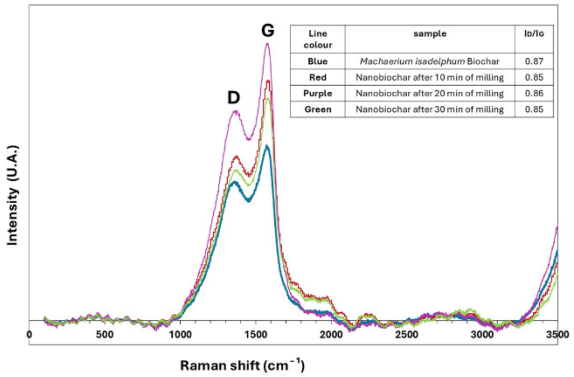

Line colour	sample	Id/Ig
Blue	*Machaerium isadelphum* Biochar	0.87
Red	Nanobiochar after 10 min of milling	0.85
Purple	Nanobiochar after 20 min of milling	0.86
Green	Nanobiochar after 30 min of milling	0.85

Figure 4. Raman spectra of Machaerium Isadelphum stem, biochar, NB10, NB20 and NB30.

Figure 4 reveals Raman spectra highlighting D (~1300 cm^{-1}) and G (~1600 cm^{-1}) bands. The D band indicates the presence of defects or non-sp^2 carbon, while the G band corresponds to sp^2 carbon formation [5]. The similar ID/IG ratio suggests that milling did not modify the biochar's structure.

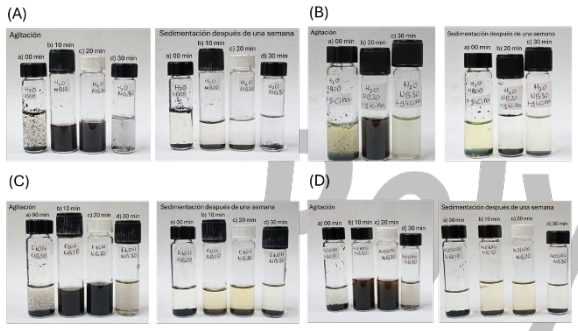

Figure 5. (A) Samples with water, (B) Samples with water and glycine, (C) Samples with ethanol, and (D) Samples with acetone.

Figure 5 shows the dispersibility in aqueous media. Dispersed NB in water is observed; after one-week, small particles remain suspended, indicating colloidal stability, high dispersibility, and effectiveness [6].

Figure 6. Fluorescence test.

Figure 6 demonstrates that nanobiochar emits fluorescence, primarily attributed to aromatic structures and oxygenated functional groups [7]. Glycine further intensifies fluorescence, especially NB30.

Figure 7 shows absorption and fluorescence spectra of NB in an aqueous solution. The observed redshift in absorption and

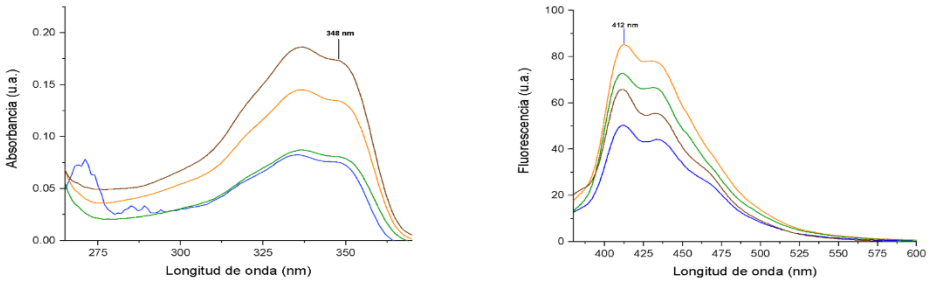

Figure 7. Absorption and fluorescence spectra of NB.

emission bands suggests particle sizes ranging from 40–60 nm. Luminescence intensity varied with concentration (Figure 6), presenting a broad emission band as expected due to the sample's purity.

Conclusions

This work highlights the importance of optimizing milling time to obtain nanobiochar with improved physicochemical properties. Extended milling time improves dispersibility in aqueous media, which also exhibited fluorescence, confirming the functionalization of NB surfaces. Compared to biochar, nanobiochar demonstrates superior adsorption capacity and surface activity, making it more suitable for applications in environmental and catalysis.

References

[1] Chausali, N.; Saxena, J.; Prasad, R. J. Agric. Food Res. **2021**, 5, 100191. https://doi.org/10.1016/j.jafr.2021.100191

[2] Chaubey, A. K.; et al. ACS Omega **2024**, 9 (11), 12331–12379. https://doi.org/10.1021/acsomega.3c07804

[3] Ng, L. Y. F.; Ariffin, H.; Yasim-Anuar, T. A. T.; Farid, M. A. A.; Hassan, M. A. Nanomaterials **2022**, 12 (18), 3251. https://doi.org/10.3390/nano12183251

[4] Khan, H. A.; et al. Chemosphere **2021**, 285, 131382. https://doi.org/10.1016/j.chemosphere.2021.131382

[5] Dresselhaus, M. S.; Jorio, A.; Filho, A. G. S.; Saito, R. Philos. Trans. R. Soc. A **2010**, 368 (1932), 5355–5377. https://doi.org/10.1098/rsta.2010.0213

[6] Jia, Q.; Chen, F.; Li, H.; Zhang, L. Proc. Int. Acad. Exch. Conf. Sci. Technol. Innov. (IAECST) **2023**, 819–823. https://api.semanticscholar.org/CorpusID:269388357

[7] Bhandari, G.; Gangola, S.; Dhasmana, A.; Rajput, V.; Gupta, S.; Malik, S.; Slama, P. Front. Microbiol. **2023**, 14, 1214870. https://doi.org/10.3389/fmicb.2023.1214870

Acknowledgements

Authors thank LMA (IF-UNAM) and LANEM (CIQ-UAEM) for access to the facilities and characterization. They also extend their gratitude for technical support to Cristina Zorrilla Cangas, Perla Román Bravo, Diana Gabriela Vargas Pineda and Paola Sánchez Portillo.

Polymat Contributions

Crystalline cellulose extraction from single-use cups: structural analysis through infrared and x-ray diffraction methods

Erick Habacuc Reyes Piña[1], Mayra Elizabeth Juárez Méndez[1], Diana Palma Ramírez[1*]

*[1]Instituto Politécnico Nacional, Unidad Profesional Interdisciplinaria de Ingeniería Campus Hidalgo (UPIIH), Pachuca 42162, México, *dpalmar@ipn.mx*

Abstract

This work focuses on processing cellulose extracted from single-use beverage cups. The material was bleached with H_2O_2 and NaOH under constant stirring for 24 h, followed by acid hydrolysis with 64% H_2SO_4 to obtain crystalline cellulose. The process was monitored using Fourier transform infrared (FTIR) spectroscopy and X-ray diffraction (XRD). FTIR results showed decreased transmittance after bleaching and removal of amorphous components, indicating the reduction of extractives such as hemicellulose, lignin, and amorphous cellulose. Signals corresponding to C–C, C–OH, CH, and C=O groups were identified, with the C=O band decreasing in intensity after treatment. XRD analysis revealed strong reflections at 2θ ≈ 15° and 22°, associated with the (101) and (102) planes of cellulose type II. Overall, the methods confirmed the successful extraction of crystalline cellulose suitable for future dispersion in interpenetrating polymer networks to enhance mechanical properties.

Introduction

The automotive industry is continuously seeking materials that meet the demands of the current market, which is increasingly aware of environmental impact. Consequently, priority is given to the use of sustainable materials that not only reduce ecological impact but also generate high performance under various testing conditions [1-3]. The combination of engineering polymers such as poly(methyl methacrylate) (PMMA) and poly(urethane) (PU), reinforced with crystalline nanocellulose (CNC) (Figure 1), could offer an efficient and environmentally low-impact alternative for automotive applications, such as headlights, as it integrates superior mechanical and optical properties [4].

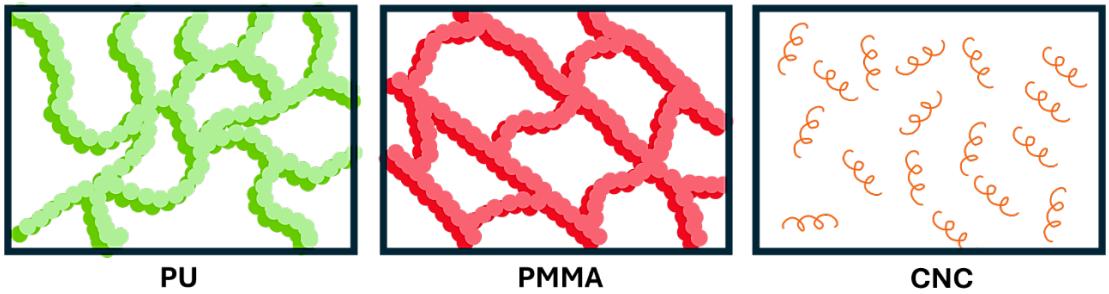

Figure 1. Representation of the polymer structure.

To take advantage of the properties of each selected polymer, the physical combination of the materials is carried out, avoiding the formation of covalent bonds between them, through interpenetrating polymer networks (IPNs). However, cellulose extraction needs to be studied before being proposed for those polymeric systems, since the synergistic properties will depend on the final extracted type of polymorph. Cellulose can impart stiffness, mechanical resistance, and transparency to some extent, whereas the PMMA and PU can impart stiffness

as well and toughness, respectively [5]. Therefore, the main purpose of this work is to study the extraction from single-use cups employing a green method and hydrolysis acid to remove amorphous regions, and the study of structural features using Fourier transform infrared (FTIR) spectroscopy and X-ray diffraction (XRD).

Materials and methods

The chemical reagents used for cellulose extraction and characterization are the following: hydrogen peroxide (J.T. Baker, 80%), sodium hydroxide (J.T. Baker, 98%), absolute ethanol (J.T. Baker, 99.5%), and sulfuric acid (Wöhler, 95–98%).

Metodology

The fiber extracted from the recycling of disposable cups contains adhesives and pigments that must be removed to obtain CNC. Using a Soxhlet extractor with a suitable solvent (in this case, ethanol), the solvent was heated at 100 °C for 4-h cycles, dissolving and removing the pigments and adhesives from the paper. The condensed ethanol drips back onto the sample, carrying away the contaminants until the liquid becomes saturated and is discharged through the siphon. The cleaned fiber is treated with a mixture of hydrogen peroxide (H_2O_2, 10% v/v) and sodium hydroxide (NaOH, 10% w/v) to remove residual lignin and hemicellulose that contribute to coloration. The mixture is stirred for 24 h, then filtered and allowed to dry. This process lightens the fiber, yielding a purer and whiter cellulose suitable for subsequent processing. The bleached cellulose is then subjected to hydrolysis with sulfuric acid (64% v/v) at 45 °C for 45 min (Figure 2), which removes the amorphous regions while preserving the crystalline domains. Then, the solids are precipitated through centrifugation, and the liquid is decanted into a waste collector for subsequent treatment. Once the sample is completely dried, it is processed using a FOSS CT-293 Cyclotec mill to reduce the CNC particle size and facilitate the homogeneous incorporation into the polymers, thereby achieving improved dispersion.

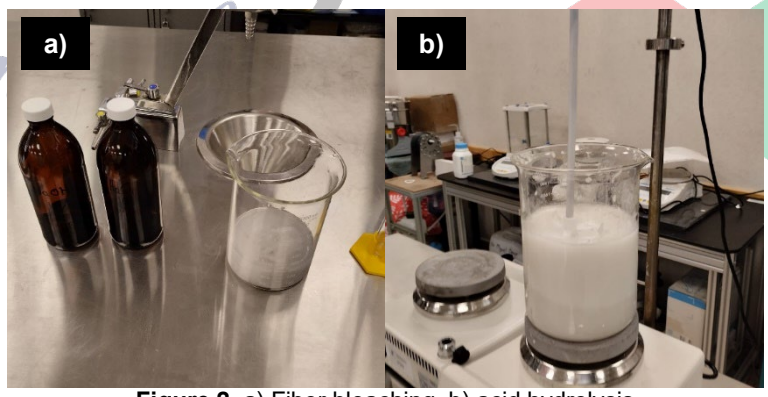

Figure 2. a) Fiber bleaching, b) acid hydrolysis

Results and discussion

The X-ray patterns of the samples corresponding to the cup fiber, the bleached cellulose, and the CNC extracted from single-use cups are presented in Figure 3. Signals are detected at 14.76°, 16.38°, 22.3°, and 33.96° (2θ), which are associated with the crystallographic planes ($1\bar{1}0$), (110), (200), and (023). These signals correspond to type Iβ cellulose with a monoclinic structure, according to crystallographic cards PDF #00-056-1717, PDF #00-056-1718, and PDF #00-056-1719. It is observed that the diffraction patterns obtained after bleaching and acid hydrolysis are very similar.

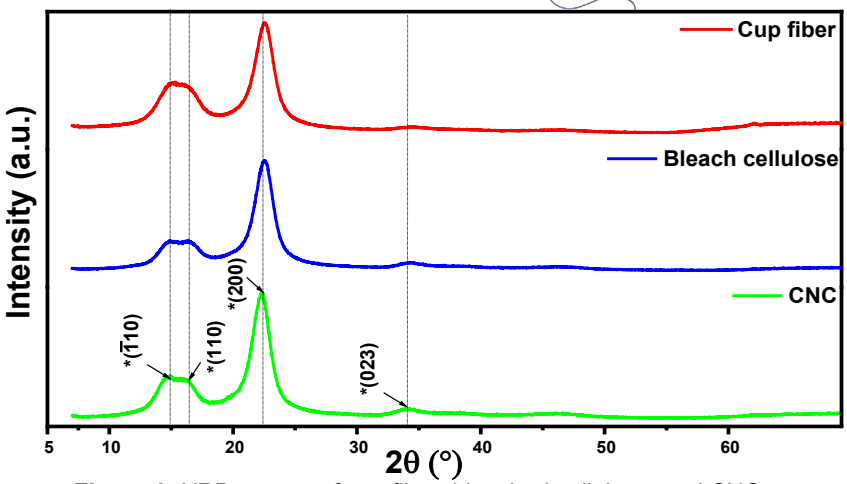

Figure 3. XRD pattern of cup fiber, bleached cellulose, and CNC.

The samples of fiber were analyzed using a Bruker ALPHA II spectrometer, with a spectral range of 350–8000 cm^{-1} and a spectral resolution of 2 cm^{-1}, equipped with a monolithic diamond crystal for ATR measurements. Based on the detected signals (Figure 4), the functional groups were identified as follows: the band at 3335 cm^{-1} corresponds to the stretching of hydroxyl groups (OH), the band at 2960 cm^{-1} to the symmetric stretching of the CH_3 group, and the signal at 2900 cm^{-1} to the asymmetric stretching of the CH_2 group. In the fingerprint region, a confirmation signal for OH groups appears at 1640 cm^{-1}, associated with adsorbed water. The CH_2 and CH groups are observed at 1428 and 1373 cm^{-1}, respectively. The stretching of CO groups appears at 1033 cm^{-1}, while the asymmetric stretching of the COC group is detected at 814 cm^{-1}. Finally, the out-of-plane bending of the COH group is identified at 705 cm^{-1}[2-10].

Table 1. FT-IR assignments of processed fiber.

Signal (cm^{-1})	Assignment
3335	OH stretching
2960	Symmetric stretching of CH_3
2900	Asymmetric stretching of CH_2
1640	OH bending
1428, 1373	Bending of CH_2 and CH
1033	CO stretching
705	COH out-of-plane bending

Conclusions

XRD and FT-IR analyses confirm that the chemical treatments applied during CNC extraction effectively removed amorphous components without altering the fundamental cellulose structure. FT-IR spectra showed the preservation of characteristic functional groups associated with cellulose, alongside the reduction of signals related to lignin, hemicellulose, and other extractives. Complementarily, XRD patterns revealed well-defined reflections corresponding to cellulose polymorphs I-α, I-β, and II, indicating an intermediate degree of crystallinity. Together, these results validate the successful isolation of crystalline cellulose while maintaining its structural integrity throughout the processing stages.

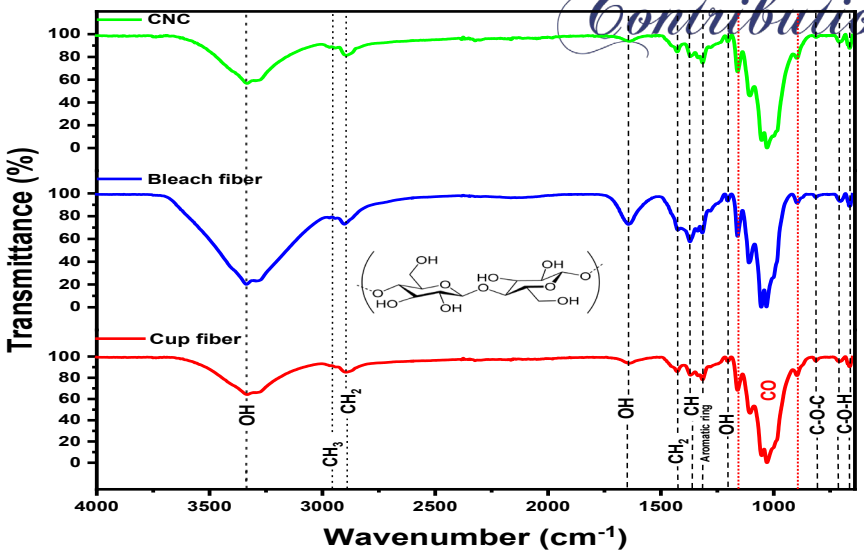

Figure 4. FT-IR spectra of cup fiber, bleach fiber and CNC.

References

[1] X. Guo, Z. Jiang, H. Li, W. Li, Production of recycled cellulose fibers from waste paper via ultrasonic wave processing, 132 (2015).

[2] X. Guo, L. Liu, J. Wu, J. Fan, Y. Wu, Qualitatively and quantitatively characterizing water adsorption of a cellulose nanofiber film using micro-FTIR spectroscopy, RSC Advances 8 (2018) 4214-4220.

[3] B.M. Marim, J. Mantovan, G.A.G. Giraldo, S. Mali, Environmentally friendly process based on a combination of ultrasound and peracetic acid treatment to obtain cellulose from orange bagasse, Journal of Chemical Technology & Biotechnology 96 (2021) 630-638.

[4] S.A. Begum, A.V. Rane, K. Kanny, Chapter 20 - Applications of compatibilized polymer blends in automobile industry, in: A. A.R, S. Thomas (Eds.), Compatibilization of Polymer Blends, Elsevier2020, pp. 563-593.

[5] B. Mahendiran, S. Muthusamy, R. Selvakumar, N. Rajeswaran, S. Sampath, S.N. Jaisankar, G.S. Krishnakumar, Decellularized natural 3D cellulose scaffold derived from Borassus flabellifer (Linn.) as extracellular matrix for tissue engineering applications, Carbohydrate Polymers 272 (2021) 118494.

[6] H. Hamad, E. Bailón-García, S. Morales-Torres, F. Carrasco-Marín, A.F. Pérez-Cadenas, F.J. Maldonado-Hódar, Physicochemical properties of new cellulose-TiO2 composites for the removal of water pollutants: Developing specific interactions and performances by cellulose functionalization, Journal of Environmental Chemical Engineering 6 (2018) 5032-5041.

[7] I. Dávila, J. Remón, P. Gullón, J. Labidi, V. Budarin, Production and characterization of lignin and cellulose fractions obtained from pretreated vine shoots by microwave assisted alkali treatment, Bioresource Technology 289 (2019) 121726.

[8] D. Matykiewicz, M. Barczewski, O. Mysiukiewicz, K. Skórczewska, Comparison of Various Chemical Treatments Efficiency in Relation to the Properties of Flax, Hemp Fibers and Cotton trichomes, Journal of Natural Fibers 18 (2021) 735-751.

[9] K. Jungnikl, O. Paris, P. Fratzl, I. Burgert, The implication of chemical extraction treatments on the cell wall nanostructure of softwood, Cellulose 15 (2008) 407-418.

[10] Y. Tong, S. Huang, X. Meng, Y. Wang, Aqueous-Cellulose-Solvent-Derived Changes in Cellulose Nanocrystal Structure and Reinforcing Effects, Polymers, 2023.

Acknowledgements

The authors are grateful to CNMN IPN for carrying out the tests and to the Secretaría de Investigación y Posgrado (SIP) of IPN through the SIP20251064 project, as well as SNII-SECIHTI.

POLYSACCHARIDE/CHITOSAN pH-RESPONSIVE NANOGELS AS EFFICIENT NANOCARRIERS FOR DOXORUBICIN HYDROCHLORIDE LOADING AND CONTROLLED RELEASE

Daniela Eunice ROMERO HERNÁNDEZ[1], Karla Gricelda FERNANDEZ-SOLIS[2,3], Guillermo TORIZ[4], Eduardo MENDIZABAL MIJARES[3], Julien ROSSELGONG[2], Alberto GUTIERREZ-BECERRA[1], Edgar B. FIGUEROA OCHOA[3], Lourdes Mónica BRAVO ANAYA[2]*

[1] Departamento de Ciencias Básicas, CUTonalá, Universidad de Guadalajara, México.
[2] Institut des Sciences Chimiques de Rennes, Université de Rennes, Rennes, France
[3] Departamento de Química, Universidad de Guadalajara, México
[4] Universidad de Guadalajara, Departamento de Madera, Celulosa y Papel, Zapopan, Jalisco, México.
daniela.romero5832@alumnos.udg.mx, *lourdes-monica.anaya@univ-rennes.fr***

Abstract

Nanogels are nanometric-sized hydrogels formed by physically or chemically cross-linked polymer chains, giving rise to a three-dimensional (3D) network with high water absorption capacity. The potential application of biocompatible polysaccharide/chitosan nanogels as nanocarriers of the antineoplastic drug doxorubicin hydrochloride (DOXO-HCl) is presented in this study. Chitosan and either oxidized maltodextrin or oxidized methylcellulose were crosslinked through a reductive amination reaction to synthesize pH-responsive nanogels. Then, high concentrations of doxorubicin hydrochloride (DOXO-HCl) were encapsulated in both type of nanogels. The release kinetic profile was studied at different pH: a) 5.5, simulating the acidity of the extracellular environment in cancerous tumors, b) 7.4, representing the pH of the bloodstream, and c) 9, in order to compare the results with those in a basic medium. The release profile for both type of nanogels was studied at 37 °C and was analyzed using the Higuchi, Korsmeyer-Peppas, and Peppas-Sahlin diffusion models. Loading efficiencies between 55 and 75% were obtained for maltodextrin/chitosan nanogels, whereas efficiencies between 90 and 100% were reached for methylcellulose/chitosan nanogels, showing that the structure of polysaccharides can impact the encapsulation ability of nanogels. It was also found that the model that best fits the experimental data was the Korsmeyer-Peppas one. The total diffusion of DOXO-HCl into the medium at pH 7.4 and 5.5 was reached at 120 and 80 minutes, respectively, for maltodextrin/chitosan nanogels, while for the basic medium of pH of 9 there was a release of 60% after 25 hours, confirming the pH responsiveness of the nanogels. Hence, the acidity of the medium was associated with an accelerated diffusion of the drug.

Introduction

Cancer is a genetic disease associated with alterations in cellular processes, particularly accelerated mitosis and reduced apoptosis, which frequently lead to the formation of malignant tumors capable of modifying the extracellular environment and spreading throughout the body via metastasis. Conventional treatments such as chemotherapy and radiotherapy remain essential but are often imprecise, generating collateral effects on healthy tissues surrounding

the cancerous cells. To address these limitations, nanoscale drug-delivery systems have been developed to deliver therapeutic agents to specific sites using smaller doses while improving overall treatment efficiency [1].

Among these systems, nanogels, nanoscale hydrogel particles composed of cross-linked polymer networks, have gained significant attention [1]. They are characterized by their biocompatibility, high absorption capacity and stability in aqueous media. Notably, nanogels respond to external stimuli, adjusting their volume by swelling or contracting when they are exposed to changes in temperature, pH or redox conditions [2]. This stimulus sensitivity makes them promising candidates for the encapsulation and controlled release of chemotherapeutic drugs, allowing more localized drug delivery, improving treatment efficiency, reducing the required dosage and minimizing adverse side effects.

In this study, pH-responsive nanogels were synthetized using biocompatible, biodegradable, and non-toxic polymers: chitosan (CS), maltodextrin (MD) and methylcellulose (MC). Chitosan and either oxidized maltodextrin or oxidized methylcellulose were cross-linked through a reductive amination reaction, yielding two types of nanogels with distinct structural characteristics. High concentrations of doxorubicin hydrochloride (DOXO-HCl) were then encapsulated in both nanogel systems to study their performance as drug-delivery platforms. To assess their release behavior, the kinetic profiles were studied at pH 5.5 (simulating the acidic extracellular environment of cancerous tumors), pH 7.4 (representing physiological blood pH), and pH 9 (to compare with a basic medium), all at 37 °C. The release data for both nanogels were analyzed using the Higuchi, Korsmeyer-Peppas, and Peppas-Sahlin diffusion models to identify the mechanisms governing DOXO-HCl transport and evaluate how intrinsic nanogel properties influence encapsulation efficiency and drug-release kinetics.

Experimental methodology

Three chitosan (CS) samples with different molecular weights (MW) and degrees of acetylation (DA): LMW (Mw = 38.4 kg/mol, DA = 0.33), MMW (Mw = 86 750 g/mol, DA = 0.22), and HMW (Mw = 417 600 g/mol, DA = 0.16), were purchased from Sigma-Aldrich. MD (DE = 16.5-19.5) and MC were also obtained from Sigma-Aldrich, and their MWs were determined by SEC. Sodium periodate, ethylene glycol, sodium cyanoborohydride ($NaBH_3CN$), n-butylamine, sodium acetate, glacial acetic acid, hydrochloric acid and NaOH were used without further purification. Oxidized polysaccharides and nanogels were purified with regenerated cellulose dialysis membranes (MWCO 3.5 kDa). For DOXO-HCl encapsulation and release studies, the materials used included DOXO-HCl powder, phosphate-buffer components (Na_2HPO_4, KH_2PO_4), HCl (38%), ethanol (96%), and a DOXO-HCl solution (2 mg/mL).

MD and MC were partially oxidized with sodium periodate to generate aldehyde groups, then purified by dialysis and lyophilized [3]. Oxidation was confirmed by FTIR and ^1H NMR and quantified via potentiometric titration with hydroxylamine hydrochloride. The oxidized polysaccharides were crosslinked with chitosan (CS) through reductive amination using sodium cyanoborohydride at controlled CS concentrations and pH (3.5 or 5.5). The resulting MD/CS and MC/CS nanogels were purified by dialysis to remove unreacted reagents and then characterized in terms of size, polydispersity, and surface charge by Dynamic Light Scattering

(DLS) and ζ-potential measurements, with morphology examined by Scanning Electron Microscopy (SEM).
The MD/CS and MC/CS nanogels were loaded with high concentrations DOXO-HCl. Five solutions were prepared for each system, with DOXO-HCl concentrations from 800 to 1600 ppm, and stirred gently at 60 rpm overnight to promote drug incorporation. Samples were then centrifuged three times for 15 minutes at 3000 rpm to remove unencapsulated drug. The supernatants were analyzed by DLS to determine their hydrodynamic diameter and by UV-Vis spectroscopy for encapsulation efficiency. Release kinetics were evaluated in PBS at pH 5.5, 7.4, and 9, using 300 µL of nanogel suspension in dialysis membranes immersed in 80 mL of buffer at 37 °C under continuous stirring. Aliquots were collected from 1 minute to 8 hours and analyzed by UV-Vis spectroscopy, and the release profiles were fitted to the Higuchi, Korsmeyer-Peppas, and Peppas-Sahlin models [5].

Results and discussion

The amount of encapsulated DOXO-HCl, expressed in ppm, was plotted against the initial drug concentration for two nanogels prepared with MD and two with MC. The concentrations were determined by UV-Vis spectroscopy after 1:20 dilution, using absorbance at 480 nm and a calibration curve. As shown in **Figure 1**, the relationship was linear and increasing, indicating that the nanogels did not reach saturation within the tested concentration range. Encapsulation efficiencies ranged from 66% to 87%, with methylcellulose-based nanogels exhibiting the highest values, exceeding 80% in some cases.

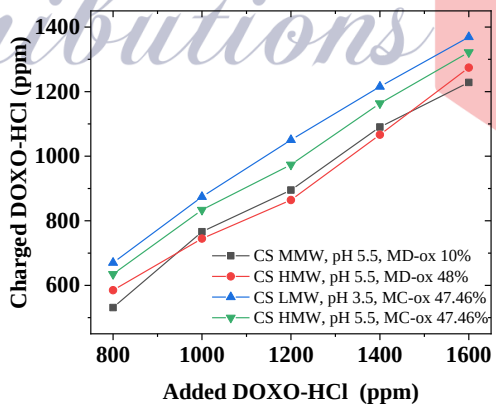

***Figure 1**. Evolution of the charged DOXO-HCl concentration as a function of the initially added DOXO-HCl concentration for the nanogels: CS/MMW, pH 5.5, ox-MD 10 %, black; CS/HMW, pH 5.5, ox-MD 48 % red; CS/LMW, pH 3.5, ox-MD 47.5 %, blue, CS/HMW, pH 5.5, ox-MD 47.5 %, green. The dotted line is included as a visual guide.*

The nanogels loaded with DOXO-HCl showed a clear increase in particle size compared with the unloaded nanogels. The percentage of swelling ranged from 90 % to 137 % for methylcellulose-based nanogels, whereas the maltodextrin-based nanogels exhibited less swelling with approximately 70 %.

The drug release assays demonstrated the important impact of pH on the release behavior of DOXO-HCl from the nanogels. Nanogels evaluated in PBS media at pH 7.4 and 9 exhibited greater drug retention, resulting in prolonged release times, compared with those tested under acidic conditions (pH 5.5). Nanogels synthesized with MC displayed slower release kinetics than those with MD across the 3 studied pH. For the pH of 9, there was a release of 60 % after 25 hours. The Korsmeyer–Peppas model provided the best fit for the release profiles of both MD/CS and MC/CS nanogels, with $R^2 > 0.97$, for all three pH values tested (5.5, 7.4, and 9).

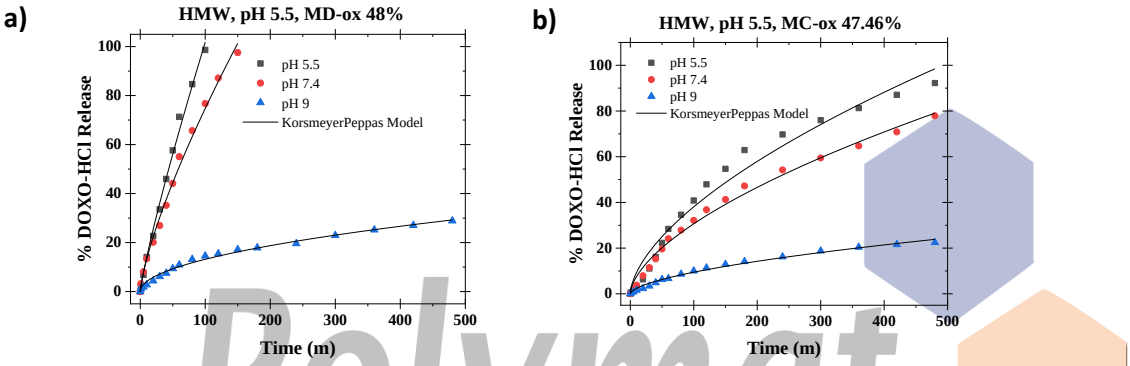

Figure 2. *Release kinetics of DOXO-HCl from nanogels in PBS at pH 5.5, 7.4, and 9: a) CS HMW (0.4 mg/mL), pH 5.5, ox-MD 48%; b) CS HMW (0.4 mg/mL), pH 5.5, ox-MC 47.46%.*

Conclusions

MD/CS and MC/CS nanogels are promising for controlled drug release due to their high encapsulation efficiency and pH-responsive behavior. Both systems achieved encapsulation efficiencies above 65%, even at high drug concentrations, and drug loading increased hydrodynamic diameter by 60-137%. Release studies confirmed pH sensitivity, with faster drug release under acidic conditions (pH 5.5) compared to neutral (pH 7.4) and basic (pH 9) media. Methylcellulose-based nanogels showed greater drug encapsulation, and the release kinetics were well described by the Korsmeyer–Peppas model, indicating diffusion-controlled release.

References

[1] Sabir, F.; Asad, M. I.; Qindell, M.; Afzal, I,; Junaid Dar, M.; Shah, K.U.; Zeb,A.; Khan, G.M.; Ahmed, N.; Din, F; *J. Nanomater.* **2019**, 1526186.
[2] Ekkelenkamp, A.E.; Elzes, M.R.; Engbersen, J.F.J.; Paulusse, J.M.J., *J. Mater. Chem. B* **2018**, 6, 210-235.
[3] Fernández-Solís, K.G.; Domínguez-Fonseca, E.; González-Martínez, B.M.; Gutiérrez-Becerra, A.; Figueroa-Ochoa, E. B.; Mendizábal, E.; Toriz, G.; Loyer, P.; Rosselgong, J.; Bravo-Anaya, L.M. *Int. J. Biol. Macromol.* **2024**, 274, 133277.
[4] Rinaudo, M. *Eur. Polym. J.* **2010**, 46, 1537-1544.
[5] Gutiérrez-Saucedo, R.A.; Gómez-López, J.C.; Villanueva-Briseño, A.A.; Topete, A.; Soltero-Martínez, J.F.A.; Mendizábal, E.; Jasso-Gastinel, C.F.; Taboada, P.; Figueroa-Ochoa, E.B. *Polymers* 2023, 15, 1-19.

Acknowledgements

D.E. Romero-Hernández acknowledges the guidance and support of Dr. Bernjamín Figueroa, Dra. Monica Bravo Anaya, Dr. Alberto Gutierrez and Mtra. Karla Fernandez throughout the development of this project. Acknowlegements are also extended to the University of Guadalajara for providing access to its facilities, as well as to the P²NanoBio project funded by CNRS to support the collaboration between Mexico and France.

PREDICTABILITY OF CALCULATIONS ON HIGH ENTROPY ALLOYS FOR HYDROGEN STORAGE: AN EXPERIMENTAL RECREATION OF $Mg_{0.10}Ti_{0.30}V_{0.25}Zr_{0.10}Nb_{0.25}$

K. Suarez-Alcantara[1], E.D. Ruiz-Santacruz[1], N.L. Torres-Garcia[1]

[1] *Morelia Unit of Materials Institute Research, National Autonomous University of Mexico,*
karina_suarez@materiales.unam.mx

High entropy alloys (HEAs) can play a role as hydrogen storage materials. However, due to the almost infinite number of combinations of elements and possible stoichiometries, one-by-one HEA processing and testing is unpracticable. Thus, calculations predicting the formation and hydrogen storage capability are highly recommended. DFT calculations are recommendable but computationally expensive. Because of that, a relatively low amount of DFT-based papers among the great number of published reports on HEAs can be located. Deng et al., in a recent paper, indicated that the high entropy alloy $Mg_{0.10}Ti_{0.30}V_{0.25}Zr_{0.10}Nb_{0.25}$ would have a hydrogen storage capacity of 3.16 wt%. Such predicted high hydrogen storage capacity deserved experimental confirmation. Thus, we prepared $Mg_{0.10}Ti_{0.30}V_{0.25}Zr_{0.10}Nb_{0.25}$ from the mechanical milling of the elements and characterized it for hydrogen storage. The maximum experimental hydrogen storage at 25 bar hydrogen pressure and 300°C was 1.2 wt% in the first cycle decreasing in the following ones. The material presented reversibility but was limited to only about 0.9 wt%. We conclude that the DFT predictability is not completely experimental fulfilled.

Introduction

High entropy alloys (HEAs) are highly promising candidates for hydrogen storage due to the ability to tailor their properties by precisely selecting the constituent elements and stoichiometry. However, since HEAs are relatively new in this field, and the vast number of potential element combinations can easily scale into millions, clear guidelines are urgently needed for selecting optimal compositions. For HEAs to be practical hydrogen storage materials, two conditions must be met: a) the alloy must be easily synthesized using common production techniques like fusion or mechanical milling, and b) the resulting HEA must store an acceptable amount of hydrogen under the mildest possible temperature and pressure conditions, ideally meeting the demanding DOE technical targets.

Regarding the first condition, traditional guidelines like the Hume-Rothery rules are not definitive, especially for Mg-containing HEAs, given the unique characteristics of Mg compared to transition metals. More advanced predictive tools are necessary. CALPHAD (CALculation of PHAse Diagrams) methods, for instance, can be useful in predicting the formation of a single-phase HEA over the formation of competing intermetallics or binary/ternary solid solutions.

Once the HEA is formed, its hydrogen storage performance is determined by the reversibility and temperature of the dehydriding reaction. The equilibrium pressure (P_{eq}) and, consequently, the dehydriding temperature (T) are classically related to the hydride formation enthalpy (ΔH) via the Van't Hoff equation:

$$ln\left(\frac{P_{eq}}{P_{eq}^{0}}\right) = \frac{\Delta H}{RT} - \frac{\Delta S}{R} \quad (1)$$

Since the hydride formation enthalpy is often unknown for complex HEAs, researchers have sought other predictive parameters. The Valence Electron Concentration (VEC) is a useful descriptor, not only for predicting the favored crystal structure (e.g. BCC for VEC < 6.87 and FCC for VEC ≥ 8) but also for estimating the dehydriding temperature, as recently reported by Nygård et al.
The presence of Ti, V, and Zr is common in HEAs developed for hydrogen storage, demonstrating diverse storage capacities and operating conditions (e.g. 2.6 wt%, 25 bar, 25°C). This work focuses on an Mg-containing HEA ($Mg_{0.10}Ti_{0.30}V_{0.25}Zr_{0.10}Nb_{0.25}$), though its Mg content is intentionally lower than that found in other high-capacity Mg-HEAs. The objective is to investigate the formation and hydrogenation behavior if this specific composition to further refine the guidelines for the future HEA design.

Methodology

All raw materials were used as received; they were Mg (Alfa-Aesar, -325 mesh, 99% purity), Ti, V, Zr and Nb powders (Sigma-Aldrich, -300 mesh, 99% purity). Stoichiometric quantities required to prepare 2 g of a $Mg_{0.1}Ti_{0.3}V_{0.25}Zr_{0.1}Nb_{0.25}$ material were calculated according to the procedure reported. The elemental powders were introduced into a stainless-steel milling vial along with six yttria-stabilized zirconia balls with a 1 cm diameter. All material storage, handling, and preparation processes were performed in an inert argon gas atmosphere within a Vigor® glovebox (with O_2 and H_2O levels below 5 ppm). Subsequently, the milling vial was transferred to a shaker-type mill (cryogenic Retsch®) at room temperature. The mill was programmed for milling cycles of 30 min with a shaking frequency of 30 Hz and rest periods of 10 min between each cycle, until a total milling time of 20 hours was completed. The temperature-programmed hydrogenation (TPH) and temperature-programmed dehydrogenation (TPD) experiments were carried out in an in-house designed and constructed Sieverts-type apparatus. 0.3 g of each sample was transferred to the Sieverts-type reactor without oxygen contact using a sample holder with an isolation valve. The full material testing involved calibration, activation, and hydriding/dehydriding cycling. Activation was achieved by heating the materials in a vacuum at 350°C for 3 h, followed by successive hydriding and dehydriding reactions. For hydriding, hydrogen was introduced at 20 bar and the sample was heated from room temperature to 300°C at 5°C/min. The reactor was then cooled, and pressure was released. For dehydriding, the hydrogen pressure was initially 0.015 bar, and the sample was heated to 350°C at 5°C/min. Complete hydrogen release was ensured by applying a dynamic vacuum for 30 min at 350°C before cooling to room temperature for the next cycle. Finally, XRD and SEM characterization was performed on the hydrided materials. Pressure-Composition Isothermal (PCI) curves were obtained using a Quantachrome® Isorb-100 instrument. Approximately 0.150 g of the as-milled materials were transferred to the instrument without air contact using a sample holder with an isolation valve. For activation, the materials were heated at 350°C for 3 h under a dynamic vacuum. Void volume calibration was performed with ultrahigh-purity helium. In isothermal conditions, the pressure was gradually increased and decreased stepwise from 0.01 to 15 bar and vice versa. Equilibrium conditions for each step were assumed when the recorded pressure varied by less than 0.1 x 10^{-3} bar over 30 min, or after a maximum duration of 120 min.

Results

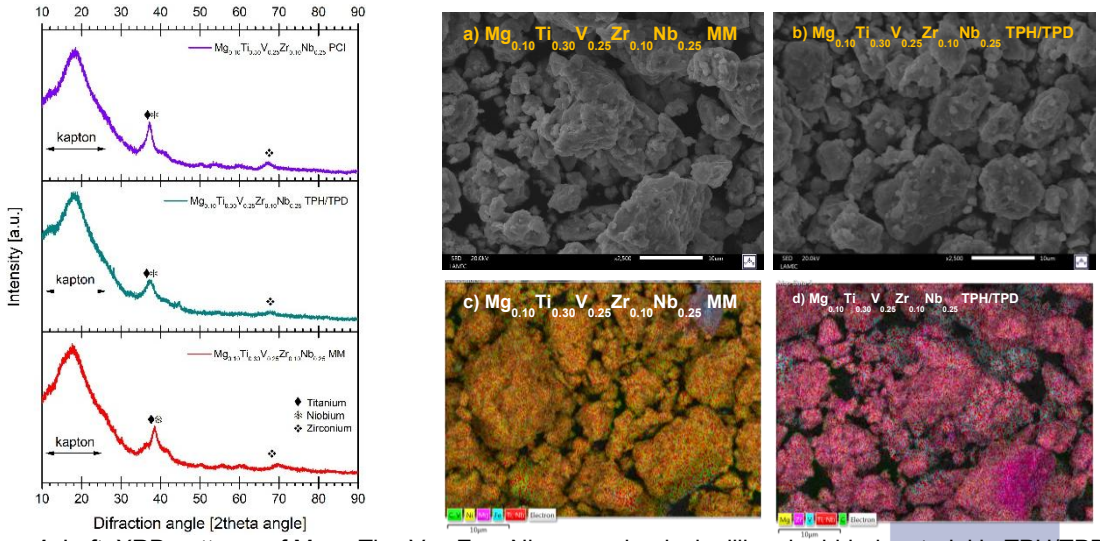

Figure 1. Left: XRD patterns of $Mg_{0.10}Ti_{0.30}V_{0.25}Zr_{0.10}Nb_{0.25}$ mechanical milling, hydrided material in TPH/TPD and PCI. Right: SEM images of this material; top of the morphological view of the material, bottom EDS analyses of these materials

Figure 1-Left shows the X-ray diffraction (XRD) patterns of the $Mg_{0.10}Ti_{0.30}V_{0.25}Zr_{0.10}Nb_{0.25}$ alloy synthesized by three different methods (PCI, TPH/TPD, and MM). All samples display a broad diffuse halo between ~15–35° (2θ), attributed to the Kapton film used during measurement, indicating the predominantly amorphous nature of the alloys. Superimposed on this halo, small crystalline reflections are observed, corresponding to elemental phases of Ti (◆), Nb (❄), and Zr (❖).

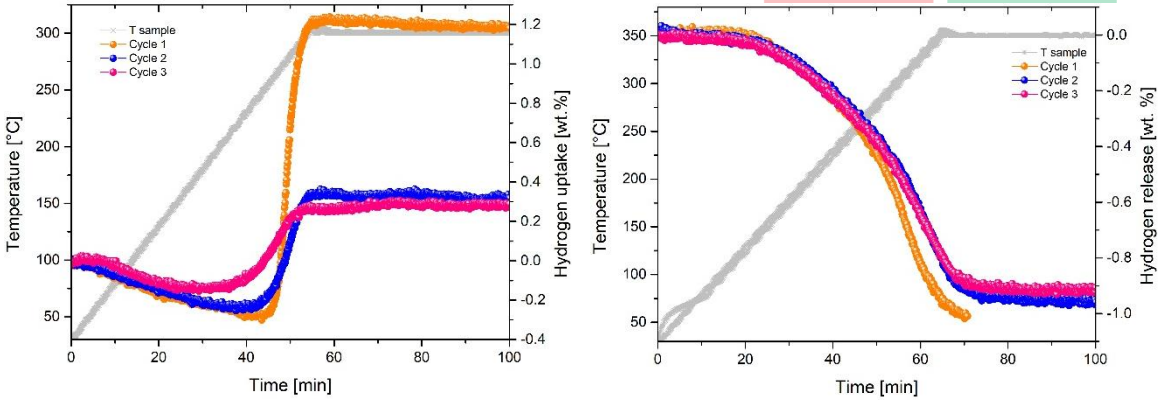

Figure 2. Hydriding and dehydriding reactions with 3 cycles to evaluate reversibility.

On the flip side it shows SEM micrographs (top) and corresponding EDS elemental mapping (bottom) of the $Mg_{0.10}Ti_{0.30}V_{0.25}Zr_{0.10}Nb_{0.25}$ alloys prepared by mechanical milling (MM) and by the TPH/TPD process. The SEM images reveal agglomerated particles with irregular and micrometer-sized morphologies in both synthesis routes. The EDS maps demonstrate a homogeneous distribution of Mg, Ti, V, Zr, and Nb throughout the particles, confirming the chemical uniformity of the multicomponent alloy.

On the other hand, the reaction kinetics are shown in Figure 2, where the experimental capacity of the material is observed to be 1.2–0.3 wt%. Three hydriding/dehydriding cycles were performed to evaluate its reversibility. A difference is evident between hydriding and dehydration, due to the pressurized cooling step in hydriding, which suggests that it continues to absorb moisture.

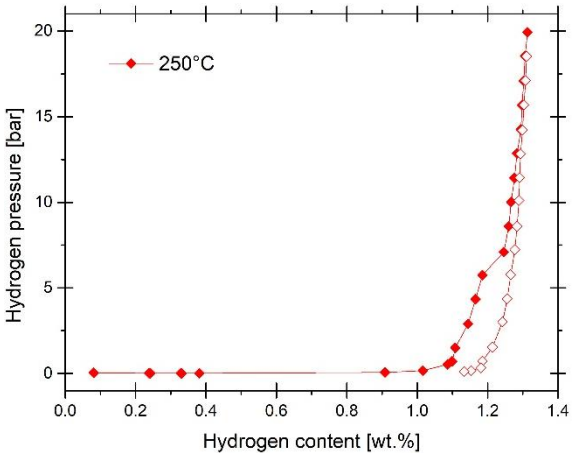

Figure 3. Pression-composition isotherms of the $Mg_{0.10}Ti_{0.30}V_{0.25}Zr_{0.10}Nb_{0.25}$ alloy 250°C

Next image (Figure 3) shows the PCI curve of the prepared material. The shape of the curve indicates the ease of hydriding re and the difficulty of the dehydration reaction for this material. The dehydration reaction could be limited by the stability of the obtained nanoparticles and the integration of the proposed metals into this alloy.

Conclusions

The experimental evaluation of the $Mg_{0.10}Ti_{0.30}V_{0.25}Zr_{0.10}Nb_{0.25}$ high-entropy alloy revealed that its hydrogen storage performance does not fully match the DFT-predicted capacity. Although the alloy was successfully synthesized by mechanical milling and exhibited chemical homogeneity at the microscale, the maximum hydrogen uptake reached only ~1.2wt% during the first hydriding cycle at 300°C and 25 bar, decreasing to ~0.9wt% upon subsequent cycling. XRD analysis indicated predominantly amorphous structures with minor elemental crystalline phases, while SEM/EDS confirmed uniform elemental distribution. Overall, the results demonstrate that DFT predictions may overestimate the practical storage capacity of Mg-containing HEAs, highlighting the need for improved computational descriptors and experimentally validated guidelines for future HEA design aimed at hydrogen storage applications.

Acknowledgements

This research was funded by CONAHCYT-CIENCIA DE FRONTERA CF-2023-I-394 Aleaciones de alta entropía con V o Mg para el almacenamiento de hidrógeno. N.L. Torres-Garcia acknowledges SECIHTI for the postdoctoral fellowship under the academic modality of the program “Estancias Posdoctorales por México 2022 (3) – Renovación”.

References

[1] Deng Y, Hu J, Zhao S, Wang W, Xie L, Sun G, et al. Hydrogen storage properties of $Mg_{0.10}Ti_{0.30}V_{0.25}Zr_{0.10}Nb_{0.25}$ lightweight high entropy alloy: A theoretical study. Int J Hydrogen Energy 2024; 50:314–23. https://doi.org/10.1016/j.ijhydene.2023.07.075.

[2] Nygård MM, Ek G, Karlsson D, Sørby MH, Sahlberg M, Hauback BC. Counting electrons - A new approach to tailor the hydrogen sorption properties of high-entropy alloys. Acta Mater 2019;175:121–9. https://doi.org/10.1016/j.actamat.2019.06.002.

[3] Kumar A, Yadav TP, Mukhopadhyay NK. Notable hydrogen storage in Ti–Zr–V–Cr–Ni high entropy alloy. Int J Hydrogen Energy 2022;47:22893–900. https://doi.org/10.1016/j.ijhydene.2022.05.107.

[4] Carrillo-Bucio J.L., Tena-Garcia J.R., Armenta-Garcia E.P., Hernandez-Silva O., Cabañas-Moreno J.G., Suarez-Alcantara K. Low-cost Sieverts-type appartus for the study of hydriding/dehydriding reactions. HardwareX 2018; 4 e00036. https://doi.org/10.1016/j.ohx.2018.e00036

EVALUATION OF ACTIVATED BIOCHAR FOR METHYLENE BLUE ADSORPTION

Elvia Terán-Salgado[1*], Carolina Godoy-Alcantar[1], María L. Garcia-Betancourt[1]

[1] Centro de Investigaciones Químicas, IICBA, Universidad Autónoma del Estado de Morelos, Av. Universidad 1001, Col. Chamilpa, C.P. 62209 Cuernavaca, Morelos, México.
**elvia.teran@uaem.mx*

Abstract

Activated carbon (AC) plays a key role in applications related to energy storage and generation, environmental remediation, water purification, among others; due to the high porosity present in its structure [1]. This extraordinary material is made up of layers of carbon in an irregular shape with spaces between the layers that constitute its porosity. A series of organic wastes used as carbon-rich precursors have been reported, such as wood, coconut shells, olive stones, and agricultural residues, among others [2]. Dyes are a group of contaminants with a high degree of toxicity, affecting biodiversity and even decomposing into carcinogenic compounds [3]. Methylene blue is an organic compound, it belongs to the group of basic dyes, used mainly in the textile industry, in medicine, and biology [4]. In this work, the synthesis of carbon through the pyrolysis process of an organic waste is presented. Subsequently, chemical activation of the biochar was carried out using acids to promote a porous surface. In addition, the performance of activated carbon as an adsorbent for methylene blue dyes with a high degree of toxicity, was studied. The produced carbonaceous materials were characterized using scanning electron microscopy (SEM), Raman spectroscopy, Fourier transform infrared spectroscopy (FTIR) and elemental analysis to determine their morphology, chemical composition.

Introduction

Biomass is a term used to describe plant-derived materials and organic waste that can serve as renewable energy sources. It can originate from various feedstocks, and most types contain long chains of carbon, hydrogen, and oxygen compounds, with a carbon content of up to 55 wt%[5]. Activated carbon (AC) is a porous material with a high specific surface area, characterized by its remarkable adsorption capacity [1]. This versatile material is commonly produced from lignocellulosic biomass, fossil coals, or polymeric precursors through a thermal process known as pyrolysis. During pyrolysis, the feedstock decomposes and transforms into carbon-based products such as biochar, bio-oil, and gases [6]. A wide range of organic residues have been reported as carbon-rich precursors, including wood, coconut shells, olive stones, and agricultural wastes, among others [2]. These materials are mainly composed of three structural biopolymers: cellulose (40–50%), hemicellulose (20–40%), and lignin (20–30%) [7]. The transformation of biochar into activated carbon can be achieved through either chemical or physical activation. In chemical activation, oxidizing agents such as acids or bases are employed to decompose the carbonized matrix and promote the formation of a highly porous structure [8]. Dyes are a group of organic pollutants with high toxicity that threaten biodiversity due to their degradation into carcinogenic compounds [3]. Among them, methylene blue (MB) is a thiazine-based cationic dye ($C_{16}H_{16}N_3ClS$) widely used in the textile, medical,

and biological industries [4]. Its high solubility in water (43.6 g/L at 25 °C) facilitates its dispersion and persistence in aquatic systems, thus contributing to water contamination.
Adsorption is an efficient and widely used process for the removal of pollutants from water. It relies on the attachment of contaminant molecules onto the surface of a solid adsorbent through physical or chemical interactions [9]. In this study, carbon materials were obtained by pyrolysis of organic residues. The resulting biochar was chemically activated using an acid agent to promote the development of a porous surface. The activated carbon produced was then evaluated as an adsorbent for methylene blue. Finally, the carbon materials were characterized by field-emission scanning electron microscopy (FESEM), Raman spectroscopy, and Fourier-transform infrared spectroscopy (FTIR) to analyze their morphology and chemical composition. The adsorption of methylene blue was quantified using UV–Vis spectroscopy.

Materials and methods

Bursera copalifera waste was used as raw material to obtain biochar. Nitric acid (70% HNO_3) was purchased from Sigma-Aldrich, and methylene blue (MB), with a molecular weight of 319.852 g/mol, was purchased from Merck. Pyrolysis of the previously washed and dried organic material was carried out in a LINDBERG/BLUE M tubular furnace at 500°C in an inert argon atmosphere with a flow rate of 1.0 L/min. The biochar was subsequently chemically activated using an aqueous HNO_3 solution at an acid/biochar ratio of 10:1. The mixture was kept stirring at room temperature and then dried at 100°C to remove moisture. Finally, a second heat treatment was applied under the same conditions as the pyrolysis to evaluate the effect of temperature on the generated functional groups. Activated biochar was characterized by scanning electron microscopy (FESEM, TESCAN MAIA3), Raman spectroscopy (532nm laser), and Fourier transform infrared spectroscopy (FTIR, Thermo Scientific NICOLET 6700). To evaluate the adsorption capacity of methylene blue, a 13.4mg/L solution at pH 7 was prepared, in which 0.1g of material was dispersed in 10 mL without stirring, at room temperature. After the contact time, the mixture was filtered and the remaining AM concentration was determined by UV-Vis spectrophotometry (Hewlett Packard 84524), to calculate the removal efficiency and adsorption capacity of the activated biochar.

Results

Three samples were obtained: Biochar (B), Activated Biochar (AB), Carbonization of Activated Biochar (CAB). All materials were characterized through scanning electron microscopy (SEM), Raman Spectroscopy and FTIR Spectroscopy to know the morphological and structural properties (figure 1). SEM results suggest that the heat treatment and chemical activation significantly modified the surface of the material obtained from *Bursera copallifera*. Changes in surface morphology are crucial to understanding how processing conditions influence structural properties, as they determine key characteristics and in turn affect material performance in applications such as adsorption. The Figure 1b shows that samples B, AB, and CAB exhibit two characteristic Raman features of carbon materials: the G band (~1580 cm^{-1}), associated with the in-plane stretching vibrations of sp^2-hybridized carbon atoms, and the D band (~1350 cm^{-1}), which arises from structural defects or disorder within the carbon lattice. The presence of these bands confirms the formation of an sp^2 carbon structure after the pyrolysis process. In contrast, the Raman spectrum of *Bursera copallifera* leaves does not display the D or G bands typically observed in carbonaceous materials, demonstrating that

pyrolysis effectively converted the biomass into a carbon-rich material. Figure 1c presents the spectra obtained by FTIR and shows the frequency interval, bond, and vibration type of some characteristic bands of functional groups in carbon nanomaterials after activation. To quantify the methylene blue (MB) concentration after contact time with the adsorbent, measurements were made in aqueous solution using UV-Vis spectroscopy. Figure 1d shows the UV–Vis spectra of the analyzed samples, where variations in absorbance can be observed depending on the material and exposure time. The higher absorbance of the base material (target) indicates a significant concentration of dye before contact with the adsorbent materials. In contrast, the decrease in peak intensity relative to the blank confirms the adsorption of the dye. The highest removal efficiency was observed for sample AB, reaching 86% after 15 min, likely due to the introduction of oxygen-containing functional groups and the increased porosity generated during the activation process.

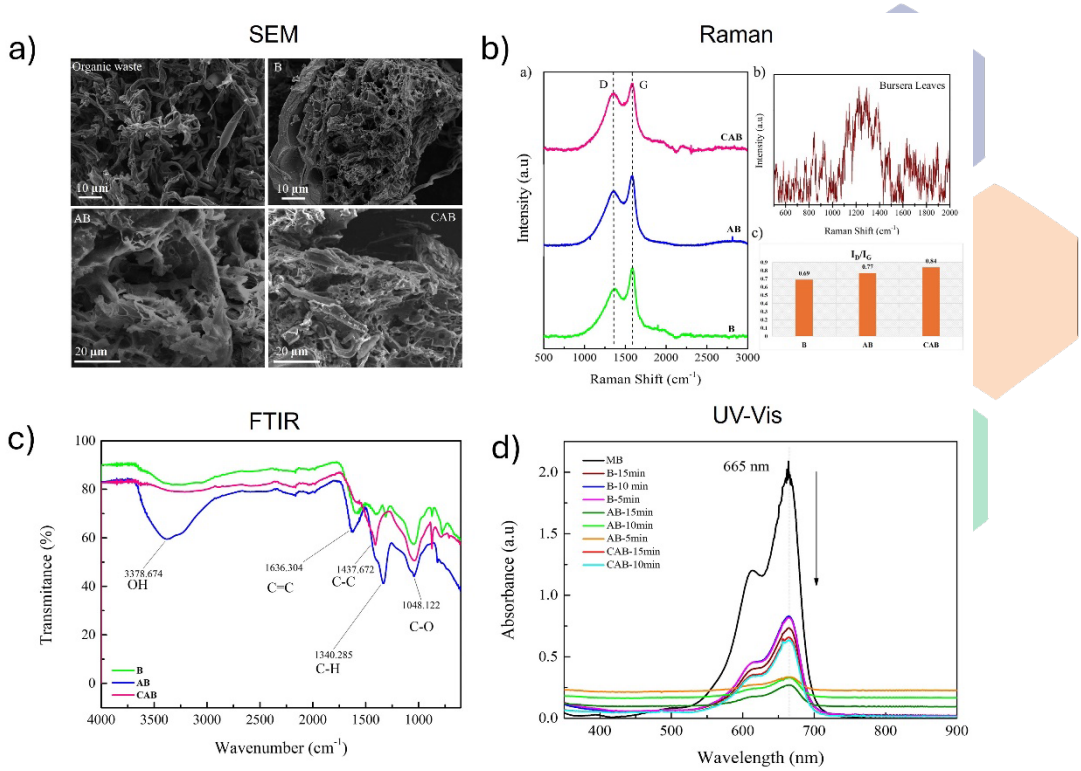

Figure 1. Characterization of the carbon materials obtained in this work by a) SEM, b) Raman Spectroscopy, c) FTIR Spectroscopy, d) UV-Vis spectroscopy.

The results obtained by different characterization techniques suggest the formation of a basic structure of porous carbon through the decomposition of organic material. The activation of carbon with HNO_3 facilitated the formation of pores and the introduction of functional groups on its surface. The adsorption of methylene blue using activated carbon was evidenced. The spectra obtained through UV-Vis showed a significant decrease in the absorbance peak, with better performance observed in the AB samples. These results are comparable to other studies reported in the literature, further supporting the validity of the approach used [9].

Conclusions

This study suggests that this material has great potential for use in pollutant removal. For future research, the activation conditions and biocarbon precursor will be optimized. Additionally, it would be interesting to evaluate its effectiveness for the removal of other contaminants and to study its regeneration and reuse capacity, which would allow assessing its economic and environmental viability. Finally, given its potential, this material could be explored for energy storage applications, such as in supercapacitors, where porosity and functional groups would be key.

References

[1] Z. Heidarinejad, M. H. Dehghani, M. Heidari, G. Javedan, I. Ali, and M. Sillanpää, Environ. Chem. Lett., 2020, 18, 393–415.

[2] Z. Zhai, L. Zhang, T. Du, B. Ren, Y. Xu, S. Wang, et al., Mater. Des., 2022, 221, 111017.

[3] M. Berradi, R. Hsissou, M. Khudhair, M. Assouag, O. Cherkaoui, A. El Bachiri, et al., Heliyon, 2019, 5(11), e02711.

[4] I. Khan, K. Saeed, I. Zekker, B. Zhang, A. H. Hendi, A. Ahmad, et al., Water, 2022, 14(2), 242.

[5] J. George, M. Eldhose, E. Tomy, S. John, A. Joseph, and C. George, Handbook of Biomass, Springer, 2023, 1–26.

[6] A. Márquez, E. Patlaka, S. Sfakiotakis, I. J. Ortiz, and J. M. Sánchez-Hervás, Waste Manag., 2023, 172, 171–181.

[7] M. Iwanow, T. Gärtner, V. Sieber, and B. König, Beilstein J. Org. Chem., 2020, 16, 1188–1202.

[8] Y. Gao, Q. Yue, B. Gao, and A. Li, Sci. Total Environ., 2020, 746, 141094.

[9] Q. Han, J. Wang, B. A. Goodman, J. Xie, and Z. Liu, Powder Technol., 2020, 366, 239–248.

Acknowledgements

The authors gratefully acknowledge to Dr. Miguel Angel Méndez Rojas (University of the Americas Puebla), Dra. Cristina Zorrilla (Institute of physics, UNAM) and Dra. Paola Sanchez Portillo (CIQ-UAEM) for their assistance in the obtaining of SEM, Raman and FTIR measurements respectively.

KINETICS OF SPHERE TO ROD-LIKE MICELLE TRANSITION IN P104 TRIBLOCK COPOLYMER: IMPACT OF COPOLYMER CONCENTRATION, SALTS AND ENCAPSULATED DOXORUBICIN

Maria Fernanda Ulloa Jaimes*[1], Edgar Benjamín Figueroa Ochoa[2], Ramón Gutiérrez Saucedo[2], Gabriel Landazuri Gómez[2], Alberto Gutiérrez Becerra[1], Lourdes Mónica Bravo-Anaya[3]**

[1] Departamento de Ciencias Básicas y Aplicadas e Ingeniería, CUTonalá, Universidad de Guadalajara, México
[2] Departamento de Química, CUCEI, Universidad de Guadalajara, México
[3] Institut des Sciences Chimiques de Rennes, Université de Rennes, Rennes, France
*maria.ulloa3324@alumnos.udg.mx, **lourdes-monica.anaya@univ-rennes1.fr*

Abstract
This study investigated the structural transition of Pluronic® P104 micelles as a function of polymer concentration, NaCl content, and the presence of doxorubicin, using Dynamic Light Scattering (DLS) coupled with temperature-jump experiments. Key physicochemical parameters, including the critical micellar temperature (CMT), giant micelle temperature (GMT), cloud point (CP), and micelle size, were first determined for systems prepared at copolymer concentrations between 1 and 6 wt.%, 0.005-1 M NaCl, and 30-50 μg of doxorubicin. Temperature jumps from 40 °C to 64 °C revealed slow micellar growth dynamics, with characteristic times of 400-700 s. The relaxation rate increased linearly with polymer concentration, consistent with a fusion-fission mechanism. Salt addition slowed the sphere-to-rod transition compared with P104 micelles in pure water, while preliminary results indicated that doxorubicin encapsulation had minimal influence on the growth kinetics.

Introduction
Conventional drug delivery systems, including those used in cancer therapy, face several limitations, such as low specificity, poor stability and solubility and high toxicity with adverse side effects due to the need for elevated doses [1]. The use of nanocarriers offers the potential to develop novel drug delivery platforms with improved physicochemical properties, enabling enhanced drug efficacy, protection against degradation and optimized pharmacokinetic profiles [2]. Pluronics®, also known as triblock copolymers, are nonionic surfactants composed of poly(ethylene oxide) (PEO) and poly(propylene oxide) (PPO) arranged in a PEO-PPO-PEO structure. These copolymers can aggregate above their critical micellar concentration (CMC) or critical micellar temperature (CMT), leading to a coexistence of monomers, micelles and micellar aggregates [3]. Due to their amphiphilic nature, Pluronics® can self-assemble in aqueous solutions into various morphologies, such as spheres or rods [3]. They have been proposed as drug delivery systems because of their biocompatibility, diverse architectures, broad molecular weight range, and commercial availability. The micellar structure and morphological transition temperatures are influenced by factors such as ionic strength and the presence of other molecules [4].
In this study, we investigated the physicochemical properties of Pluronic® P104 (PEO_{27}-PPO_{64}-PEO_{27}) as a function of polymer weight percentage (1- 6% wt), ionic strength (0.005–1

M) and the encapsulated doxorubicin (30-50 µg). The CMT, GMT (giant micellar temperature), the characteristics of the micellar structures and the amount of encapsulated doxorubicin were determined by dynamic light scattering (DLS), temperature sweeps, and UV-Vis measurements, respectively. Additionally, "temperature jump" experiments (from T_1 = 40 °C to T_2 = 64 °C) coupled with DLS were performed to monitor the time-dependent evolution of scattering intensity and hydrodynamic radius. These data were analyzed using a mono-exponential function to determine the apparent growth time [5]. Preliminary results indicate that encapsulated doxorubicin does not consistently affect micellar growth.

Materials and methods

Pluronic® P104 (Mw = 5.9 kDa) was used to prepare micellar solutions (1-6 wt%) in distilled water, and with NaCl concentrations ranging from 0.005 to 1 M. The critical micellar temperature (CMT), giant micellar temperature (GMT), and micellar size distributions were characterized by temperature ramps carried on with dynamic light scattering (DLS). Doxorubicin was encapsulated in the copolymer micelles following the method of *Gutiérrez et al.* [4]. Drug content and encapsulation efficiency were determined by UV-Vis spectroscopy at 480 nm, while micellar sizes were measured by DLS both before and after drug loading. Additionally, temperature-jump DLS experiments were conducted to investigate the kinetics of micellar morphological transitions under abrupt temperature changes.

Results and discussion

Determination of the clouding point: effect of copolymer concentration, NaCl content and doxorubicin

Figure 1a shows the effect of copolymer concentration on the appearance of turbidity. As the concentration increases, the transition occurs at lower temperatures, consistent with previous reports in the literature [3]. At a given temperature, higher copolymer concentration also produces more pronounced turbidity. **Figure 1b** indicates that increasing the NaCl concentration shifts both the onset of visual transitions and the turbidity increase toward lower temperatures. If we compare both figures, we can observe that the cloud point of P104 decreases by around 15 °C, dropping from about 80 °C in pure water to approximately 65 °C at 1 M NaCl.

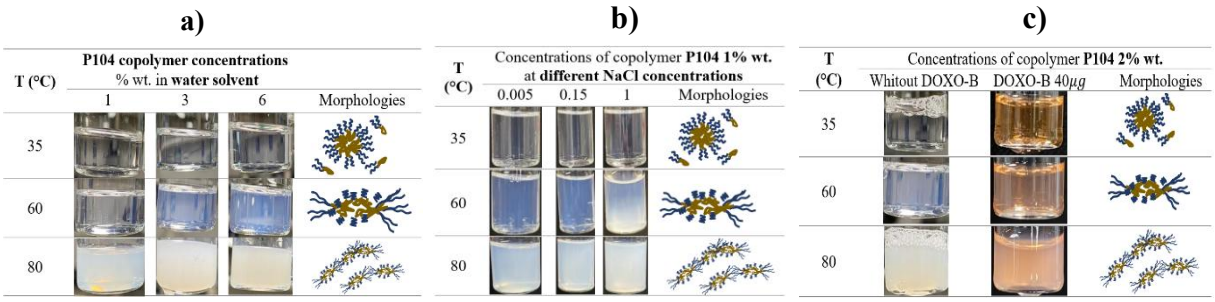

Figure 1. *Visuals observations highlighting the appearance of turbidity in copolymer solutions, as a function of temperature as a function of:* ***a)*** *copolymer concentrations,* ***b)*** *NaCl concentrations,* ***c)*** *in the absence and presence of DOXO.*

Visual observations showed that the presence of DOXO did not influence turbidity levels or the cloud point (CP). **Figure 1c** compares the appearance of turbidity in micellar solutions with and without drug at different temperatures. As expected, DOXO-loaded solutions displayed an orange-reddish coloration due to the intrinsic color of the molecule. At 35 °C, both samples were clear; upon heating to 65 °C, a bluish-white turbidity developed, and at 80 °C both solutions became fully turbid. These observations confirm that drug incorporation does not modify the temperature range associated with the transitions of P104.

Determination of CMC, GMT and micelle sizes through DLS

Figures 2a and **2b** show the evolution of the hydrodynamic radius (R_H) during temperature ramps for P104 micelles as a function of copolymer concentration and NaCl concentration, respectively. In water, the temperature-dependent profiles for 1, 3, and 6 wt% solutions reveal three distinct regions corresponding to unimers, spherical micelles, and elongated micelles. As the concentration increases, the CMT decreases from 34 to 28 °C, and the temperature window associated with spherical micelles becomes narrower (**Figure 2a**). The inset further highlights the linear decrease of both the CMT and GMT with increasing P104 concentration. NaCl also strongly affects the CMT and GMT: increasing ionic strength shifts the onset of micellization to lower temperatures, reduces the spherical micelle region and promotes the formation of larger aggregates at lower temperatures (**Figure 2b**). However, the size of micelles ($R_H \approx 16 \pm 2$ nm) remains constant compared to P104 in pure water.

a) **b)**

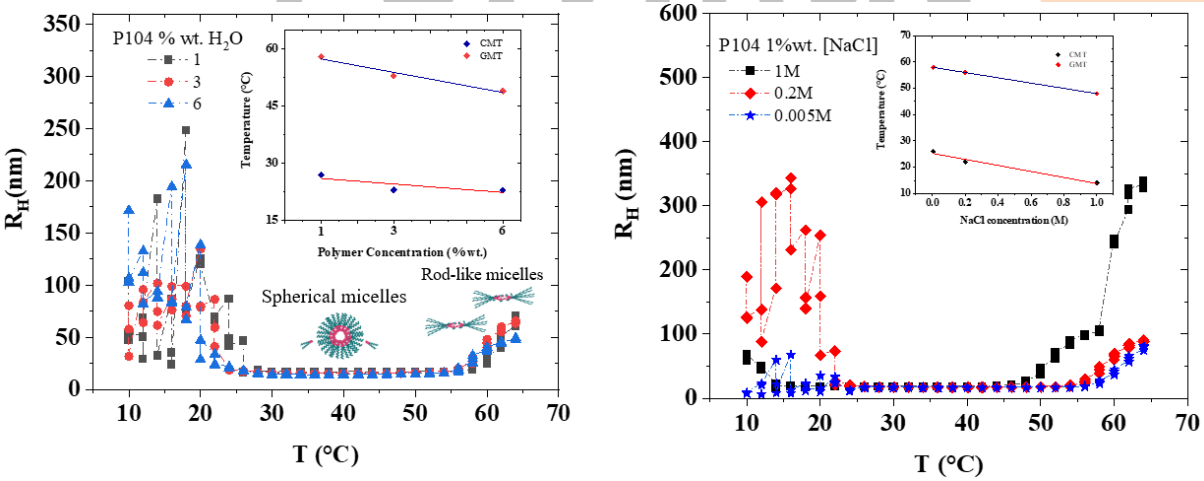

Figure 2. *R_H evolution as a function of temperature for: a) 1, 3 and 6 wt% P104 solutions, and b) 0.005, 0.2 and 1 M NaCl in 1 wt% P104 solution. The inset on each figure shows the CMT and GMT evolution as a function of P104 and NaCl concentration, respectively.*

Effect of polymer concentration, NaCl and doxorubicin in growth kinetics

Figure 3 shows the evolution of R_H and growth kinetics of P104 micelles under different conditions. **Figure 3a** presents R_H over time for a 1 wt% P104 solution subjected to a thermal jump from 40 °C to 64 °C over 3 900 s. R_H growth was analyzed using a mono-exponential function, $R_H(t) = [R_H(\infty) - R_H(0)] * exp(-t/\tau) + R_H(\infty)$, where $R_H(0)$ is the initial radius, $R_H(\infty)$ the equilibrium radius, and τ the apparent growth time. The fits allowed determining the characteristic growth times and the growth rate, $k_{growth} = 1/\tau$. **Figure 3b** shows that k_{growth}

increases linearly with P104 concentration, indicating a fusion–fission mechanism for the transition from spherical to elongated micelles, consistent with previous reports for P103 [5]. **Figure 3c** shows that increasing NaCl concentration accelerates micellar growth. Preliminary studies with DOXO (not shown) show a slight increase in growth rate and a ~50 s decrease in relaxation time, suggesting the drug moderately promotes micellar morphological transitions.

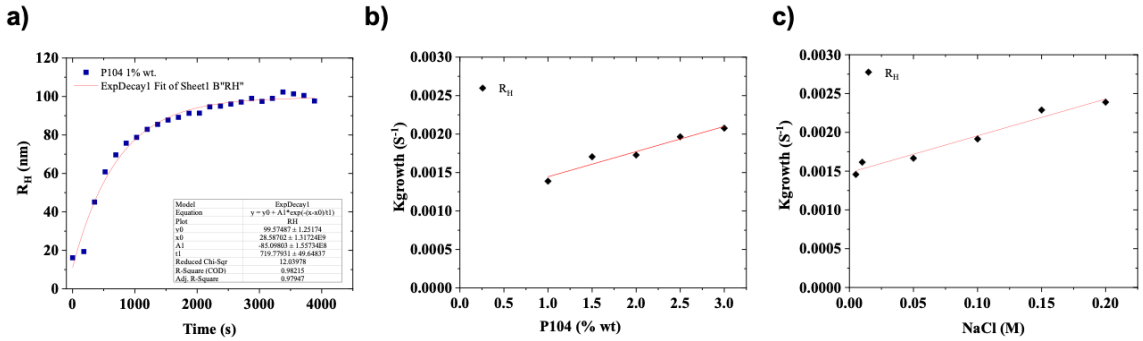

Figure 3. *a) Evolution of R_H for a 1 wt% P104 solution following a temperature jump from 40 °C to 64 °C over 3 900 s. R_H growth was modeled using a mono-exponential function to extract the apparent relaxation time (τ) and corresponding growth rate (k_{growth} = 1/τ). b) Micellar growth rate as a function of C_{P104}, showing a linear increase indicative of a fusion-fission mechanism for the transition from spherical to elongated micelles. c) Growth rate dependence on NaCl concentration for 1 wt% P104 solutions, showing that higher ionic strength accelerates micellar growth.*

Conclusions

P104 transitions identified through visual observations as a function of temperature were confirmed by temperature-dependent measurements. These results showed that the CMT of P104 shifts to lower temperatures as the copolymer concentration increases, a behavior attributed to the larger amount of PEO/PPO blocks in solution that facilitates micellization. Similarly, higher NaCl concentrations promote micellization at reduced temperatures by decreasing copolymer solubility. The GMT also decreases with increasing P104 and NaCl concentrations. In addition, DOXO encapsulation did not modify the temperature range associated with the micellar transitions of P104. Overall, the micellar solutions exhibited continuous and stable growth, progressively evolving into elongated structures. The growth kinetics followed a single-exponential behavior, indicating that micelle evolution is primarily governed by a random fusion-fragmentation mechanism.

References

[1] S. Grund, M. Bauer, D. Fischer, *Adv. Eng. Mater.* **2011**, 13(3).
[2] A. M. Vargason, A. C. Anselmo, S. Mitragotri, *Nat. Biomed. Eng*. **2021**, 5(9), 951–967.
[3] M.J. Kositza, C. Bohne, P. Alexandridis, T.A. Hatton, J.F. Holzwarth, *Langmuir* 1999, 15(2), 322-325.
[4] R.A. Gutiérrez-Saucedo, J.C. Gómez-López, A.A. Villanueva-Briseño, A. Topete, J.F.A. Soltero-Martínez, E. Mendizábal, C.F. Jasso-Gastinel, P. Taboada, and E.B. Figueroa-Ochoa. *Polymers* **2023**, 15(10), 2249.
[5] G. Landazuri, V.V.A. Fernández, J.F.A. Soltero, and Y. Rharbi, *J. Phys. Chem. B* **2012**, 116, 11720−11727.

Acknowledgements

The authors wish to acknowledge the CNRS-IEA P²NanoBio for funding the collaboration between México and France.

MESOPOROUS SILICA NANOCARRIER DOPED WITH CHLOROPHYLL FOR PHOTODYNAMIC THERAPY

Rodríguez Galván Marissa[1], Aparicio Ixta Laura[1], Flores Villavicencio Lérida Liss[2], Villagómez Castro Julio Cesar[2], Pichardo Molina Juan Luis[2]

[1]*Centro de Investigaciones en Óptica, A. C. Loma del Bosque 115, Colonia Lomas del Campestre, C.P. 37150 León, Guanajuato, Mexico. jpichardo@cio.mx*

[2]*Departamento de Biología, División de Ciencias Naturales y Exactas, Universidad de Guanajuato, Noria Alta S/N Col. Noria Alta, C.P. 36050 Guanajuato, Guanajuato, Mexico*

***INTRODUCTION**:* Photodynamic therapy (PDT) is a process in which a photosensitizer (PS) is activated by light, leading to the generation of reactive oxygen species (ROS) to damage or destroy nearby abnormal cells to produce therapeutic effects. However, photosensitizers suffer from limited targeting and aggregation due to their low solubility, leading to optical quenching and reduced therapeutic efficacy. On the other hand, chlorophyll (Chl) is a natural pigment with potential use as a photosensitizer for photodynamic therapy. Previous studies reported that chlorophyllin is readily soluble in water, exhibits very low toxicity, and is less expensive than synthetic photosensitizers [1-2]. In this study, we report the use of Chl obtained from *Argemone ocrholeuca* and loaded into mesoporous silica nanoparticles (MS-NPs) as nanocarriers to enhance its absorption and to evaluate its photodynamic effect in the SH-SY5Y cell line. ROS detection was carried out using the dichlorodihydrofluorescein diacetate (DCFH-DA) assay.

MATERIALS AND METHODS: Chemical reagents were Tetraethyl orthosilicate (TEOS) 99%, cetyltrimethylammonium bromide (CTAB) 99%, ethanol 99%, 3-Aminopropyl triethoxysilane (APTES), Trietanolamina (TEA), and 2',7'-Dichlorodihydrofluorescein diacetate (DCFH-DA) 97%, which were obtained from Sigma-Aldrich. *Argemone ochroleuca* (ArOch) plants were collected from La Sardeneta Leon, Gto. N 21°11'34" W 101°40'44" 1840masl), and chlorophyll was obtained and purified by column chromatography separation. The MS-NPs were fabricated following the method reported by Qiao et al. [3]. In a 250 mL round-bottom flask, a 60 mL solution of CTAB at 85 mM, TEA at 16.6 mM was prepared in water-ethanol (6:1 v/v) at 60 °C under magnetic stirring. After 30 minutes, TEOS at 0.2 mM and APTES at 0.2 µM were added dropwise. The solution was stirred for 2 hours, then cooled at room temperature. The colloid was washed three times with ethanol by centrifugation at 2000 g, and the pellet was resuspended in 20 mL of methanol. Subsequently, 1 mL of concentrated hydrochloric acid (HCl, 30%) was added to remove the excess CTAB, the solution was stirred for 8 hours at 60 °C, then cooled at room temperature. Subsequently, the product was washed three times with ethanol by centrifugation at 2000 g for 5 minutes each, finally the NPs were dried at 70 °C for 12 hours. Morphological characterization was performed using transmission electron microscopy (TEM; Morgagni M-268, Philips/FEI), and micrographs were analyzed using ImageJ. FTIR spectroscopy was performed to identify surface functional groups on MS-NPs (Cary 670, Agilent Technologies Inc.).

A batch of Chl samples at different concentrations was prepared and analyzed with UV-

Vis spectroscopy from 300 to 800 nm (Figure 1c). By plotting optical absorption at λ=408nm against chlorophyll (Chl) concentration, a calibration curve was obtained for calculating the Chl concentration loaded onto MS-NPs, as shown in Figure 1d. Subsecuently Chl was loaded into MS-NPs, followed by the preparation of 5 mL of Chl at a initial loading concentration of 1.0 mM in a round glass flask. Then, 10 mg of MS-NPs were added under magnetic stirring at 25 °C. T_1=1 hour and T_2=2 hours, samples were collected and centrifuged at 2000 g. The supernatant was analyzed by UV-Vis spectroscopy, and Chl concentration was calculated from the calibration curve, next the loading efficiency was calculated using Equation (1).

$$Loading\ efficiency = \frac{(Total\ drug - Free\ drug)}{Total\ drug} \times 100 \quad (1)$$

SH-SY5Y neuroblastoma cell line (ATCC® CRL-2266TM) was cultured in RPMI + GlutaMAX™-I supplemented with fetal bovine serum (Gibco) at a final concentration of 10 % and incubated at 37 °C in a 95 % air, 5 % CO_2 atmosphere. Cell density was maintained at 50-80 % confluence to facilitate development protocols. For ROS analysis, SH-SY5Y cells (2 × 10^5 cells/mL) were exposed to Chl-MS-NPs at 90.4 µg/mL and irradiated with a 532 nm green laser diode (1 mW/cm^2, 3 and 5 min). After adding 10 µM 2',7'-dichlorodihydrofluorescein diacetate (DCFH-DA, Sigma Aldrich), the cells were incubated at 37 °C for 30 min. Finally, the fluorescence of DCF (Ex/Em 502/525 nm) was acquired using an epifluorescence microscope (Filter B, Leica DMLS) with an AxioCam 305 color camera (Carl Zeiss). Controls included untreated and non-irradiated cells.

RESULTS AND DISCUSSION: Figure 1a shows a TEM micrograph of MS-Chl-NPs, which reveals spherical nanoparticles with a mean size of 51 ± 7 nm. Additionally, we included an inset image showing the size distribution of Chl-MS-NPs, obtained from TEM micrographs analyzed in ImageJ.

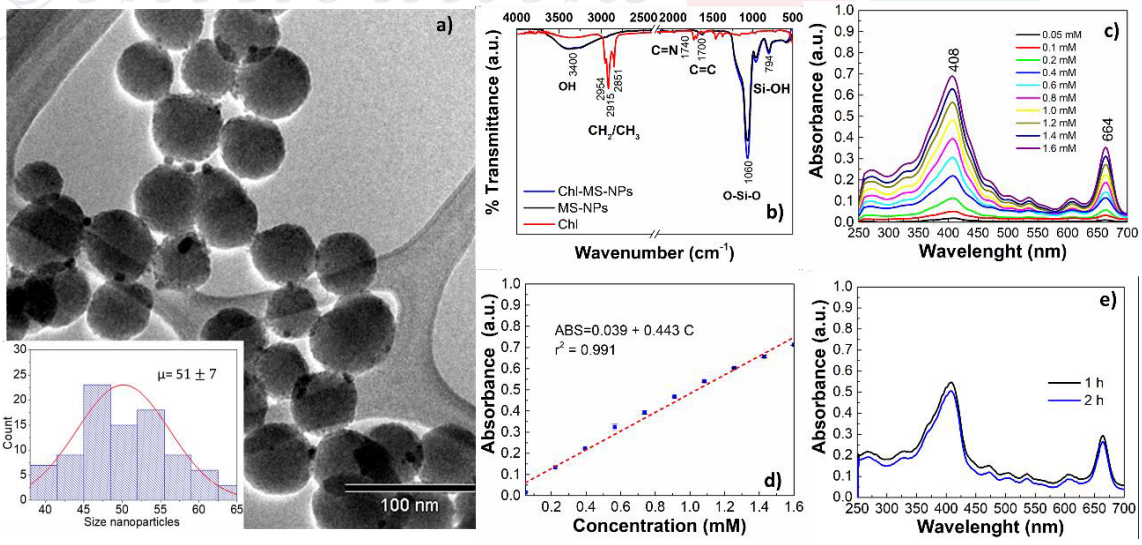

Fig 1. The figure shows a) SEM micrographs of MS-NPs, b) FTIR analysis of Chl, MS-NPs, and Chl-MS-NPs, c) UV-Vis spectra of Chl at different concentrations, d) the calibration curve of Chl at 408 nm, and e) UV-Vis spectra of supernatant after loading Chl.

On the other hand, FTIR spectroscopy was performed on samples of Chl extracts from , MS-NPs, and Chl-MS-NPs, as shown in Figure 1b. Chl sample spectrum shows the stretching vibrations at 2954, 2915, and 2850 cm^{-1} assigned to ($-CH_3$/$-CH_2$), also at 1740 and 1700 cm^{-1} assigned to C=O and C=C, respectively while the spectra of MS-NPs and Chl-MS-NPs show an intense band at 1060 cm^{-1} assigned to the bending mode of O-Si-O, and a less intense peak at 794 cm^{-1} assigned to the bending mode of Si-OH.

After Chl was purified by column chromatography separation, a solution of the purified chlorophyll was prepared in ethanol for future use. Firstly, UV-Vis absorption spectra of chlorophyll were recorded at various concentrations ranging from 0 to 1.6 mM. The maximum absorbance at λ = 408 nm was used for the calibration curve. Figure 1c shows the UV-Vis spectra, Figure 1d shows the corresponding calibration curve, and the red line corresponds to the best linear fit, with an R^2= 0.991. The loading efficiency of Chl in MS-NPs was quantified in the following manner: the supernatant from the loading solution after centrifugation was analyzed by UV-Vis spectroscopy (Figure 1e), and the Chl concentration of supernatant was calculated using the calibration equation show in Figure 1d. After determining the concentration of chlorophyll in the supernatant, the concentration in MS-NPs was calculated as we know the initial Chl used for the loading, finally the loading efficiency was subsequently determined using Equation 1. Table 1 presents the measured chlorophyll concentrations in the Chl-MS-NPs and their corresponding loading efficiencies. The adsorption method we employed for loading chlorophyll onto MS-NPs demonstrated a higher loading efficiency than previously reported by Adnane et al. [4].

Table 1. Chl concentration and loading eficiency in MS-NPs after one and two hours of adsorption are shown.

Time	Chl Concentration in supernatant (mM)	Loading efficiency (%)	Chl/MS-NPs µg/ mg
1h	0.1	10	47.5 ± 4.0
2h	0.2	20	90.4 ± 2.0

ROS generation by laser irradiation of SH-SY5Y cells with and without Chl-MS-NPs was assayed by using DCFH-DA. DCFH-DA was taken up by cells and converted to dichlorofluorescein (DCFH) by intracellular esterase. ROS oxidizes DCFH to the fluorescent DCF. The fluorescence of DCF is directly proportional to the amount of ROS. The results shown the corresponding epifluorescence images of SH-SY5Y cells for the negative and positive controls (Figure 2a and 2b, respectively). The negative control shows no fluorescence, whereas the positive control exhibits significant fluorescence due to H_2O_2-induced oxidative stress. On the other hand, figures 2c and 2d show the cells exposed to two different times of laser irradiation (3 and 5 minutes) without Chl-MS-NPs. In both cases, fluorescence emission was observed, with higher intensity for 5 minutes of laser irradiation at 1 mW/cm^2. Cells incubated with Chl-MS-NPs irradiated for 3 and 5 minutes showed higher fluorescence intensity than the positive control. Cells treated with Chl-MS-NPs and the sample irradiated for 5 minutes showed a marked

increase in fluorescence, indicative of increased oxidative stress driven by elevated ROS levels.

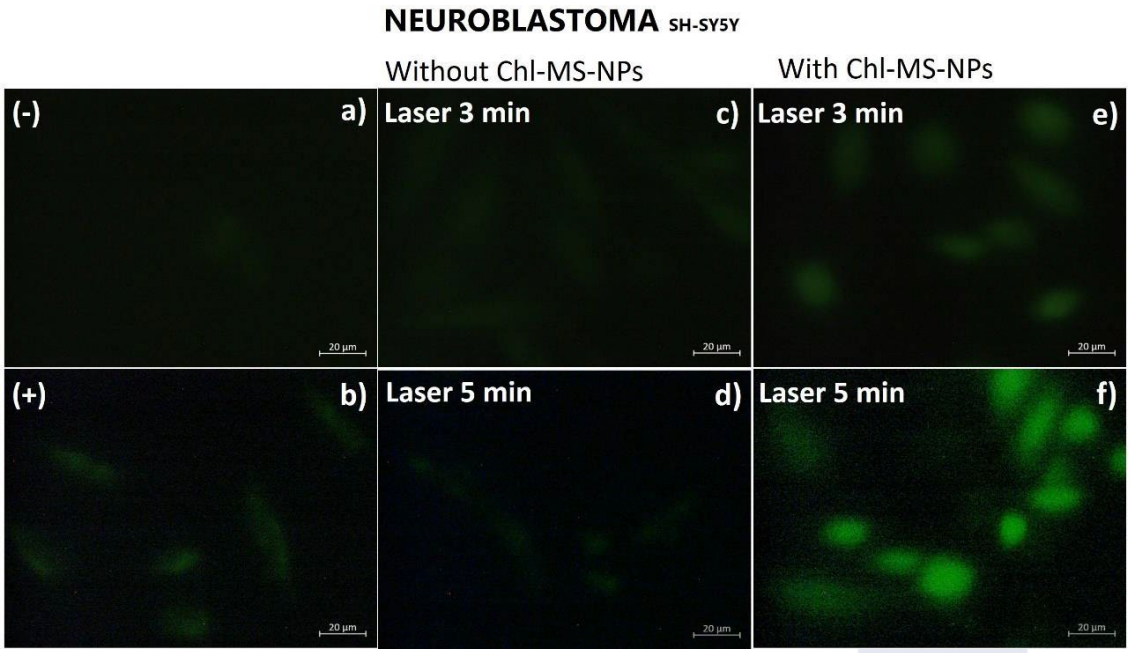

Figure 2. Detection of reactive oxygen species (ROS) by DCFH-DA assay in the SH-SY5Y cell line. Conditions: a) (-) control, b) Treatment with 50 µM H_2O_2 as (+) control, without Chl-MS-NPs, c) three minutes, and d) five minutes of laser irradiation, with Chl-MS-NPs, e) three minutes, and e) five minutes only with laser irradiation.

CONCLUSION

When cell cultures were exposed to Chl-MS-NPs at a concentration of 90.4 µg/mL of Chl and excited with a 532 nm laser at a power density of 1 mW/cm², the NPs generated ROS and fluorescence upon interaction with DCFH-DA, with the effect most pronounced in samples irradiated for 5 minutes. We conclude that even at low radiation power density and short exposure time, Chl-MS-NPs generate ROS, leading to significant oxidative stress in SH-SY5Y cells. However, further experiments are needed to explore other concentrations of Chl-MS-NPs, higher power densities, and longer exposure times to determine the optimal conditions for generating ROS and inducing apoptosis in cancer cells.

References

[1] S. Alexeree et al. A novel synthesis of a chlorophyll b-gold nanoconjugate used for enhancing photodynamic therapy: In vitro study. *Photodiagnosis Photodyn. Ther.*, *35* (2019) 102444.

[2] B. Mansoori Photodynamic therapy for cancer: Role of natural products, *Photodiagnosis Photodyn. Ther.*, 26 (2019) 394-404.

[3] Z. A. Qiao et al. Synthesis of mesoporous silica nanoparticles via controlled hydrolysis and condensation of silicon alkoxide. *Chem. Mater.*, *21*(2009) 3823-3829.

[4] F. Adnane et al. Evaluation of chlorophyll-loaded mesoporous silica nanoparticles for photodynamic therapy on cancer cell lines. Lasers Med. Sci., 39 (2004) 45.

Polymat Contributions

CONSTRUCTION OF MODIFIED SURFACES BASED ON TiO_2-FeO_X FOR THE DEGRADATION OF TOLUENE IN THE GAS PHASE

K. Bolaños, E. P. Hernández-Zozaya, and E. Bustos*
Centro de Investigación y Desarrollo Tecnológico en Electroquímica, S. C.
Parque Tecnológico Querétaro s/n, San Fandila, Pedro Escobedo, Querétaro, 76703, México.
ebustos@cideteq.mx

ABSTRACT

Currently, the problem of pollution affects various aspects of daily life, such as the ongoing respiratory illnesses caused by the large amount of atmospheric emissions. Among the most important pollutants are BTEX (benzene, toluene, ethylbenzene, and xylene isomers), which generate CO_2, CO, and H_2O. These are photoreactive in the atmosphere because they increase the concentration of ozone (O_3) in the mixture of components that make up the air. Consequently, the different reaction mechanisms of these pollutants in the atmosphere hurt the environment, decreasing the quality of breathable air. For this reason, applying treatments that improve the air quality in a given site is of utmost importance. Hence, the main challenge of this research project is the modification of existing materials such as titanium dioxide (TiO_2), which is considered one of the best materials to promote photocatalytic oxidation of organic molecules, however, since it is only active with UV light, the aim is to improve the surfaces with iron oxides (FexOx) in order to increase their degradation capacity in the visible light spectrum.

INTRODUCTION

It is estimated that each year, exposure to air pollution causes seven million premature deaths and the loss of as many millions of years of healthy life. In children, this can lead to reduced growth and significant impairment of lung function, as well as an increased risk of respiratory infections and worsening of asthma. Meanwhile, in adults, ischemic heart disease and stroke are the most common causes of premature death attributable to outdoor air pollution. This is evident in the 2005 global update by the World Health Organization (WHO), which states that there has been a significant increase in evidence demonstrating the impact of air pollution on various aspects of health. Based on these studies, the WHO has modified the determining parameters for air quality by lowering their permissible limits. "The new WHO guidelines recommend air quality levels for six pollutants for which the most recent data on their health effects are available. When action is taken on these classic pollutants—particulate matter (PM), ozone (O_3), nitrogen dioxide (NO_2), sulfur dioxide (SO_2), and carbon monoxide (CO)—other harmful pollutants are also impacted." (New WHO Global Guidelines on Air Quality Aim to Prevent Millions of Deaths Due to Air Pollution, 2021). PM (particulate matter) is primarily generated by fuel combustion in various sectors, including transportation, energy, homes, and industry, among others. These include BTEX pollutants, which are of great interest in current research. Titanium dioxide (TiO_2) is one of the most studied photocatalysts in the field of environmental remediation, as it is environmentally friendly, nontoxic, has good chemical stability, and exhibits suitable conduction band characteristics. Several TiO_2 synthesis techniques have been employed, including sol-gel, flame hydrolysis, water-in-oil microemulsion, chemical vapor deposition, solvothermal, hydrothermal, and electrochemical techniques. With the latter technique, TiO_2 nanotubes ($TiO_{2,nt}$) have been developed, which can perform physical and chemical contaminant removal treatments in water, such as photocatalytic oxidation.

METHODOLOGY

For the development of this research work, electrode preparation was carried out using the anodizing technique, in order to develop the $TiO_{2,nt}$|Ti and Fe_xO_x-$TiO_{2,nt}$|Ti surfaces, as will be explained below:

1. **Sanding sheets with different grit counts**: This activity uses a rough sanding process to improve the adhesion of the nanotubes formed by anodizing.

2. Ultrasonic cleaning: Cleaning must be carried out in a high-intensity sonicator. It is also important to note that after cleaning, avoid touching the surfaces with your skin to avoid leaving residues, such as dead skin or grease, that could interfere with the anodizing process.

3. Assembling the cell: At this stage, special care must be taken to maintain reproducible results, leaving a separation distance of approximately 2 cm between the electrodes and the alligator clip with Teflon to prevent additional electrochemical deposits. At this stage, care must be taken to ensure that the stirrer does not hit the electrodes to ensure better diffusion of the ions in solution to the anode Surface, verifying the current applied to the cell.

4. Sintering in the muffle: the sintering of the titanium electrodes was carried out by placing them facing upwards, since a greater quantity of nanostructures will be present there. The temperature was raised to 600°C for two hours.

5. Modification of electrodes:

5.1. Sonolysis: The first method developed to construct FexOx-TiO_2 |Ti surfaces was based on the method reported by Dong et al. (2010), which used immersion with stirring for a short period (1 h). The surfaces were also immersed in iron compound solutions. For this step, an inert material such as Parafilm was placed on the top end of the plates (the end that hung from the alligator clip during anodization) to support the plate when placed inside the vial, preventing it from being completely submerged. Stirring was carried out in an ultrasonic bath at low intensity for 1 h. The electrodes were then placed on a temperature ramp, maintaining a temperature of 150°C for one hour after induction in the muffle furnace. At the end of the ramp, the temperature was raised to 300°C for 1 h.

5.2. Immersion: The surfaces were immersed in iron solutions, with an inert material such as Parafilm placed on the top end of the plates (the end that hung from the alligator clip during anodization) to support the plate when placed inside the vial, preventing it from being completely submerged. The synthesized electrodes ($TiO_{2,\ nt}$|Ti) were left to soak in the different solutions and their respective mixtures (mentioned in Table 1) for 62.5 h. During this time, the condition of the plates after immersion was monitored. A temperature ramp was carried out, maintaining the temperature at 150°C for 1 h. At the end of this time, the temperature is increased to 300°C for another hour. As part of the characterization of the modified electrodes (16 electrodes) of $TiO_{2,nt}$|Ti and FexOx-$TiO_{2,nt}$|Ti, they were observed using an optical microscope for a superficial review with a 20x eyepiece and a 10x objective, which means a total magnification of 200x.

5.3. Electrolysis: The oxidation of our target contaminant, toluene, is carried out on the Fe_xO_x-TiO_{2nt}|Ti electrode. It is followed by an ethanol solution with a KCl support electrolyte and the target contaminant (toluene at 100 ppm), as the calibration curve was previously performed on a gas chromatograph with a BID detector under these parameters. Constant stirring is required to promote diffusion in the solution, as well as a potential of 2.0 volts, as this ensures the electrolysis of the water. The target solution must be changed when testing each electrode to ensure effective toluene degradation results. The container must be completely sealed to prevent loss of toluene or ethanol due to evaporation, which could alter the consistency of the results. To take the sample for analysis, the cap on the lid was removed, and samples were taken using a micropipette. 0.5 mL samples will be taken every 3 minutes to verify the percentage of degradation over time according to the calibration curve.

5.4. Photo-electrocatalysis: The Fe_xO_x-TiO_{2nt}|Ti electrode, which oxidizes toluene, was included in the electrochemical cell and placed inside a black box to prevent ultraviolet light from escaping. An ethanol solution was then prepared with a KCl support electrolyte and the contaminant under study (toluene at 100 ppm). The calibration curve was previously run on a gas chromatograph with a BID detector under these parameters. Constant stirring is required to promote diffusion in the solution, as well as a potential of 2.0 V, which ensures water electrolysis. The test solution must be changed when testing each electrode to ensure effective toluene degradation results. The container must then be completely sealed to prevent loss of toluene or ethanol due to evaporation, which could affect the consistency of the results. In this way, the sampling valve located at the top of the box is opened to take samples using a micropipette. Samples of 0.5 mL will be taken every 3 minutes to verify the percentage of degradation over time according to the calibration curve.

RESULTS

Figure 1 shows that$TiO_{2,nt}$|Ti without iron modification, using the sonolysis method, obtained an increasing degradation with respect to time, until reaching a maximum of 30% of the toluene present in the solution, which is our standard. It is much higher than the bare titanium electrode, which did not exceed a 3% removal. In contrast, the electrode modified with potassium ferrocyanide ($K_4Fe(CN)_6$) presents a removal of 29.31% similar to the $TiO_{2,nt}$|Ti electrode, being the one that gave the best result of the sonolysis modifications, however, lower than expected. In

addition, it is important to consider that the lower percentage of toluene removal obtained at 15 min was the result of electrolysis using the electrode modified with potassium ferricyanide ($\boldsymbol{K_3Fe(CN)_6}$). The results obtained using the immersion method were mainly non-linear, with a decrease in the toluene removal percentage over time. In this case, toluene degradation was lower than that shown using iron-modified electrodes by sonolysis, with a maximum of 17% using the electrode modified with ferric chloride ($\boldsymbol{FeCl_3}$). In contrast, the "CD" ($\boldsymbol{FeCl_3}$-$\boldsymbol{FeCl_2}$) electrode modified with the mixture of ferric and ferrous chlorides ($\boldsymbol{FeCl_3}$-$\boldsymbol{FeCl_2}$) resulted in a lower removal percentage than bare titanium; this electrode, when analyzed by optical microscope, showed a corroded surface with large crystals heterogeneously dispersed over the surface, which could suggest that this mixture promotes corrosion of the plate.

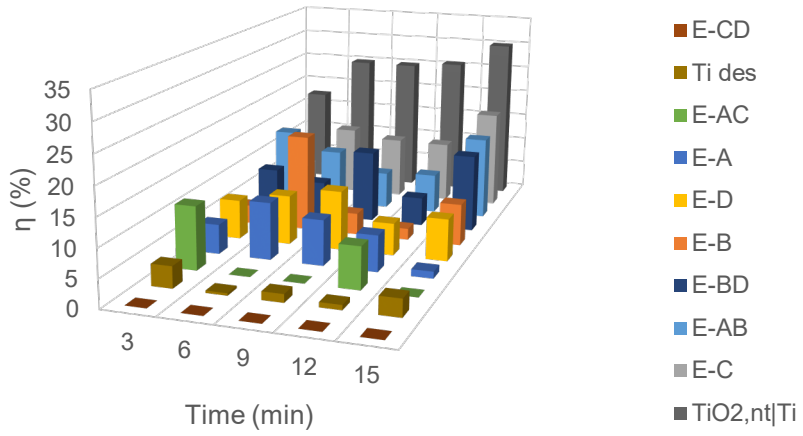

Figure 1. Removal efficiency of toluene by electrolysis (E) using the different modified electrodes in study by inmersión.

CONCLUSIONS

The best result in this study was achieved using only the system with $TiO_{2,nt}$|Ti, without modification by immersion in different solutions with iron, because the adhered Fe_xO_x particles clog the nanostructures, as observed in the spectroscopic characterization. Considering the results obtained in the photoelectrocatalysis experimentation, a generation of byproducts was observed in addition to the fact that the removal was lower than expected. Comparing the data, in the case of electrolysis performed by immersion, there is better removal than in electrode "A" ($K_4Fe(CN)_6$), which presents a low intensity in Raman shift corresponding to iron, while in photocatalysis, it shows the generation of byproducts. A high iron concentration is not necessarily more beneficial than a lower one. Finally, to achieve greater consistency with the data and determine whether the methodology is successful, Raman spectroscopy analyses of the electrodes modified by sonolysis must be available for their respective evaluations.

REFERENCES.

Agency for Toxic Substances and Disease Registry. (2007). Toxicological Profile for Benzene.

Aung, W. Y., Noguchi, M., Pan-Nu Yi, E. E., Thant, Z., Uchiyama, S., Win-Shwe, T. T., Kunugita, N., Mar, O. (2019). Preliminary assessment of outdoor and indoor air quality in Yangon city, Myanmar. Atmospheric Pollution Research, 10(3): 722–730. https://doi.org/10.1016/j.apr.2018.11.011

Alfaro, J. A. (Agosto de 2010). Síntesis y deposición sonoquímica de nanopartículas de plata. *Síntesis y deposición sonoquímica de nanopartículas de plata*. Saltillo, Coahuila, México.

Barroso Martínez, J. Sh., Sandoval González, A. S., Cerro López, M., Espejel Ayala, F., Cárdenas Mijangos, J., Treviño Reséndez, J. J., Meas Vöng, Y., Manríquez Rocha, J., Bustos Bustos, E. (2021) Electrochemical degradation of amoxicillin in acidic aqueous medium using TiO_2-based electrodes modified by oxides of transition metals. Environmental Science and Pollution Research. https://doi.org/10.1007/s11356-021-15315-1.

Castro Gonzales, A. I. (2009). Degradación de BTEX en fase gaseosa por biofiltración: aplicación en campo. Comisión Federal para la Protección contra Riesgos Sanitarios. (2017). Normas Oficiales Mexicanas (NOM) de Calidad del Aire Ambiente. https://www.gob.mx/cofepris/acciones-y-programas/4-normas-oficiales-mexicanas-nom-de-calidad-del-aire-ambiente

Corona, D. A. (2015). *Física Uson*. Obtenido de Física Uson http://paginas.fisica.uson.mx/armando.ayala/cursos/moderna2/Electrolisis.pdf

Daly, A., Cognuck Gonzáles, S. (2021). Calidad del aire ¡Es el momento de actuar! In

UNICEF. De la Rosa Fernando, A. F., Ramírez Peñaherrera, V. E. (2012). Cuantificación de compuestos aromáticos (BTEX) en las emisiones gaseosas de fuentes móviles terrestres de gasolina en el Distrito Metropolitano de Quito. Dirección de Monitoreo Atmosférico. (2016). BTEX. http://www.aire.cdmx.gob.mx/default.php?opc=%27Y6BhnmKkaQ==%27

El-Hashemy, M. A., Ali, H. M. (2018). Characterization of BTEX group of VOCs and inhalation risks in indoor microenvironments at small enterprises. Science of the Total Environment, 645:974–983. https://doi.org/10.1016/j.scitotenv.2018.07.157

Environmental Protection Agency. (2019). Purificadores de aire. Un resumen técnico. Estéves, D., Dimas-Neri, E., Casanova-Gómez, M. T., Cerón-Bretón, J. G., Cerón-Bretón.

R. M., Rustrián-Portilla, E., Houbron, E., & Cima, C. (2015). Niveles de BTEX en airemambiente y niveles de riesgo carcinogénico de benceno en un sitio urbano en el centro de Veracruz. Asociación Mexicana De Ingeniería Ciencia Y Gestión Ambiental, a.C. Amica, 1–8. http://www.amica.com.mx/issn/archivos/121.pdf

Gholami, M., Reza Nassehinia, H., Jafari, A. J., Nasseri, S., Esrafili, A. (2014). Comparison of Benzene & Toluene removal from synthetic polluted aire with use of Nano photocatalytic TiO2/ZnO process. Journal of Environmental Health Science & Engineering, 12 (45):7363–7369. https://doi.org/10.1039/c4ra10604k

Gómez, C. (2006). Evaluación de compuestos orgánicos volátiles en emplazamientos urbanos, de fondo urbano e industriales de la capv. González, A. S., Solis-Cortazar, J. C., Pineda-Arellano, C. A., Ramírez-Morales, E., de los Monteros, A. E., & Silva-Martínez, S. (2019) Synthesis of Ruthenium-Doped TiO2 Nanotube Arrays for the Photocatalytic Degradation of Terasil Blue Dye, Journal of Nanoscience and Nanotechnology, 19(8):5211–5219. https://doi.org/10.1166/jnn.2019.16823.

INE-SEMARNAT (2006). Guía metodológica para la estimación de emisiones vehiculares.

INECC (2015). Evaluación de Compuestos Orgánicos Volátiles en la Zona Metropolitana del Valle de México.

Jafari, A. J., Delikhoon, M., Rastani, M. J., Baghani, A. N., Sorooshian, A., Rohani-Rasaf, M., Kermani, M., Kalantary, R. R., Golbaz, S., Golkhorshidi, F. (2021). Characteristics of gaseous and particulate air pollutants at four different urban hotspots in Tehran, Iran. Sustainable Cities and Society, 70 (April):102907. https://doi.org/10.1016/j.scs.2021.102907

Lan, T. T. N., Binh, N. T. T. (2012). Daily roadside BTEX concentrations in East Asia measured by the Lanwatsu, Radiello and Ultra I SKS passive samplers. Science of the Total Environment, 441:248-257.

Lenntech USA LLC (Américas). (s.f.). *LENNTECH*. Obtenido de https://www.lenntech.es/electrolisis.htm

Liao, D., Li, E., Li, J., Zeng, P., Feng, R. (2018). Removal of benzene, toluene, xylene and styrene by biotrickling filters and identification of their interactions. PLOS ONE, 13(1):1–16.

Marć, M., Bielawska, M., Wardencki, W., Namieśnik, J., Zabiegała, B. (2015). The influence of meteorological conditions and anthropogenic activities on the seasonal fluctuations of BTEX in the urban air of the Hanseatic city of Gdansk, Poland. Environmental Science and Pollution Research, 22(15):11940–11954.

Martinez, J. Á. (2018). Síntesis, caracterización y uso en catálisis heterogénea de nanotubos de titanatos. Nuevo León, México: Universidad Autónoma de Nuevo León.

Mosaddegh, M. H., Jafarian, A., Ghasemi, A., Mosaddegh, A. (2014). Phytoremediation of benzene, toluene , ethylbenzene and xylene contaminated air by D. deremensis and O . microdasys plants. Journal of Environmental Health Science & Engineering, 12(39): 1–7.

OMS. (2021). Contaminación del aire ambiente (exterior). https://www.who.int/es/news-room/fact-sheets/detail/ambient-(outdoor)-air-quality-and-health

Paredes, J. L. (2009). El uso de la anodización. México: Casa del Tiempo.

Pekey, B., Yilmaz, H. (2011). The use of passive sampling monitor spatial trends of volatile organic compounds (VOCs) in one industrial city of Turkey. Microchemical Journal, 97:213–219. https://doi.org/10.1016/j.microc.2010.09.006

Petrucci, R. H., Herring, F. G., Madura, J. D., Bissonnette, C. (2011). Química General: Principios y Aplicaciones Modernas. In Química General. Programas Internacionales. (n.d.). AIRE.ORG.MX. https://aire.org.mx/programas-internacionales/Puigcerver, M., Carrascal, M. D. (2008). El medio atmosférico: meterología y contaminación. Universitat de Barcelona, 245.

Raysoni, A. U., Stock, T. H., Samat, J. A., Chavez, M. C., Sarnat, S. E., Montoya, T., Holguin, F., Li, W. W. (2017). Evaluation of VOC concentrations in indoor and outdoor microenvironments at near-road schools. Environmental Pollution, 231:681–693.

Regonini, D., Bowen, C. R., Jaroenworaluck, A., Stevens, R. (2013). A review of growth mechanism, structure and crystallinity of anodized TiO2 nanotubes, Materials Science and Engineering: R: Reports, 74(12):377–406. https://doi.org/10.1016/j.mser.2013.10.001.

Rojas, B. L., Garibay, B. V. (2003). Las partículas suspendidas, aeropartículas o aerosoles: ¿hacen daño a la salud ?; ¿podemos hacer algo? Gaceta Ecológica, 69(octubre-diciembre), 29–44.

NOM-086-SEMARNAT-SENER-SCFI-2005 (2005). Especificaciones de los combustibles fósiles para la protección ambiental.

OMS. Las nuevas Directrices mundiales de la OMS sobre la calidad del aire tienen como objetivo evitar millones de muertes debidas a la contaminación del aire. (2021). Recuperado 29 de septiembre de 2022, de https://www.who.int/es/news/item/22-09-2021-new-who-global-air-quality-guidelines-aim-to-save-millions-of-lives-from-air-pollution#:%7E:text=y%20el%20tabaquismo.-,La%20contaminaci%C3%B3n%20del%20aire%20es%20una%20de%20las%20mayores%20amenazas,vez%20la%20calidad%20del%20aire.

SMA-GDF, INE-DGCENICA, UAMI. (2008). Technical Report on Monitoring and Evaluation of the concentrations of volatile organic compounds in the Metropolitan Area of Mexico City.

Spiegel, J., Maystre, L. Y. (2007). Enciclopedia de Salud y Seguridad en el Trabajo. In Ministerio de Trabajo y Seguridad Social, 4:508–512. https://doi.org/10.1157/13109987

USEPA. (2016). Technical Overview of Volatile Organic Compounds. https://www.epa.gov/indoor-air-quality-iaq/technical-overview-volatileorganic-compounds

Vera, L. M. (2007). Unidad X: Electroquímica. Facultad de Ciencias Exactas y Naturales y Agrimensura. Obtenido de https://exa.unne.edu.ar/quimica/quimgeneral/temas_parciales/unidad_10_Electroquimica2007.pdf

Wöhrnschimmel, H., Zuk, M., Martínez-Villa, G., Cerón, J., Cárdenas, B., Rojas Bracho, L., & Fernádez Bremauntz, A. (2008). The impact a bus rapid transit system on commuters' exposure to benzene, CO, PM2.5 and PM10 in Mexico City. Atmosphere, 42. https://doi.org/8194-8203

EVALUATION OF ENVIRONMENTAL ERGONOMICS AND THE IMPACT IN THE PRODUCTIVITY AND QUALITY LEVELS IN AN ELECTRONICS INDUSTRY OF MEXICALI, BC, MEXICO

Carlos Raúl Navarro Gonzalez[1], Gustavo López Badilla[2], Martín Humberto Llamas Haro[3], Verónica Arredondo Robledo[1], Ana Laura Sánchez Corona[1], Luis Andrés Mondragón Chavero[4], Arilí Cárdenas Robles[5], Eddna Teresa Valenzuela Martínez[5], África Casillas Higuera[6]

[1]Departamento de Ingeniería Industrial, Universidad Autónoma de Baja California, Mexicali, Baja California, México.

[2]Departamento de Ciencias Avanzadas, Universidad Vasconcelos, Campus Murua, Tijuana, Baja California, México.

[3]Departamento de Investigacion y Posgrado, Universidad Vasconcelos, Campus Río, Tijuana, Baja California, México.

[4]Departamento de Ingeniería Industrial, CETYS Universidad, Tijuana, Baja California, México.

[5]Departamento de Mecánica, Universidad Autónoma de Baja California, Mexicali, Baja California, México.

[6]Departamento de Ciencias Básicas, Universidad Autónoma de Baja California, Mexicali, Baja California, México.

ABSTRACT

The environmental ergonomics is a relevant thematic in the operative yielding of workers of industrial process of any type of industrial company in the world, because in accord of the environmental condictiones in indoors of industrial companies, are generated the industrial operations by personnel of manufacturing areas. In this investigation was made an analysis of the environmental factors as ranges of pollution and climatic parameters in an electronics industry and be correlated by operative yielding (OP) of workers of one manufacturing area and the impact in the productivity and quality levels, presenting an increase in the OP of workers when the environmental indices (air pollution parameters and climatic factors), were good conditions, as less of the Air Quality Standards (AQS) in the Tijuana city. The principal air pollutants evaluated were the Sulphur Dioxide (SO_2), Nitrogen Oxides (NO_X) and Carbon Monoxide (CO), and in addition with the principal climatic factors as Temperature (T, °C) and Relative Humidity (RH, %), where the main sources emitted were the traffic vehicle, industries as anthropogenic sources generating air pollutants as the mentioned above. When was presented good environmental conditions with specialized filters to the air pollutants and refrigerated areas of indoors of the electronics industry evaluated, the OP of workers was adequate and was a positive impact in the productivity and quality indices, with an increase, two after be beginning this investigation, when was controlled the enviromental factors. This scientific study was made in 2023 from January to December.

Keywords Electronics Industry, Enviromental Ergonomics, Operative Yielding, Productivity and Quality Levels.

INTRODUCTION

The enviromental ergonomics is very important in the labor well conditions of workers of manufacturing aeras and industrial processes of industrial plants of any type of product manufactured[1]. This relevant thematic can evaluate the air pollution and climatic factors levels, and also the industrial noise, vibrations of industrial equipments and machinery and luminosity of electrical lamps. These interesting factors are very important in the operative yielding of operative personnel of the industrial processes, which in sometimes, when not are controlled these

enviromental ergonomics aspects, can suffer of the origination of the acute respiratory illness (ARI) or others type of diseases as skin and stomach health symptoms. The principal objectives of the enviromental ergonomics are expressed now in table 1[2].

Table 1Main objectives of the enviromental ergonomics

Objectives
Maintaining the health and well-being of workers. It is necessary to maintain comfortable and safe indoor environments in any type of industry so that workers in manufacturing and industrial processes can comfortably carry out their industrial operations. The five main environmental ergonomics factors mentioned above must be evaluated, with the appropriate levels, according to Mexican and international regulations.
It is vitally important to consider that adequate working conditions for workers in industrial processes will generate efficient functions for operational personnel and, consequently, increase the productivity and quality of manufactured products in any type of industry. Maintaining optimal working conditions can help prevent injuries, stress, or even musculoskeletal disorders, and lead to greater job satisfaction and productivity.
The evaluation and application of specialized techniques of enviromental ergonomics, can reduce costs by the possibility of origination of health symptoms mentioned above, and to avoid the presence of fines, and with this an increase of production costs.
Is necessary apply the Mexican and international normativity, to maintain controlled the five enviromental ergonomics parameters, and with this the optimal labor well conditions of workers of manufacturing areas and industrial processes of any type of industry.
Every industrial company must consider improving its image. Directors, managers, supervisors, specialized personnel, and operational staff must collaborate in improving the interior work environments of industrial companies to ensure that workers do not suffer accidents or illnesses in their workplaces. This will lead to better customer perceptions, improving sales and, consequently, economic profits. Furthermore, workers will feel they are working in a safe and comfortable industrial company and will be able to remain in their jobs for years to come.

Health symptoms in industries

The health symptoms in industrial activities can occurs when any type of uncontrolled agents, could be provoke any type of diseases of traumatic symptoms in workers of industrial processes, reducing his operative yielding and with this, the possibility of cause errors and defective products manufactured in the industries[3]. For this reason, is necessary evaluate essentially the five environmental ergonomics parameters mentioned above, and with this, will be a comfortable environment in indoors of industrial companies, and avoid in the major of the cases, the presence of any type of health symptoms of workers[4]. The main health symptoms of workers mentioned above, are illustrated in table 2, for a better understanding of this type of relevant topic in industrial companies[5].

Table 2 Essential health symptoms occurred in industrial processes

Health Symptoms	Causes
Acute Respiratory Illness	Are generated by the exposition of aggressive environments containing acidic agents as air pollutants (SO_2, NO_X and CO, mentioned above) principally, in indoors of industrial plants.
Musculoskeletal Symptoms	Are originated by over effort of some industrial activities elaborated by the operative personnel of industrial processes and manufacturing areas of industrial companies.
Skin Diseases	Can occurs by the presence of air pollutants mentioned above, where are added to the skin and originates damage in skin, and could be

	occurred the dermatitis.

METHODOLOY

In this investigation was realized some activities to analyze the effects of the five environmental ergonomics factors mentioned, when these relevant aspects are uncontrolled, and could be originates health symptoms in workers of manufacturing areas and industrial processes. These actions elaborated are presented in the next paragraphs:

a) Evaluation of the five environmental ergonomics parameters analyzed in this scientific study.

b) Correlation analysis of the occurrence of health symptoms in this electronics industry that permits make this scientific study.

RESULTS

The evaluations show relevant information in the next sections, which supports to improve the essential industrial process elaborated by operative personnel and industrial equipments and machinery.

Evaluation of enviromental ergonomics factors

In this section was made an analysis of the main sources that were originated the occurrence of the enviromental ergonomics factors evaluated and are expressed in table 3.

Table 3 Analysis of essential agents of the enviromental ergonomics evaluated in this investigation (2023)

Environmental Ergonomics Parameters	Main Causes in this Investigation
Air Pollution Agents	Are emitted principally by anthropogenic sources of traffic vehicle and industrial activities of outdoors activities that penetrate to this industrial city.
Climatic Factors	Can originates variations in small periods of times (in temperature and RH factors), generated by the presence of aggressive environments in indoors of this electronics industry.
Industrial Noise	Occurs when were utilized by prolongated periods of time, industrial equipments and machinery without control of the industrial noise, causing uncomfortable environments, even using earplugs.
Luminosity	Is necessary control this factor, which can originate inadequate luminosity, when electrical lamps have any type of electrical failures, by old electrical lamps, old or inadequate electrical wiring or inadequate intensity light by angles or directions of electrical lamps.
Vibrations of Industrial Equipments and Machinery	Are presented by excessive time of use and position of the industrial equipments and machinery in the industrial processes and nor apply the preventive and predictive maintenance

Table 3 represents the main causes occurred in the scientific study elaborated in this electronics industry, and where was observed the factors involved in the uncontrolled environmental ergonomics parameters.

Correlation analysis of enviromental ergonomics and health symptoms

The uncontrolled enviromental ergonomics generated some health symptoms that are presented in table 4. In this table are presented numerical data percentage indices, correlating the enviromental

ergonomics factors analyzed and the occurrence of health symptoms. As is illustrated in table 4, the percentage levels of correlation analysis show the reduction action from the before of the investigation to the after of the investigation process, indicating that with the specialized strategic applied as the use of specialized filters to detect and avoid to enter to indoors of this electronics industry, and the use of automatized systems to control the air pollution agents, climatic factors, luminosity, industrial noise and vibrations of industrial equipments and machinery.

Table 4 Health symptoms presented in the electronics industry evaluated (2023)

Health Symptoms	**ARI**		**Skin Diseases**		**Stomach Symptoms**	
Environmental Ergonomics Factors	**BI**	**AI**	**BI**	**AI**	**BI**	**AI**
Air Pollutants	86	22	83	20	80	21
Climatic Parameters	87	23	82	21	79	19
Industrial Noise	84	18	80	18	81	20
Luminosity	83	22	77	20	80	24
Vibrations of Industrial Equipments and Machinery	86	20	79	23	83	22

BI. Before this investigation; AI. After this investigation

CONCLUSIONS

This investigation was relevant in this electronics industry to control the enviromental ergonomics parameters and with this generates labor well conditions in indoors of the is industrial plant, where was presented before make this investigation some critical cases of the occurrence of health symptoms in workers of manufacturing areas and industrial processes of this industry, as respiratory diseases as ARI, some musculoskeletal symptoms by elaborate the industrial activities very fast or without energy and lack of control of workers. This was concerning to directive people, managers, supervision and specialized persons, and this industry presented a lot errors, defective products fabricated, low operative yielding of workers, low productivity and quality indices and economical losses. With this scientific study, were increased he operative yielding, productivity, and quality levels and the economical gains.

REFERENCES

[1] Asadabadi M., Ahmadi H., Gupta H., Liou J. (2023). “Supplier Selection to Support Environmental Sustainability: The Stratified, BWM TOPSIS Method. Ann. Oper. Res. 2023,322, 321–344.

[2] Acquah A., D’Souza C., Martin B., Arko-Mensah J., Botwe P., Tettey P., Dwomoh D., Nti A., Kwarteng L., Tyaki S., Quaki I., Robins T., Fobil J. N. (2021b). “A Preliminary Assessment of Physical Work Exposures among Electronic Waste Workers at Agbogbloshie, Accra Ghana”, International Journal of Industrial Ergonomics, 82, 1-13.

[3] Carlos Raúl Navarro González, Yanet Villarreal González, Pedro Alberto Escárcega Zepeda, Rigoberto Zamora Alarcón (2022). “Comparative Evaluation of the Environmental Ergonomics Factors in Indoors of the Electronics Industry in Arid and Marine Environments of the Northwest of Mexico”, Partners Universal International Research Journal, Volume: 01Issue: 04| October-December2022|ISSN:2583-5602, 166-174.

[4] Tebcheran T., Phillip Koshute T., Hooper D., Toms M., Holtry R. (2025). “Estimating military working dog core temperature change with machine learning: A simulation Study”, Journal of Thermal Biology, Volume 131, July 2025, 10421.

[5] Hallam, C.; Contreras, C. Management Decision Integrating lean and green management. Manag. Decis., 2016, ,54, 2157–2187.

Polymat Contributions

MICROANALYSIS OF METALLIC CORROSION ON MATERIALS USED IN THE ELECTRONICS INDUSTRY OF TIJUANA

José Manuel Alejandro Gómez Castillo[1], Martin Humberto Llamas Haro[2], Gustavo López Badilla[3], Rosa María Duque Sevilla[4], María del Carmen Corral Nuñez[1], Arilí Cárdenas Robles[5], Eddna Teresa Valenzuela Martínez[5], África Casillas Higuera[6]

[1]Instituto Internacional de Desarrollo Empresarial-INIDE, Tijuana Baja California, México
[2]Departamento de Investigacion y Posgrado, Universidad Vasconcelos, Campus Río, Tijuana, Baja California, México.
[3]Departamento de Ciencias Avanzadas, Universidad Vasconcelos, Campus Murua, Tijuana, Baja California, México.
[4]Departamento de Ingeniería Industrial, Tecnológico Nacional de México, Instituto Tecnológico de Tijuana, Tijuana, Baja California, México
[5]Departamento de Mecánica, Universidad Autónoma de Baja California, Mexicali, Baja California, México.
[6]Departamento de Ciencias Básicas, Universidad Autónoma de Baja California, Mexicali, Baja California, México.

ABSTRACT

This investigation was made to determine the principal factors that was generated the corroded metallic surfaces of products manufactured in an electronics industry, which is located in the Tijuana city that is considered an industrial city of the northwest of the Mexican Republic. This scientific study was relevant because was determined the main air pollutants that were evaluated in this region of our country, where are analyzed the Sulphur Dioxide (SO_2), Nitrogen Oxides (NO_X), Carbon Monoxide (CO) and Ion Chlorides (Cl^-). The climatic parameters involved in this investigation were the temperature (°C) and relative humidity (%), where all factors mentioned as atmospheric aspects were a negative impact in the deterioration of the metallic surfaces of materials utilized in the electronics industry as electrical connectors and micro components used in the fabrication of cell phones of this industrial company, located in this industrial city. The Scanning Electron Microscopy (SEM) was utilized to determine the grade of impact of deterioration of each air pollutant added to the climatic factors, being made this scientific study in 2023 to evaluate the corrosion phenomena in the metallic materials of cell phones.

Keywords Metallic materials, electronics industry, SEM, corrosion phenomena

INTRODUCTION

Metallic corrosion is a negative action that generates deterioration in metallic materials used in the electrical connections of the electronic devices and systems utilized in the industrial equipments and machinery utilized in manufacturing areas of industries[1]. This action can originate errors or stop of industrial equipment and machinery, and thus even the shutdown of a production line, and also in sometimes can industrial equipments and machinery works inadequately, elaborating bad functions and can causes defective products in this electronics industry, of fabricated products were damaged by the metallic corrosion[2]. In this scientific study, was evaluated the occurrence of the metallic corrosion, observing the presence of uniform and pitting corrosion in the metallic surfaces of electrical connections of electronic devices and systems mentioned above. The principal factors that originated the metallic corrosion in this investigation, were the presence of air pollutants as SO_2, NO_X, CO as anthropogenic sources and the Cl^- as natural source from

the sea breeze, which overpass la air quality standards, in some periods of the 2023 year where was evaluated this scientific study in this electronics industry[3]. The presence of air pollutants in addition of variations of climatic parameters, generating aggressive environments, being the SO_2 and NO_X, and the both climatic factors analyzed (Temperature (°C) and Relative Humidity (%)), the essential agents that contributed to the occurrence of the metallic corrosion in the two main types of corrosion mentioned[1].

Metallic corrosion generated by atmospheric factors

The air pollutants mentioned are emitted principally by the traffic vehicle and industrial activities, where industrial plants that are installed next of boulevards, as is occurred in this scientific study, which the electronics industry is located next to Otay Blvd in the Tijuana city., considered as industrial region of the northwest of the Mexican Republic[1]. In this zone of Tijuana, pass a lot cars, being the maximum hours of traffic vehicle, from the 6 AM to 8AM, in the time where enter people of industrial companies and students of kinder garden, elementary, medium high school, high school and universities to schools[2]. Then from 1PM to 3PM, the traffic vehicle is heavy and finally from 5PM to 7PM, the traffic vehicle is complicated. In these periods of times, this anthropogenic source originates considerable levels of SO_2, NO_X and CO; and the industrial activities are other type of human source, which generates essentially, the air pollutants mentioned, and these air pollution agents penetrates to holes, ceilings, gaps in areas with controlled environments, and sometimes, by keeping doors and windows open; generating the aggressive environments that provoke the occurrence of the metallic corrosion[4]. Also, the variations of the climatic parameters evaluated, contributes to the presence of main types of the corrosion phenomena (uniform and pitting), because were generated wet or dry environments, being relevant to the occurrence of the metallic corrosion, in addition with the air pollutants analyzed[5].

Air Quality Standards

Are very important in the generation of the metallic corrosion, when not are controlled the main air pollutants and the climatic parameters in indoors of industrial companies2. The Air Quality Standards (AQS) of the air pollutants mentioned, were proposed and monitored constantly by the Mexican normativity of the Secretaria de Medio Ambiente y Recursos Naturales (SEMARNAT-Mexico) and the Enviromental Protection Agency (EPA-USA), from around 40 years ago. Table 1 shows the AQS of the atmospheric factors evaluated in this scientific study3.

Table 1 Atmospheric parameters evaluated (2023)

AQS Atmospheric Agents	Standard Level	Main Sources
Air Pollutants		
Cl^-**	By 8 Hours (250 mg/L) and 1 Hour (25 mg/L)	Sea Breeze
CO*	By 8 Hours (9ppm) and 1 Hour (35 ppm)	Industrial Activities and Traffic Vehicle
NO_2*	By 1 Hour (100 ppb) and 1 Year (53 ppb)	Industrial Activities and Traffic Vehicle

SO_2*	By 1 Hour (75 ppb) and 1 Year (10 ppb)	Industrial Activities and Traffic Vehicle
Climatic Parameters		
Relative Humidity, %	In indoors of industries (30 % to 50%)	Environmental Phenomes
Temperature, °C	In indoors of industries (20 °C to 30 °C)	Environmental Phenomes

* https://www.epa.gov/criteria-air-pollutants/naaqs-table, ** https://store.astm.org/d0512-04.html

Table 1 shows the relevant information about the AQS, to detect and control with specialized sensors and filters the air pollutants mentioned, to avoid the presence of aggressive environments and with this, the occurrence of the metallic corrosion.

Microscopy analysis

In this part of the investigation was made a microanalysis of the presence of the two types of corrosion with more frequency appeared, where was observed in the first section of the figure (as figure 1a), the majorly of the electrical connection evaluated, as was deteriorated almost totally in the metallic surface. In change in the second section of the figure (as figure 1b), was illustrated a hole and the metallic surface cracked[1].

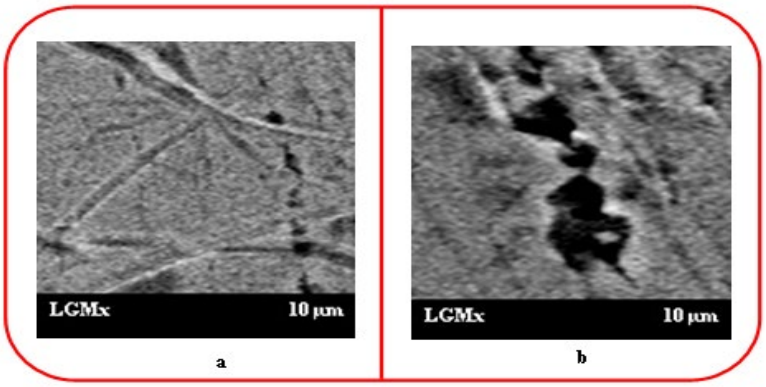

Figure 1 Microanalysis of electrical connections presenting uniform (a) and pitting corrosion (b) (2023).

METHODOLOGY

In this investigation was realized the principal activities that are showed next, to determine the principal causes of the two types of corrosion occurred in this electronics industry:

a) An analysis of the atmospheric agents that was involved in this investigation was made, as the air pollutants and climatic parameters mentioned above.

b) A micro evaluation of deterioration of electrical connections of electronic systems of industrial equipments and machinery, which were generated electrical failure that was caused in sometimes stop line products and defective fabricated products in this electronics industry where was made this scientific study.

RESULTS

This investigation is very important, because in all places of the world where are installed industrial plants as the electronics industry as was analyzed in this industrial city (Tijuana), can occurs the microdeterioration of metallic surfaces of electrical connections. This

originates complicated situations, which are factors causing the decrease in productivity and quality indices.

Evaluation of the atmospheric agents

In this section was elaborated an evaluation of the presence of the air pollutants mentioned above and variations of climatic factors as atmospheric parameters, which were originated the corrosion process. Also, was made a correlation analysis of these relevant aspects evaluated, and the productivity and quality indices that are illustrated in table 2.

Tabla 2 Correlation analysis of atmospheric factors and productivity and quality levels

Production Factors	Productivity, %				Quality, %			
Atmospheric Agents	Cl^-	CO	NO_X	SO_2	Cl^-	CO	NO_X	SO_2
Air Pollutants	65,87	70,89	61, 87	60, 84	69, 89	71, 93	62, 88	64, 86
	T, °C		RH, %		T, °C		RH, %	
Climatic Factors	72, 93		70, 91		69, 92		70, 90	

As is showed in table 2, the productivity and quality indices were increased from the third month of the elaboration of this scientific study, observing that in the NO_X y SO_2, these production factors were less than other numerical data, indicating that were the air pollution agents, which caused the major deterioration and damage to the electrical connections, where were not controlled it.

Analysis of the microdeterioration of electrical connections

To determine the grade of microdeterioration was made a microanalysis in some electrical connections of the electronic systems evaluated, being represented in figure 2, with two sections, which were illustrated the uniform corrosion (figure 2a) and pitting corrosion (figure 2b).

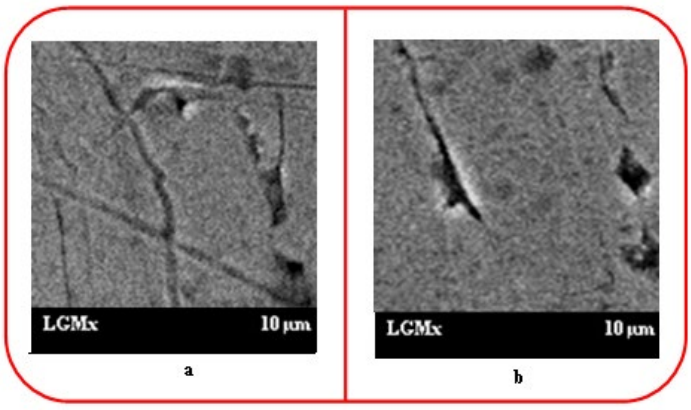

Figure 2 Microdeterioration caused by atmospheric factors originating uniform corrosion (a) and pitting corrosion (b) (2023).

CONCLUSIONS

This scientific study reflected relevant numerical data as information of great interest to directive people, managers, supervisors and specialized persons, which acts very fast in addition with the researchers of this paper, to avoid the microdeterioration of electrical connections and with this an efficient operation of industrial machinery and equipments,

which support to obtain high productivity and quality indices and economical gains in this electronics industry evaluated.

REFERENCES

[1] Gustavo López Badilla, Hugo Tiznado Vázquez, Gerardo Soto Herrera, Benjamín Valdez Salas, Miguel Schorr Wiener, Roumen Zlatev (2010). "Corrosion of electronic devices by atmospheric corrosion in indoor of industrial plants of arid and marine enviroments, Biological Sciences, Vol. 3, No. 5, https://novascientia.lasallebajio.edu.mx/ojs/index.php/novascientia/article/view/197

[2] Gustavo López Badilla, María Marcela Acosta Gómez, Elizabeth Romero Samaniego, Sandra Luz Toledo Perea, Rodolfo T. G. Garduño, Carlos O. G. Márquez, Juan P. Q. Hinojosa (2013). "Corrosion in Control Systems Decrease the Lifetime of the Electronic Devices of the Industrial Plants of Mexicali, BC, Mexico, *Open Journal of Air Pollution* Vol.2 No.2, June 20, 2013, DOI: 10.4236/ojap.2013.22005.

[3] Gustavo López Badilla, Juan Manuel Terrazas Gaynor (2021). "Corrosion of Electronics system in Mexicali, Materials Performance Journal, 59-59, February, 2021.

[4] Wei Z., Jiuguo D., Yilong Z., Hao l., Ziyao L., Rongshuo W., Yuding L., Guofeng Q., Mingyang Z., Jijun Y. (2024). "Microstructure response and LBE corrosion behavior of the FeCrAlY coating after Au-ions irradiation", Corrosion Science, Volume 241, December 2024, 11252.

[5] Hakim A., Ahmed Al-A., Wan N.R. (2024). "Advancements in Corrosion Prevention Techniques", Vol. 10, No. 78, https://link.springer.com/article/10.1007/s40735-024-00882-w

POLYMAT CONTRIBUTIONS, Año 8, No. 8, enero-diciembre 2025, es una publicación anual editada por la Universidad Nacional Autónoma de México, Ciudad Universitaria, Delegación Coyoacán, C.P.04510, México, D.F., a través del Instituto de Investigaciones en Materiales, Avenida Universidad 3000, Col. Copilco, Del. Coyoacán, C.P. 04510, Ciudad de México, Tel. (55)56224500 y (55)56224581, www.iim.unam.mx/polymatcontributions, polymat@unam.mx. Editor Responsable: Dr. Armando Reyes Montero, Reserva de Derechos al uso Exclusivo No. 04-2015-110313532900-203, otorgado por el Instituto Nacional del Derecho de Autor, ISSN 2448-590X.

Responsable de la última actualización de este número, Instituto de Investigaciones en Materiales, Dr. Armando Reyes Montero, Avenida Universidad 3000, Col. Copilco, Del. Coyoacán, C.P. 04510, Ciudad de México, fecha de la última modificación, diciembre de 2025. Las opiniones expresadas por los autores no necesariamente reflejan la postura del editor de la publicación. Se autoriza la producción total o parcial de los textos aquí publicados siempre y cuando se notifique al editor.

ISSN 2448-590X